

**TOWARDS AUTOMATION OF MULTIMODAL CELLULAR
ELECTROPHYSIOLOGY**

A Dissertation
Presented to
The Academic Faculty

By

Mighten C. Yip

In Partial Fulfillment
of the Requirements for the Degree
Doctor of Philosophy in
Bioengineering

Georgia Institute of Technology

May 2023

© Mighten C. Yip 2023

**TOWARDS AUTOMATION OF MULTIMODAL CELLULAR
ELECTROPHYSIOLOGY**

Thesis committee:

Dr. Craig R. Forest
GWW School of Mechanical Engineering
Georgia Institute of Technology

Dr. J. Brandon Dixon
GWW School of Mechanical Engineering
Georgia Institute of Technology

Dr. Stephen F. Traynelis
School of Pharmacology
Emory University

Dr. Christopher R. Valenta
School of Electrical and Computer Engineering
Georgia Tech Research Institute

Dr. Matthew J.M. Rowan
School of Cell Biology
Emory University

Dr. Ming-Fai Fong
Wallace H. Coulter Department of
Biomedical Engineering
Georgia Institute of Technology

Date approved: April 21, 2023

The credit belongs to the man who is actually in the arena, whose face is marred by dust and sweat and blood; who strives valiantly; who errs, who comes short again and again, because there is no effort without error and shortcoming; but who does actually strive to do the deeds; who knows great enthusiasms, the great devotions; who spends himself in a worthy cause; who at the best knows in the end the triumph of high achievement, and who at the worst, if he fails, at least fails while daring greatly, so that his place shall never be with those cold and timid souls who neither know victory nor defeat.

Theodore Roosevelt

For my parents who support me as I pursue my dreams

ACKNOWLEDGMENTS

When I first started my PhD, I looked forward to the day I would be able to write the acknowledgments of my thesis. For me, I always enjoyed reading this section of other doctoral theses because they gave a glimpse into their personality and community that brought them to the finish line of the PhD. First of all, this PhD would never have happened without Dr. Craig Forest, my PI, who gave me the opportunity to be an engineer in the field of neuroscience and provided me with wonderful mentorship, guidance, and wisdom as I navigated the PhD over the past six years. I would also like to add that his support for my passions outside of the PhD were critical in my growth as a person and towards my future career.

I would also like to take a step back and begin my thank you roll call from the beginning of my academic career – for which none of this would have occurred without the myriad of butterfly effects that concatenated until I got this point. As no one can play music to boot me off the stage, I appreciate you sticking through the entire story. I would like to thank the professors at the University of Southern California (Fight on!) for cultivating my intellectual curiosity, but more specifically, to Dr. Veronica Eliasson whose fluid dynamics class and her suggestion to pursue a PhD ignited the next decade of my life. As always, it was not until the eleventh hour that I truly decided to apply, and with limited time, the scope of where I applied was small. However, after endless reach-outs, I was able to connect with Dr. Firat Güder (and had just started at Imperial College London) who worked tirelessly with me to apply for any and all PhD student-specific grants under the sun to get me across the pond. While it was to no avail, I am extremely grateful for the opportunity I had to learn from him. While the start of my PhD was delayed, this did allow me the opportunity to join the George Whitesides Research Group at Harvard where I was taken under the wing of Dr. Alar Ainla. Alar is an incredibly kind, gifted engineer, and my applied learning skyrocketed during my time there. Furthermore, other postdocs like Dr.

Maral Mousavi gave me opportunities to participate in their projects, and you could say that I was permanently hooked on getting my PhD. Then, in a random moment of chance, another postdoc, Dr. Brian Cafferty, suggested I apply to Georgia Tech because he found it a wonderful time when he got his PhD there and so I did. After the project I worked on had concluded, I had the chance to go to New York City and work with Dr. Bobak Mosadegh and Dr. Simon Dunham at Weill Cornell Medicine. While I had fun doing research in Cambridge, it felt especially galvanizing to be mentored by Simon and Bobak particularly because of the freedom to explore different topics. Funnily enough, after nearly reaching the conclusion of my own PhD, a paper we had started working on right before I left was recently published. We are finally metal-benders. And after this length preamble, brings me to the start of my PhD here at Georgia Tech.

First and foremost, I would like to thank my lab, Precision Biosystems Laboratory, for providing such an inviting and wonderful space to spend the past six years. To those that came before me: Dr. Ilya Kolb, whose giant shoulders I stand on as a result of his work. While we overlapped briefly in Atlanta, our collaborations together over the years have led to a steadfast friendship, and I am grateful for our time working together; Dr. Will Stoy and his critical reasoning; Dr. Timothy Lee and his level-headed teachings; Dr. Corey Landry with whom I spent countless hours philosophizing about the aimless aims of our research and whose autopatching efforts are unmatched; Dr. Colby Lewallen who was the flashlight to my abstract ideas, empathized and commiserated with me, and found ways for us to rabbit hole into passion projects for months at a time. And thank you to those that came after me: Phoebe Welch and her insane time management to help me with experiments and countless others; Mercedes Gonzalez, without whom I would have been doomed to never complete this PhD; and Athena Chien, Mohamed Badawy, Ally Dunnum, Nathan Malta, Caitlin van Zyl for their help in the lab.

Of course, my PhD would not have been as productive or eventful without all my wonderful mentors along the way. To name a few, huge thanks to Dr. Bo Yang for providing his

slicing wizardry and expertise in neuroscience. Truly a big thank you to Dr. Riley Perszyk for teaching me the ropes of patching and pharmacology, congruently seeing the vision of the pharmaBot, and working tirelessly with me on my many side project ideas. As well as a thank you to Dr. Chris Obara who I met while at Janelia and shaped how I critically thought about science holistically.

Also, a very grateful thank you to my thesis committee, Dr. Brandon Dixon and Dr. Ming-fai Fong from Georgia Institute of Technology; Dr. Chris Valenta from GTRI; Dr. Matt Rowan and Dr. Stephen Traynelis from Emory University for providing me impactful insight and fruitful collaborations over the years. In addition, special thanks to the other collaborators I had the pleasure of working with during my PhD: Dr. Andy Jenkins, Dr. Ed Boyden, Dr. Karel Svoboda, and Dr. Wyatt Korff.

And of course, none of this would be possible without the support of my friends and family. To my friends, from the early DMT days to SJM to Dreamz and to the ATL community who have buoyed me throughout this experience, thank you! To my siblings Melody and Megan, thank you for being my biggest fans and happy to learn and tell other people about automation towards cellular electrophysiology. And most importantly, the biggest thank you to my parents for their unwavering support as I stepped into the PhD arena.

There were many people along the way who were helpful with my journey, and I hope I did not miss too many of you. But again, thank you to everyone who supported and witnessed this journey of mine. Together we swarm, fight on!

TABLE OF CONTENTS

Acknowledgments	v
List of Tables	xii
List of Figures	xiii
List of Acronyms	xvii
Summary	xix
Chapter 1: Introduction and Background	1
1.1 Introduction	1
1.1.1 Limitations of patch clamp recording	3
1.1.2 Automation of patch clamp recording	5
1.1.3 Pharmacology in patch clamping	6
1.1.4 Optogenetic engineering in patch clamping	8
1.1.5 Machine learning in patch clamping	9
1.1.6 Local synaptic connectivity and circuit mapping	10
Chapter 2: Integrate automated patch clamping to improve reproducibility and throughput for traditional pharmacology assays	13
2.1 Summary	13

2.2	Introduction	14
2.3	PatcherBot _{Pharma} Hardware and Software	15
2.3.1	Transiently Expressing HEK cells	16
2.3.2	Stably Expressing HEK cells	17
2.3.3	Whole-cell voltage-clamp recordings	18
2.3.4	Analysis and Statistics	18
2.4	Discussion	25
2.5	Additional Pharmacology Experimentation	28
	Chapter 3: Integrate automated patch clamping for genetically encoded voltage indicators and effectors	39
3.1	Motivation	39
3.2	Introduction	40
3.3	Methods and Validation of voltage imaging integration with the patcherBot	42
3.3.1	Current GEVIs	42
3.4	Methods	45
3.4.1	Validation of voltage imaging	45
3.4.2	Neuronal cell culture	45
3.4.3	Automated whole-cell electrophysiology	46
3.5	Results	47
3.5.1	High throughput optimization of the patcherBot for GEVI screening	47
3.5.2	High throughput screening of Voltron mutants in neuron culture . .	49
3.5.3	Screening and characterization with automated whole-cell electro-physiology	51

3.6	Opsin Screening and PatcherBot Integration	55
3.6.1	Opsin autopatching significance	55
3.6.2	Implementation towards directed evolution platform capable of high-throughput screening of optogenetic tools	55
Chapter 4: Deep learning-based real-time detection of neurons in brain slices for <i>in vitro</i> physiology		
4.1	Introduction	63
4.2	Methods	65
4.2.1	Implementation	66
4.2.2	Evaluation metrics of YOLOv3 performance	68
4.2.3	Real-time detection and patch clamp validation	69
4.3	Results	71
4.3.1	Digital Image Processing for Acute Brain Slices	71
4.3.2	YOLOv3 Neuron Detection	72
4.3.3	Inference Results	73
4.3.4	Patch Clamp Experiments	74
4.4	Discussion and Conclusion	75
Chapter 5: Coordinated multi-pipette patch clamp for enabling high throughput synaptic connectivity studies		
5.1	Introduction	82
5.1.1	Motivation	84
5.2	Methods	85
5.2.1	Computational multipatching modeling	85

5.2.2	Multipatching patcherBot	88
5.2.3	Brain slice preparation	92
5.2.4	Patch-clamp recording	93
5.2.5	Dual-patch experimental validation	93
5.2.6	Statistics	94
5.3	Results	95
5.4	Discussion	103
Chapter 6: Conclusion		105
6.1	Major Contributions	107
6.2	Future Work	108
Appendices		110
Chapter A: pharmaBot Manual		111
A.1	patcherBot _{pharma} - Manual and SOP	111
A.1.1	Important Considerations	111
A.1.2	Before each experiment:	137
Chapter B: Preliminary "Super" Pipettes		150
B.1	Quartz and Focused Ion Beam-milled pipettes	150
References		155

LIST OF TABLES

2.1	patcherBot _{Pharma} overall success rate	28
2.2	Manual and Autopatching Comparison	35
2.3	Activation and deactivation parameters	36
2.4	Census of robotic operation and operator interaction time for the propofol case study	36
2.5	Concentration response of propofol	37
2.6	Performance of the patcherBotPharma in the propofol case study	38
3.1	ASAP1 screen throughput	49
4.1	Mean average precision of unaltered and enhanced trained networks tested on unaltered and enhanced input images.	74
4.2	F1 score of unaltered and enhanced trained networks tested on unaltered and enhanced input images.	74
B.1	Resistance as a function of pipette construction	150

LIST OF FIGURES

1.1	Whole-cell patch clamp sequence	2
1.2	patcherBot setup	7
1.3	patcherBot workflow	8
2.1	patcherBot workflow showcasing a discovery experiment for pharmacology. The difference here versus the original patcherBot is the addition of drug application during ephys recordings.	16
2.2	patcherBot _{Pharma} description	17
2.3	Repeatable, precise physical manipulations for solution exchange	29
2.4	Fast-solution exchange	30
2.5	Representative experimental timeline of patcherBot _{Pharma} operation	31
2.6	patcherBot _{Pharma} experimental workflow	32
2.7	Solution exchange protocols	33
2.8	Voltage- and current-clamp protocols programmed into the patcherBot _{Pharma}	34
3.1	patcherBot workflow showcasing the use of voltage imaging screening within the electrophysiology experiment. The difference here versus the original patcherBot is the addition of voltage imaging during ephys recordings.	42
3.2	Estimated throughput model for the voltage imaging-specific patcherBot based on the maximum number of cleans per pipette. The red box shows with an average maximum number of cleans at 20, we can expect around 3.5 constructs screened per day.	42

3.3	The physical setup of the patcherBot @ Janelia in collaboration with Sen- sapex.	43
3.4	ASAP1 voltage indicator explanation	44
3.5	ASAP1 $\Delta F/F_0$ manual vs automated comparison	48
3.6	$\Delta F/F_0$ examples for different ASAP variants	49
3.7	Voltage clamp and imaging example for ASAP1 neuronal culture	50
3.8	patcherBot mid-experiment voltage clamp and imaging of ASAP1-transfected neuron	51
3.9	Zoomed image of active pixels in field of view for voltage imaging	51
3.10	Manual versus patcherBot representative voltage clamp experiment on cul- tured neurons	57
3.11	Representative patcherBot voltage clamp experiment for transfected HEK cells	58
3.12	Mutagenesis and screening workflow of Voltron	58
3.13	Automated patch clamp screening and characterization of Voltron2 in cul- tured neurons	60
3.14	patcherBot workflow showcasing the use of opsin screening within the elec- trophysiology experiment. The difference between the original patcherBot is the addition of light stimulation during the ephys recording.	60
3.15	ChR2 cartoon explanation and example of transfected HEK cells on the patcherBot rig	61
3.16	50 whole-cell opsin screening experiment with representative traces	62
4.1	Deep-learning based method and training	65
4.2	Classic digital image processing methods for neuron detection	78
4.3	YOLOv3 deep-learning training and validation statistics and results	79
4.4	YOLOv3 testing statistics and results	80

4.5	Patch clamp results utilizing the YOLOv3 real-time detection	81
5.1	Multipatching literature review	86
5.2	Computational modeling of multipatching with differing route-planning algorithms	87
5.3	Software debugging and validation methodology	89
5.4	Example route-planning path for 4 manipulators	89
5.5	Hardware and software experimental setup for patch-walking	91
5.6	Supplemental methods and results of the dual-patcherBot	94
5.7	Dual-patching throughput and quality metrics	96
5.8	Connectivity matrix and recordings using patch-walking	99
A.1	Cartoon Representation of the patcherBot _{Pharma}	112
A.2	Camera: QImaging Retiga Electro	112
A.3	Z-focus Module	113
A.4	Elevated Microscope Platform. This is a custom milled sheet of aluminum. .	113
A.5	Bath Chamber. Note: .STL files for the depicted chamber is posted on Github.	114
A.6	Electrode Manipulator.	114
A.7	Solution manifold.	114
A.8	Piezoelectric translator.	115
A.9	Peristaltic pump.	115
A.10	Solution valves.	115
A.11	DAQ.	116
A.12	Custom pressure control box	116

A.13 Main VI Left Panel.	116
B.1 Unaltered quartz pipette	151
B.2 Focused ion beam-milled quartz pipette	152
B.3 Size change of pipette after FIB-mill	153
B.4 Resistance of pipette based on outer diameter milling	154

LIST OF ACRONYMS

- aCSF** Artificial Cerebro-Spinal Fluid
- ASAP** Accelerated Sensor of Action Potentials
- ChR2** Channel-rhodopsin 2
- CI** Confidence Interval
- DAQ** Data Acquisition System
- DIC** Differential Interference Contrast
- FOV** Field of View
- GABA** Gamma-Aminobutyric acid
- GABA_AR** Gamma-Aminobutyric acid Receptor Type A
- GEVIs** Genetically Encoded Voltage Indicators
- GUI** Graphical User Interface
- HEK-293** Human Embryonic Kidney cells
- IG** Image-Guided
- MCTS** Monte Carlo Tree Search
- NH** Neuron hunting
- NMDA** N-methyl-D-aspartate
- NMDA_AR** N-methyl-D-aspartate Receptor
- O-O** Outside-out
- PV-int** Parvalbumin Inhibitory Interneurons
- R** Resistance
- R_A** Access Resistance
- R_{GS}** Gigaseal Resistance

VI Visual area I

WC Whole-cell

SUMMARY

Understanding how neurons of the brain communicate, connect, and respond to stimuli is a fundamental goal of neuroscience. Whole-cell patch clamp recording in vitro represents the gold standard method for measuring electrophysiology of single neurons because of its high spatiotemporal resolution. However, the manual and time-consuming nature of patch clamping experiments have limited the throughput and number of cells that can be sampled per day. To improve the throughput for these single-cell experiments, the goal of this dissertation was to (1) integrate automated patch clamp with discovery experiments for cellular indicators and effectors, (2) develop a machine learning algorithm for real-time neuron detection of neurons in brain slices for in vitro patch clamping, and (3) create a coordinated, multi-pipette patch clamp algorithm for enabling high throughput synaptic connectivity studies. Towards these aims, this thesis demonstrated the first robotic system to perform ligand-gated ionotropic receptor protocols autonomously leading up to a 10-fold reduction in research effort over the duration of the experiment. I showed the robot can rapidly replicate an 8-point concentration response curve of the effect of propofol on GABA_AR deactivation from likely weeks to 13 hours of recording. In addition, I integrated the fully automated patch clamp robot to discover a brighter and more sensitive chemigenetic voltage indicator, Voltron2, over its predecessor exhibiting 3-fold higher sensitivity in response to sub-threshold membrane potential changes. Towards the second aim, I developed a novel, deep learning-based method able to accomplish automated, real-time neuron detection in brain slice at 18 frames per second with high precision and trained with a small data set of 1138 annotated neurons. The final aim of this thesis describes the first ever fully automated, multipatching robot able to "walk" across a brain slice in a coordinated route plan to efficiently probe for local synaptic connections between neurons. The combination of these technologies has created a bouquet of tools to enable high-efficiency, single-cell experiments that yield multiple types ("multimodal") of cellular electrophysiology data.

CHAPTER 1

INTRODUCTION AND BACKGROUND

1.1 Introduction

Patch clamp recording is a gold-standard technique for the accurate measurement of single-cell membrane voltage fluctuations, synaptic currents, and ionic channel activity in neurons [1, 2]. Using a glass micropipette to form a physical seal with a small patch of membrane on a target cell, one can directly record with high temporal (>10 kHz) and voltage resolution (<1 mV) the electrical activity of the cell, fully avoiding interfering signals from other neurons. The sensitivity of patch clamp recording has uniquely permitted the recording of current signals in an individual ion channel [3] and synapse [4]. Whole-cell patch clamping, a variant of the technique in which the patch of membrane is ruptured to obtain access to the cell cytosol, has been used to characterize synaptic plasticity [5], study sub-cellular compartments [6], and elucidate connectivity among nearby neurons [7].

Typically, whole-cell patch clamp studies are performed under microscope guidance, allowing a direct visualization of cells [8]; however, “blind” patch clamp recording, in which pipette Resistance (R) is used as a proxy to detect cell contact is also possible [9]. The majority of patch clamp studies are currently performed on cultured cells adhered to a substrate or in slices of living brain tissue even though patch clamp recording in-vivo has yielded unique insight into the function of single cells in physiologically relevant states [10].

An example sequence of steps in a whole-cell electrophysiology experiment in brain slices is as follows (Figure 1.1 shows the main steps):

1. Visually identify a brain region of interest under low magnification (4x).
2. Visually identify a target cell suitable for patch clamp recording using differential

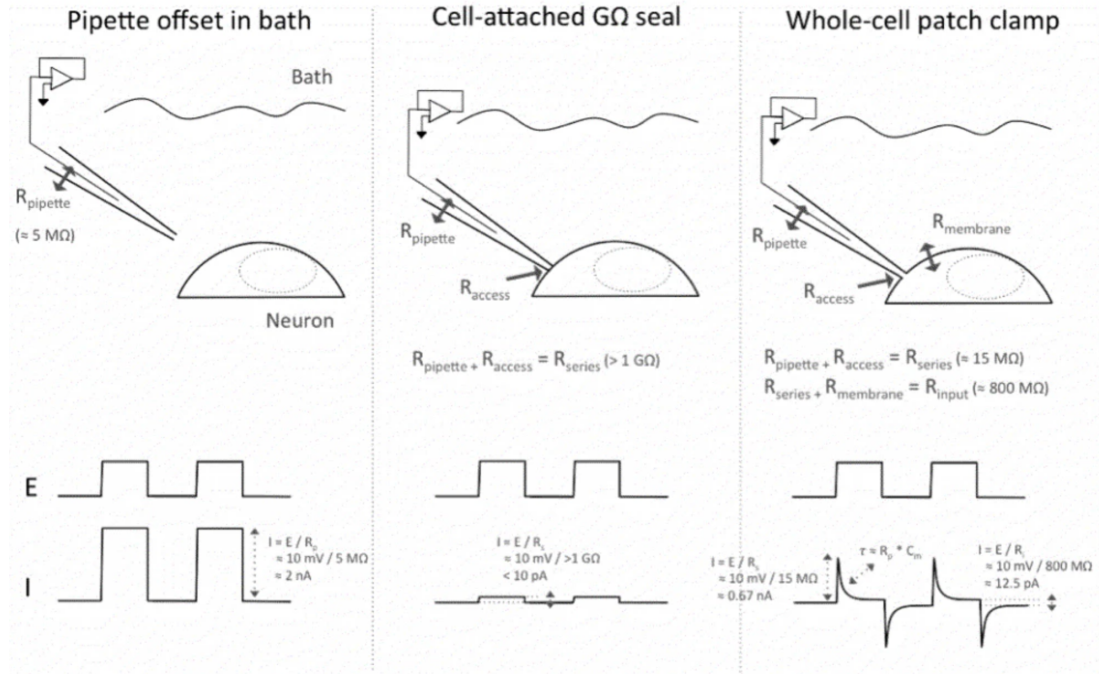


Figure 1.1: Whole-cell patch clamp sequence. Copyright Axol Biosciences Ltd.

interference optics (DIC) under high magnification (e.g. 40x) in the brain region of interest. A cell is generally picked by distinguishing morphological characteristics or the perceived health of its cell membrane, but may also be picked based on the presence of a fluorescent marker.

3. Several (10-100) microns above the slice, find the patch clamp pipette under the high-magnification objective and apply positive pressure to the pipette by mouth or with a syringe. This positive pressure is not acute and is constant until Step 6.
4. Descend pressurized pipette to a relative distance ($\sim 10 \mu\text{m}$) above target cell.
5. Approach target cell slowly while monitoring the position of the cell and the pipette tip, the internal pressure in the pipette, and the electrical resistance.
6. Form a gigaohm seal ($> 1 \text{ G}\Omega$ Gigaohm Resistance (R_{GS})) with the cell by releasing positive pressure and applying slight suction. Apply a holding voltage of -70 mV before break-in.

7. Break into the cell by applying brief suction pulses to the pipette and monitoring the response to the membrane test.
8. Detect successful break-in by observing low holding current at -70 mV and capacitor transients in response to square wave voltage pulses. This is done in voltage clamp where we clamp the membrane voltage to -70 mV and look at the required current to hold it there. This is just an example method and for different amplifiers, it may be advantageous to enter into current clamp.

1.1.1 Limitations of patch clamp recording

The immense diversity of neuronal cell types in the brain and their sparse connections create a tremendous demand for large sets of single-cell data that current patch clamp technologies cannot fulfill. Cell type classification of neurons remains a “holy grail” of neuroscience. Defining highly specific classes of neurons is difficult because of their inherent electrophysiological, morphological, and genetic variability, even within a single class. Thus, it becomes necessary to use large datasets that enable the creation of sufficiently defined borders between cell types.

The difficulty of collecting these data has resulted in many small-scale studies of cell characterization, e.g. $n=21$ [11], $n=89$ [12], $n=27$ [13] but precious few with >100 cells [14]. The low throughput from patch clamping has made it difficult to form a unified taxonomy of cell types. A notable attempt to do so is the recent effort by the Allen Institute for Brain Science (AIBS) aimed at creating a catalog of cells in the mouse primary Visual area I (VI) cortex. This ambitious, multi-year project is set to profile thousands of neurons using patch clamping; however, with the current throughput limitations of the technique, it is not clear if these efforts can be replicated in other brain regions or by any other lab or institution in the future.

The sparse connections between neurons are fundamentally important to brain function but are difficult to study in large numbers. Inter-neuronal connections form the foundation

of learning and memory and faulty connectivity patterns can give rise to neurological disorders [15]. Despite the importance of these connections, there is a dearth of large-scale single-cell connectivity studies, owing to the compounded difficulty of patch clamping multiple neurons simultaneously as well as the inherently low inter-neuronal connection probabilities. For instance, studies of brain regions with low (2%) connection probabilities will yield only 39 connections in 2,000 dual-patch recordings [16]. Recent advances in micromanipulator stability and electronic multiplexing have enabled eight and twelve simultaneous patches [17] which dramatically increases the number of connections that can be sampled simultaneously. This increase in throughput has led to impressive studies with the number of total patches numbering in the thousands, e.g. >8,000 [18], >2,500 [19], >1,000 [20], >11,000 [21]. However, those studies still require hundreds of experiments and the high-channel patch clamp technique still requires tremendous skill, dexterity and experience to set up and use, and is thus far from a “benchtop” tool for analyzing neuronal connectivity.

In stark contrast to the thousands of data points necessary to sufficiently identify a cell type or profile a synaptic connection, only a handful of cells are typically patched in a single day by an experimenter. The low throughput from patch clamping is primarily a result of two factors: first, neurons in brain slices die over the course of the experiment; 12+ hours after slicing the brain, it is thought that most neurons visible under DIC are unsuitable for patch clamping [22]. Second, the highly manual nature of patch clamp experiment which requires extensive attention, skill, and dexterity is physically and psychologically taxing on the investigator. Given the highly repetitive yet demanding nature of the task, when large datasets are necessary, many advantages of patch clamp recording are offset by its low throughput.

1.1.2 Automation of patch clamp recording

Several automation technologies have emerged to alleviate some of the manual tasks in patch-clamping. Fully-automated systems have been developed for patching onto dissociated cells [23]. These planar patch clamp devices automatically capture dissociated cells suspended in solution into an etched cavity which replaces the conventional patch clamp pipette. While these systems are widely used in pharmacology due to their high throughput [24, 25], they are not suitable for substrate-adhered (non-dissociated) cells or cells in sliced brain tissue, making them impractical for studying neurons in culture or brain slice.

For conventional (pipette-based) experiments, several hardware and software technologies have been crucial to reducing the complexity and increasing the throughput of each trial. On the hardware side, commercially available motorized actuators and XY translation stages have enabled precise, motorized manipulation of a pipette to a target cell. Once a cell is approached, automated pipette pressure control via an “Autopatcher” device developed in our lab enables one to automatically form a gigaseal with the target neuron and break-in to reach the Whole-cell (WC) configuration [26].

Various software packages take advantage of the motorized and automated hardware to automate portions of the patch clamp trial. The LinLab and PatchVision software packages (Scientifica Ltd.) allow users to move pipette actuators to pre-defined positions, keep pipettes in view while moving the sample, and customize the function of stage and manipulator control devices. Free, open-source software packages such as Micro-Manager [27], Ephus [28], and Acq4 [29] effectively combine multiple acquisition and manipulation devices to create a unified user interface for patch clamp recording and photostimulation. While these software packages automate electrophysiology experiments after a whole-cell configuration has been reached, they do not automate the patch clamp procedure itself. Recently, a custom multi-electrode patch clamp system automated multi-pipette positioning and seal formation with up to 12 pipettes [30].

The hardware and software developments mentioned above have sped up experiments

and enabled more convenient user interaction with scientific equipment but do not completely automate a full in-vitro microscope-guided patch clamp experiment. That is, for all the mentioned solutions, a skilled and experienced user is still required to (1) manually navigate the pipette to the target cell and (2) replace pipettes after each patch clamp attempt. Thus, existing technologies do not automate microscope-guided patch clamp recording to the level of an autonomous, independently functioning system. While there are concerns that an automated system will not match the flexibility and experience of a trained user [17], few would argue that high-throughput patch clamp data collection will be possible without major automation efforts.

To improve the throughput and reduce the barrier to entry for these high value experiments, the Forest lab recently developed the “patcherBot,” a robot (Figure 1.2) that automatically performs whole-cell recordings in adherent cells and acute, mouse brain slice by algorithmically detecting and recording from individual cells using Image-Guided (IG) techniques with pipette reuse allowing for fully, unattended patch clamping experiments (workflow in Figure 1.3). The patcherBot can obtain data at a rate of 16 cells (adherent) per hour and work with no human intervention for up to 3 hours [31]. Using such an automated system, we were able to identify a myriad of patch clamping developments that were enabled due to the controlled, automated ability of the patcherBot. For instance, we discovered that pipette cleaning can be improved by a factor of three [32], and that gigaseal success probability is a product of distance from the pipette to the cell. With the validation of the patcherBot, it has enabled the potentially transformative application towards high-quality measurements of single cells for discovery experiments such as drug screening, protein functional characterization, and other multimodal cell type investigations.

1.1.3 Pharmacology in patch clamping

Many alternative methods and machines have been developed that attempt to accelerate the collection of data that approximates what patch-clamp electrophysiology can achieve, such

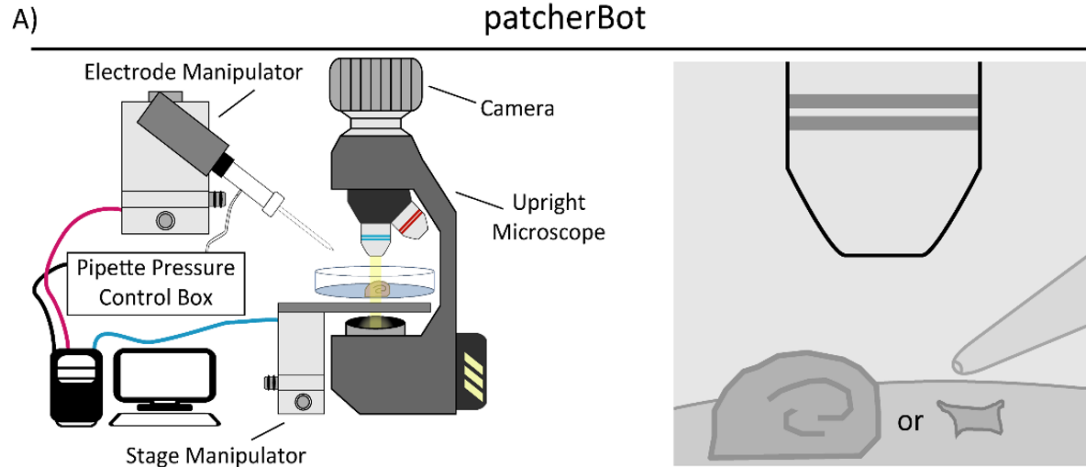


Figure 1.2: Cartoon of the previously published PatcherBot (Kolb et al. 2019), assembled from an upright microscope, high sensitivity camera, custom pressure control box, quasi-4 axis electrode manipulator, and a motorized stage..

as activity-sensitive fluorometric probes and high-throughput machines that patch dissociated cells on planar patch-clamp “chips” [33, 34, 35, 36]. However, these methods sacrifice the high precision of patch-clamp electrophysiology in order to achieve higher throughput. For instance, fluorometric probes must be tuned to a specific application, and fully resolving the kinetics or full activity of ionotropic receptors is typically not possible. Imaging experiments also cannot control for confounding voltage fluctuation associated with the measured response. Additionally, for high-throughput patch-clamp systems, performance is limited by their solution handling capabilities, and cost of both equipment and supplies are prohibitive for many studies. Most of these methods are also incapable of measuring cells that are adherent or embedded in tissue [28, 29, 34, 37, 38].

Thus, an implementation of the patcherBot that enables automated intracellular pharmacological electrophysiology would enable substantially faster acquisition of drug screening datasets. The “patcherBotPharma” can perform pharmacological concentration-response experiments and can record ligand-gated ionotropic receptor response to fast agonist exposure (millisecond exchange time) with automated control of the microscope, bath solution, a solution manifold, and a piezoelectric translator. We observe a high-throughput rate of the patcherBotPharma unattended, with further improvement using minimal operator as-

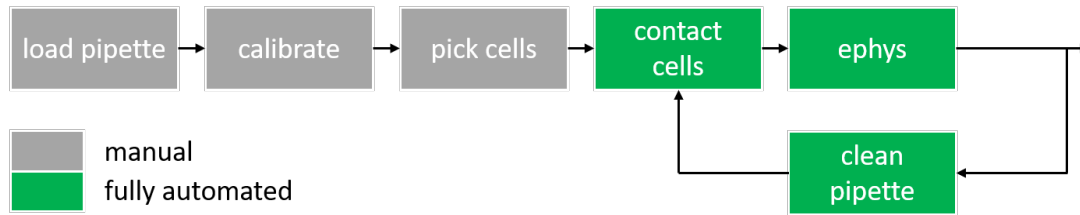


Figure 1.3: The first step is to load the pipette electrode onto the manipulator. The second step is to calibrate the tip of the pipette in the field of view on the microscope. The third step is to pick cells of interest to patch. The fourth step is to hunt (Neuron hunting (NH)) for the cell and come into contact with it with the electrode. After contact, a gigaseal is attempted and if successful, the pipette ‘breaks-in’ to the cell for a whole-cell configuration. Afterwards, electrophysiology recordings are conducted. After the data recording, the pipette is retracted and sent to be cleaned for reuse. The green boxes represent the fully automated portions of the patcherBot.

sistance. We show the capabilities of the patcherBotPharma by replicating a conventional dataset substantially faster — with considerably less human effort — than we had done previously. The increased efficiency enabled by this patch-clamp electrophysiology system creates the potential to address scientific questions that were previously considered impractical because of large, time-consuming requirements needed to complete data acquisition using conventional approaches.

1.1.4 Optogenetic engineering in patch clamping

Similar to how intracellular electrophysiology is important for pharmacology drug screening, whole-cell patch clamping is extremely important in screening for genetically encoded voltage indicators and effectors (GEVIs and opsins). Optogenetics is a form of protein mutation within an adherent cell or neuron that allows the use of light stimulation to change the membrane potential of itself. In the case of Genetically Encoded Voltage Indicators (GEVIs), the voltage potential of the neuron will be indicated by a change in fluorescence intensity. With effectors like opsins, the actual stimulation of light can cause a current response within the neuron [39, 40]. Furthermore, the method of optogenetics allow scientists to study the brain non-invasively and without any direct probes which is one of the drawbacks of patch clamping. With the development of optogenetics in the 2000s, aca-

demic labs around the world have focused on creating “better” protein mutations so that the opsin and GEVI response is faster, brighter, and less damaging to the neuron for longer recording opportunities [41, 42, 43, 44].

However, there are two fundamental issues with an all-optical study of the brain, (1) the temporal fidelity is not as precise as compared to whole-cell patch clamping, and (2) the difficulty in re-engineering and developing better GEVIs and opsins. Due to the vast number of mutant libraries for different protein mutations, there is still a requirement to use patch clamping as ground truth data to validate that the protein mutation and its mechanisms respond as they should to an action potential. In this manner, the use of whole-cell patch clamping is still required to further develop better opsins, and thus there is a need for automation and the use of the “patcherBot” to mitigate the time-consuming experiments of opsin validation. This thesis integrates light stimulation and voltage imaging with the patcherBot to optimize the automation for discovery experiments as it pertains to optogenetics.

1.1.5 Machine learning in patch clamping

One of the most crucial initial steps in the patch clamping process is identifying a healthy cell. The edges of a healthy neuron under Differential Interference Contrast (DIC) are often unclear and vary widely in shape and size. Moreover, the milieu of brain tissue not only consists of neurons, but also cerebrospinal fluid, blood vessels, and glia, among other extracellular content which induce significant light scattering under DIC, an optical technique widely used for observing unstained biological samples. While fluorescence microscopy may be used for identifying somas in acute slice patch clamp experiments, it is not always practical since it requires the use of dyes or genetically engineered production of fluorophores. Rather, it is often desirable to image label-free, yet optically transparent samples which requires the use of DIC.

Since identification of neurons is such a critical task, often requiring significant experi-

ence to identify healthy cells, automation of the cell identification and selection process is a difficult, necessary step towards completing full automation of patch clamp as well as in assisting novices how to identify cells. Research groups enabling the automation of patch clamp have alluded to the potential benefits of automating this task, though the problem is not yet fully resolved. Koos et al. have recently shown a CNN that identifies somas under DIC, though their network required substantial time and over 31,000 annotated neurons for training [45]. This thesis aims to achieve similar accuracy on a smaller, faster CNN that can quickly nominate cells for patch clamp experiments.

1.1.6 Local synaptic connectivity and circuit mapping

Lastly, as previously mentioned in the introduction, the notable attempt to map and catalog the mammalian neocortex by the Allen Institute for Brain Science was recently published [46]. This ambitious, multi-year project set out to profile thousands of neurons using patch clamping. Even more heroically, they managed to do this feat with brute force of manual patch clamping. Not only did this take years of effort by dozens of scientists, but it is not clear if these efforts can be replicated in other brain regions or by any other lab or institution in the future. But such an effort is required because cell types transmit information in a highly stochastic manner and dependently on past activity. The dynamic properties in connectivity between cell types suggest major implications in cortical function, and the need for empirical neuroscience data for computational and modeling studies is highly necessary. Thus, it is important to classify neurons to understand cortical circuit function as well as classifying probability and the dynamic synaptic relationship between pre- and postsynaptic cell types.

Other labs dedicated to the reconstruction of the local circuitry and synaptic connectivity within brain regions [17, 20, 47, 48] have also devoted years of heavy efforts, and the ability to add automation to the issue can greatly enhance the efficiency and effectiveness of such studies. Even more so, automation would add a level of efficiency for other labs

who also studied local circuitry on a more limited scale such as the anteroventral cochlear nucleus [49]. While an atlas and catalog of the local circuitry and synaptic connections in a brain region can enhance our ability to understand the brain, there is additional utility with automation of multiple manipulators for simultaneous multi-pipette patch clamping.

Indeed, neurons such as parvalbumin inhibitory interneurons (Parvalbumin Inhibitory Interneurons (PV-int)) are highly vulnerable to stressors and have been implicated in many psychiatric diseases like autism and Alzheimer's disease (AD) [50]. Alzheimer's disease is associated with changes in fast-spiking interneurons. Transgenic mice with AD-like pathology were found to have reduced gamma power that, in one model, precedes cognitive impairment and amyloid plaque formation [51]. In another study, a voltage-gated sodium channel (Nav1.1) that is largely found on axons of PV-int was decreased in a mouse model with amyloid pathology, and in AD patients [52]. Restoration of the levels of this voltage-gated sodium channel increased gamma oscillations, while memory deficits and premature deaths decreased [52]. Thus, the final aim was to create an efficient method to probe local synaptic connections between neurons. To do this, I developed the first ever forward-thinking multipatching robot demonstrating automatic, sequential recordings in a brain slice using a coordinated route plan. This method, named "patch-walking", uses a route-planning algorithm to optimize for efficient, high throughput synaptic connectivity studies whether it is used for profiling the local circuitry of a region of the mouse brain or for studying the effects of PV-int stressors that may lead to pathologies towards Alzheimer's disease.

To enable high throughput patch clamping for pharmacological, optogenetic, and chemi-genetic discoveries, I aim to link the electrophysiology of cells to the application of various effectors. Due to a vast number of mutant libraries for genetically encoded voltage indicators/ effectors and numerous pharmacological compounds, a rigorous, robust census of these libraries must necessarily be automated. I have developed and optimized an automated tool that enables recording of whole-cell intracellular recordings in combination with

drug delivery, light stimulation, or voltage imaging. With these technologies combined, this thesis enabled the first robot that can automatically search for connected neurons in brain tissue and also outperforms manual patch clamping-based screening assays to significantly advance the field of neuroscience and reveal new insights into brain function

CHAPTER 2

INTEGRATE AUTOMATED PATCH CLAMPING TO IMPROVE REPRODUCIBILITY AND THROUGHPUT FOR TRADITIONAL PHARMACOLOGY ASSAYS

2.1 Summary

We report an automated, high-precision patch clamp system which substantially improves the throughput of these time-consuming pharmacological experiments. The `patcherBotPharma` enables recording from cells expressing receptors of interest and manipulation of them to enable millisecond solution exchange to activate ligand-gated ionotropic receptors (work-flow seen in Figure 2.1). The solution-handling control allows for autonomous pharmacological concentration-response experimentation on adherent cells, lifted cells, or excised outside-out patches. The system can perform typical ligand-gated ionotropic receptor experimentation protocols autonomously, possessing a high success rate in completing experiments, and up to a 10-fold reduction in research effort over the duration of the experiment. Using it, we could rapidly replicate previous datasets, reducing the time it took to produce an 8-point concentration response curve of the effect of propofol on Gamma-Aminobutyric acid Receptor Type A ($GABA_A R$) deactivation from likely weeks of recording to 13 hours of recording (Figure 2.2). On average, the rate of data collection of the `patcherBotPharma` was a data point every 2.1 minutes that the operator spent interacting with the `patcherBotPharma`. The `patcherBotPharma` provides the ability to conduct complex and comprehensive experimentation that yields datasets not normally within reach of conventional systems that rely on constant human control. This technical advance can contribute to accelerating the examination of the complex function of ion channels and the pharmacological agents that act on them.

2.2 Introduction

Patch-clamp electrophysiology is an incredibly important technique that has enabled many discoveries in pharmacology, physiology, and neuroscience [1, 53]. Patch-clamp recording has the ability to accurately measure the time-course of postsynaptic or post-junctional currents and can fully resolve ion flux and the rapid transitions of individual ionotropic receptors [1, 54, 55, 56]. However, extensive effort and time are required to perform this high-resolution technique. Many alternative methods and machines have been developed that attempt to accelerate the collection of data that approximates what patch-clamp electrophysiology can achieve, such as activity-sensitive fluorometric probes and high-throughput machines that patch dissociated cells on planar patch-clamp “chips” [57, 33, 58, 34, 35, 36]. However, these methods sacrifice the high precision of patch-clamp electrophysiology in order to achieve higher throughput. For instance, fluorometric probes must be tuned to a specific application, and fully resolving the kinetics or full activity of ionotropic receptors is typically not possible. Imaging experiments also cannot control for confounding voltage fluctuation associated with the measured response. Additionally, for high-throughput patch-clamp systems, performance is limited by their solution handling capabilities, and cost of both equipment and supplies are prohibitive for many studies. Most of these methods are also incapable of measuring cells that are adherent or embedded in tissue [28, 29, 59, 34].

Recently, our group has worked on equipping a traditional intracellular electrophysiology rig with the capability to operate autonomously [60, 31]. Robotic vision, pipette pressure control, and electrode cleaning enable the resulting “patcherBot” to execute the basic steps required to perform patch-clamp electrophysiology without human intervention. Utilizing these automated methods allow for the acceleration of electrophysiology experimentation by reducing the process times of many steps as well as drastically decreasing the amount of required operator-rig interfacing time. The patcherBot is capable of patching

over 30 cells sequentially, can run unattended for over 4 hours, and operates at about a 70% success rate (reaching the whole-cell patch-clamp configuration per patching attempt) [31]. These advances enable the patcherBot to record spontaneous activity or voltage-dependent biological phenomena, and they can be multiplexed within a single preparation to record from multiple cells simultaneously. Thus, the patcherBot is highly proficient at addressing questions such as connectomics or intrinsic properties of neurons. Despite its many capabilities, this technology cannot perform many assays on ligand-gated ionotropic receptors or pharmacological studies.

Here, we present an implementation of the patcherBot that enables automated intracellular pharmacological electrophysiology. The “patcherBot_{Pharma}” can perform pharmacological concentration-response experiments and can record ligand-gated ionotropic receptor response to fast agonist exposure (ms exchange time) with automated control of the microscope, bath solution, a solution manifold, and a piezoelectric translator. We observe a high-throughput rate of the patcherBot_{Pharma} unattended, with further improvement using minimal operator assistance. We show the capabilities of the patcherBot_{Pharma} by replicating a conventional dataset substantially faster — with considerably less human effort — than we had done previously. The increased efficiency enabled by this patch-clamp electrophysiology system creates the potential to address scientific questions that were previously considered impractical because of large, time consuming requirements needed to complete data acquisition using conventional approaches.

2.3 PatcherBot_{Pharma} Hardware and Software

The patcherBot_{Pharma} is built on a standard inverted microscope (Axiovert 200, Zeiss) to allow for clearance of the recording electrode and solution handling manifolds. Standard, three-axis micromanipulators were used to translate the recording electrode (PatchStar, Scientifica) and the microscope (Motorized XY Stage [UMS] with Z-focus module, Scientifica). A high sensitivity camera (Retiga Electro, QImaging) is used for computer vision.

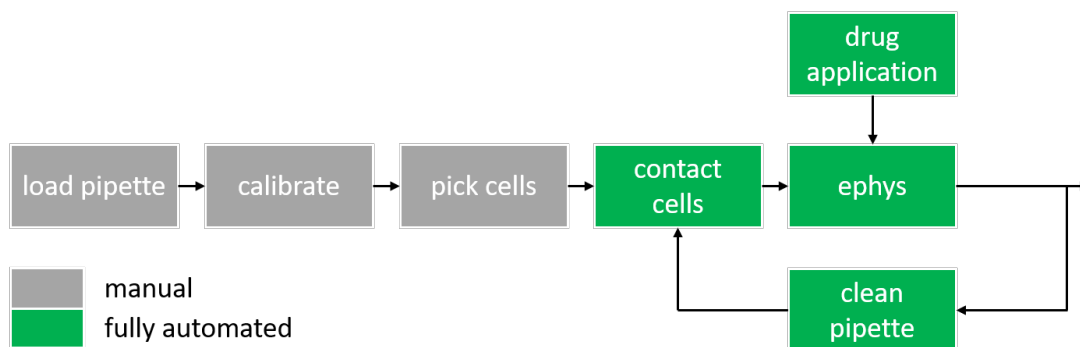


Figure 2.1: patcherBot workflow showcasing a discovery experiment for pharmacology. The difference here versus the original patcherBot is the addition of drug application during ephys recordings.

Electrode pressure was controlled using a custom control box that regulates house-air line to deliver -700 to +1000 mbar using an inline venturi tube (SMC), solenoid valve (Parker Hannifin), and a digital air regulator (ProportionAir) controlled by an Arduino Uno for rapid pressure switching [26, 31]. A three-barreled, square cross-section solution manifold (3SG700-5, Warner Instruments) attached to a piezoelectric translator (Burleigh Instruments) was used for cell perfusion similar to many that have been previously published [61, 62]. Barrels of the solution manifold were connected to 8-valve solution changers (Hamilton Modular Valve Positioner). Custom LabVIEW code (National Instruments) integrating manipulators (electrode and microscope), camera view of the microscope stage, pressure control box, piezoelectric translator, and solution valves was implemented to control the rig and enable automated experimentation. Communication between the computer and the amplifier, piezoelectric translator and solution changers was achieved using a Data Acquisition System (DAQ) (BNC-2110, National Instruments) with several analog and digital interfaces. Representative approach is seen in Figure 2.2.

2.3.1 Transiently Expressing HEK cells

Human Embryonic Kidney cells (HEK-293) (CRL 1573, ATCC; hereafter HEK cells) and a stable GABA_AR-expressing cell line were cultured in DMEM (Cat 10566016, ThermoFisher Scientific) supplemented with 10% fetal bovine serum (FBS), 10 U/ml peni-

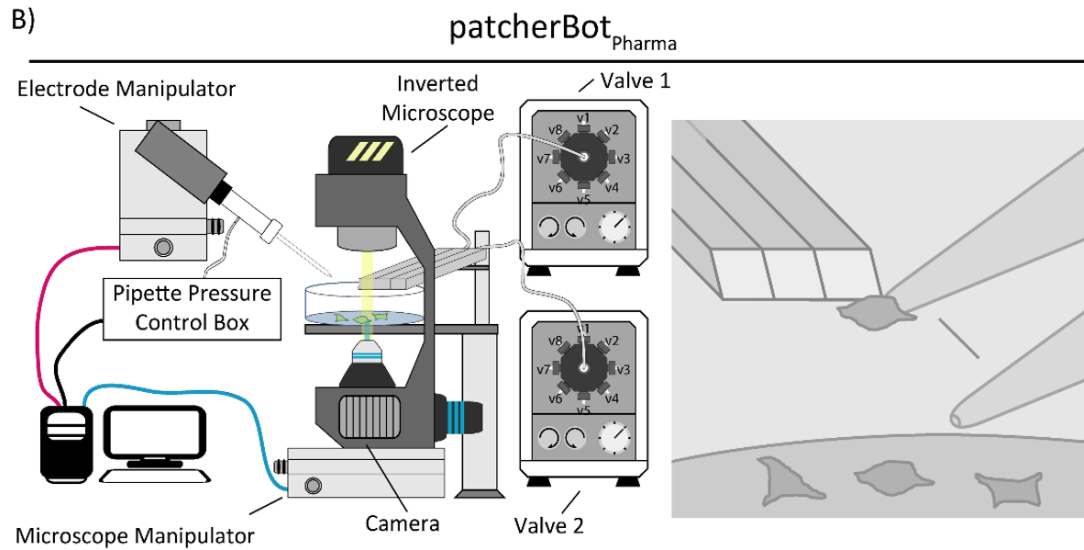


Figure 2.2: Cartoon of the patcherBot_{Pharma}, assembled from an inverted microscope, high sensitivity camera, custom pressure control box, quasi-4 axis electrode manipulator, a motorized microscope manipulator, two solution valves, and a solution exchange manifold.

cillin, and 10 $\mu\text{g/ml}$ streptomycin and maintained at 5% CO₂ in a 37°C incubator. For use on the electrophysiology rig, heterologous cells were plated on poly-D-Lysine (PDL) coated glass coverslips (0.1-0.5 mg/mL, Warner Instruments). Recombinant N-methyl-D-aspartate (NMDA) receptors were transiently expressed from complementary DNA (cDNA) encoding rat GluN1-1a (hereafter GluN1, U08261), and GluN2A (D13211). Calcium phosphate was used to transfect HEK cells in a 24-well plate with 500 ng of DNA at a ratio of 1:1:5 (GluN1:GluN2A:GFP). Four hours after transfection, N-methyl-D-aspartate Receptor (NMDA_AR) antagonists D,L-2-amino-5-phosphonovalerate (200 μM , DL-APV) and 7-chlorokynurenic acid (200 μM) were added to the culture medium to decrease the cytotoxic effect of NMDA_AR expression.

2.3.2 Stably Expressing HEK cells

cDNAs for mouse Gabra1, Gabrb2, and the long form of Gabrg2 were subcloned into the pAC156 plasmid, a generous gift from Albert Cheng. The cDNAs were driven by an EF1alpha promoter. A PGK promoter-driven puromycin resistance cassette was also

present in pAC156; both cassettes were flanked by piggybac transposon arms. All three plasmids were co-transfected with the mPB piggybac transposase into HEK 293 cells, selected by puromycin, and sorted into single cells. Clones were assayed for Gabra1, Gabrb2, and Gabrg2 expression by immunofluorescence, and one clone was expanded for further study and use in this manuscript. Trypsin was used to dissociate the cells and plated on the same coverslips, as mentioned above, 24-72 hours before experimentation (shorter time and less PDL for lifted cell, and the inverse for excised patches).

2.3.3 Whole-cell voltage-clamp recordings

Whole-cell voltage-clamp recordings were performed with thin-walled borosilicate glass electrodes (3-6 M Ω , TW150F-4, World Precision Instruments) filled with solution containing (in mM) 110 Cs-gluconate, 30 CsCl, 5 HEPES, 4 NaCl, 0.5 CaCl₂, 2 MgCl₂, 5 BAPTA, 2 NaATP, 0.3 NaGTP (pH 7.35). The extracellular recording solution contained (in mM) 150 NaCl, 10 HEPES, 3 KCl, 0.5 CaCl₂, 1 MgCl₂, and 0.01 EDTA (pH 7.4). Whole cell recording from primary cortical neurons (examples showing alternative experiment paradigm in the supplemental) were obtained utilizing an internal solution, containing (in mM) 115 K-gluconate, 20 KCl, 10 HEPES, 2 Mg₂ATP, 0.3 NaGTP, and 10 Na₂Phosphocreatine (pH 7.35), and external solution stated above but with 1mM CaCl₂. The electrode cleaning solution (2% Tergazyme in water) was made fresh daily. Cleaned electrodes were washed in appropriate external solution. All solutions were filtered (0.45 μ m or 0.22 μ m). Responses were recorded using a Multiclamp 700B (Molecular Devices), filtered at 10 kHz (-3 dB), and digitized at 20 kHz.

2.3.4 Analysis and Statistics

Whole-cell rapid solution exchange experiments were analyzed using custom algorithms (Matlab, Mathworks). The desensitization and deactivation time courses were fitted by exponential functions based on receptor type. For NMDA_AR desensitization and GABA_AR

deactivation, they were fit by one exponential function,

$$I = A * e^{\frac{-\text{time}}{\tau}} \quad (2.1)$$

where I was the current response, A was the amplitude of the response, time is the duration after the peak response or removal of agonist, τ is the time constant, and C is an offset constant. NMDA_AR deactivation and GABA_AR desensitization was fit with a dual exponential function,

$$I = A_f * e^{\frac{-\text{time}}{\tau_f}} + A_s * e^{\frac{-\text{time}}{\tau_s}} + C \quad (2.2)$$

the two exponentials are designated as fast (A_f, τ_f) and slow (A_s, τ_s). For dual exponential fits, a weighed tau (τ_w) was calculated,

$$\tau_w = \frac{A_f * \tau_f + A_s * \tau_s}{A_f + A_s} \quad (2.3)$$

The Fisher's exact test, two tailed, was used where noted. Mean \pm SEM (standard error of the mean) is used unless otherwise noted.

For efficient traditional pharmacological experimentation, one must ensure the viability of the available cell pool during sequential experimentation. Especially for ligand-gated ionotropic receptors, this is achieved by lifting cells or pulling patches from the coverslip and performing solution application far from the cells remaining on the coverslip (Figure 2.3B). This procedure can be more straightforward than translating the manifold to the cell locations. We first set out to ensure that this could be done reproducibly by the robotic system, since achieving accurate placement of all components is essential for efficient data collection with minimal operator effort. We first verified that the patcherBot_{Pharma} could traverse the recording electrode distances on the millimeter scale while ensuring micrometer scale precision at the interface of a multibarrel flow pipe, given that piezoelectric translators typically have a maximum range from 100-300 μm . This is especially important since in

one complete cycle of the patcherBot_{Pharma} operation (patching, experiment manipulation, and electrode cleaning) the electrode will translate roughly 150 mm.

The patcherBot_{Pharma} needs to achieve this high level of accuracy and precision at the solution manifold without necessitating manual, time-intensive error correction. Typically, the placement of the electrode at the solution interface is established visually at a predesignated location (beginning of the recording session) then test pulses are conducted to ensure proper placement taking at least 30 second for a highly skilled operator. To test the ability to return to the critical location, we translated the electrode through the various positions required to patch sequentially (4x). After each cycle, the solution exchange around an open-tip electrode was measured by triggering a piezoelectric translation of the solution manifold (exchanging extracellular buffer and a partial salt solution containing 50% extracellular buffer and 50% H₂O). We found that the electrode could be repeatably positioned while retaining the fast solution exchange time, and without placement errors that can lead to recording artifacts (i.e., straying into the adjacent lane before the jump, Figure 2.3C).

Lifting cells in the whole-cell configuration and pulling outside-out patches are two of the most common methods of studying ligand-gated ionotropic receptors using rapid solution exchange manifolds. For lifting cells in the whole-cell conformation, we implemented a segmented (100 step) spiral translation method while applying a light suction on the pipette (-40 mbar, Figure 2.3D,E). In applying this method, we were able to reliably lift cells while retaining the high-resistance seal that was obtained while breaking through (Figure 2.3F). For pulling outside-out patches, we implemented a segmented (100 step) arc translation method while the pipette was at atmospheric pressure (Fig. 2G,H). In applying this method, we were able to repeatedly pull outside-out patches, achieving the characteristic low capacitance and high resistance of this patch-clamp conformation (Figure 2.3I).

With these new functionalities, this system proved capable of performing rapid solution exchange experiments as well as executing precise solution application. To demonstrate these capabilities, we recorded from two synaptic ligand-gated ionotropic recep-

tors, GABA_AR and NMDA_ARs, using the patcherBot_{Pharma} (Figure 2.4). As expected, the patcherBot_{Pharma} was capable of recording NMDA_AR responses from transiently transfected HEK cells that were lifted off the bottom as well as from outside-out patches excised from HEK cells (Figure 2.4A). Additionally, the patcherBot_{Pharma} was capable of recording GABA_AR responses from stably expressing cells, including both long agonist applications as well as brief agonist applications (5 ms, Figure 2.4B). In addition to this experimental protocol, the patcherBot_{Pharma} is programmed to conduct many other commonly used solution exchange protocols (Supplemental Fig. 1) as well as voltage-clamp and current-clamp protocols. These can be employed to measure neuronal activity or study specific voltage-gated channels expressed in heterologous cells. The patcherBot_{Pharma} can implement these experimental protocols on adherent cells, lifted cells or patches pulled from cells, paired with solution control to measure channel responses in different conditions (Figure 2.7).

We subsequently performed a series of pharmacology experiments on GABA_AR and NMDA_ARs where we recorded rapid agonist application to excised outside-out patches to assess patcherBot_{Pharma} performance on the minimum processes required in an experiment (Table 2.1). Assessment of the overall performance of the patcherBot_{Pharma} for both glutamate and GABA receptors revealed that a giga-ohm resistance patch (gigaseal patch) was obtained 81.2% of the time (108 of 133 attempts). After a gigaseal was achieved, successful break-in occurred 96.3% of the time to establish the whole-cell conformation (104 of 108 gigaseals). After whole-cell configuration stabilization, the success rate of excising an outside-out patch was 76.0% (79 of 104 whole-cell conformations). The successful completion of an experiment based on every outside-out patch pulled was 74.7% (59 of 79 outside-out patches). Subsequent failure to complete an experiment after obtaining an outside-out patch was due either to the lack of detectable receptor response upon agonist application or patch integrity breakdown after initiating the experimental recordings. Taken together the overall success of the patcherBot_{Pharma} was 44.4% (59 of 133 attempts). In examining the nature of failed experiments, we found that the yield of the system is largely

based on two main factors, electrode placement and biological factors.

One major contributing biological factor to experiment failure was the efficiency in the transient cDNA transfection process used to express the NMDA_ARs. Overall, there was a higher success rate in achieving a high-quality recording from the stably expressing GABA_AR cells (31 successes out of 51 total attempts) than the transiently transfected NMDA_AR cells (28 successes out of 82 total attempts, Fisher's exact test, $p = 0.0039$). Despite expression of GFP, which was coexpressed with NMDA_AR subunits, 14 of the 42 pulled patches did not have a current response of a sufficient amplitude. By contrast, the GABA_AR cell line had a trend of higher reliability: only 5 of the 31 outside-out patches failed to have detectable current. This suggests that enhanced yield could result from improved molecular biology methods. Outside of those biological inefficiencies, monitoring the operation of the patcherBot_{Pharma} suggests that the failures at the gigaseal formation step and the outside-out patch-pulling step are due to slight errors (1-3 μm) in optimally placing the electrode. In this dataset, we had performed a subset of experiments where an experimenter manually intervened by controlling the final placement of the electrode once the patcherBot_{Pharma} had positioned the electrode 100 μm above the next selected cell. In these operator-assisted experiments, we observed that the gigaseal yield was higher with 97.2% and the patch-pulling yield was 88.6%. Specifically, in obtaining gigaseals, the operator-assisted trials resulted in 35 successes from 36 attempts compared to 9 successes from 15 attempts (Fisher's exact test, $p = 0.0016$). Additionally, in excising outside-out patches, the operator-assisted trials resulted in 31 successes from 35 attempts compared to 6 successes from 9 attempts (Fisher's exact test, $p = 0.1383$). The overall yield (successful experiment compared to attempt) of these operator-assisted runs was 69.4% (25 good experiments of 36 attempts), as compared to the 40% success rate of the other experiments (6 good experiments of 15 attempts, Fisher's exact test, $p = 0.0645$). Fully automated electrode placement implemented in the patcherBot_{Pharma} relies on machine vision using camera pixel intensity cross-correlation methods to align a previously stored image of the cell and electrode to

make corrections at the beginning of each attempt. These methods work well in placing the electrode somewhere on a cell ($10 \mu\text{m}$ precision) without operator intervention but lack the accuracy to place it optimally ($\pm 1 \mu\text{m}$), which appears to have a large impact on overall success. In addition to the losses in efficiency, the machine vision processes are slow due to the necessity to move the electrode or microscope to check for positioning errors. The process time during fully automated patcherBot_{Pharma} operation takes on average 267 ± 35 s (mean \pm Standard Deviation, SD) to correct the manipulators, land the electrode on the cell and break-in to the whole-cell conformation. This is compared to 74 ± 10 s (mean \pm SD) for the operator-assisted patcherBot_{Pharma}, where robotic translations move the stage to the next cell and places the electrode just above the cell ($100 \mu\text{m}$) before the operator places the electrode on the cell and, in this case also, forms a gigaseal followed by the automated break-in process. Thus, the patcherBot_{Pharma} can operate fully autonomously, but the speed and performance can be improved by operator intervention during key steps with the current techniques of position error correction.

Operating in this manner, with minor manual interaction, the patcherBot_{Pharma} can collect experiment electrophysiology recordings proficiently, which is demonstrated by a representative run of the patcherBot_{Pharma} from the results mentioned previously (Figure 2.5). In this experimental run, the patcherBot_{Pharma} was programmed to collect four-phase recordings. During each phase, five technical replicate sweeps were collected, a 10 sec sweep with agonist applied for 0.5 sec. Following each set of recordings, the patch was blown off with high pressure and the open-tip exchange time was determined to validate the electrode positioning. On average, the recording time and position validation totaled 11.2 min. If the patcherBot_{Pharma} detects inadequate patch formation, after the outside-out patch procedure, it terminates the recording and moves on to the next cell, spending only 1.4 min in doing so. Over this 3.8 hour recording session, highlighted in Figure 2.5, 15 cells were attempted to be patched, yielding 12 successful recording sets. During this time, the operator only interacted with the patcherBot_{Pharma} for 15.5 min during recording (7.1% of the experimen-

tal run time) after the 10.3 min of calibration and cell selection. The patcherBot_{Pharma} was recording data for 2.6 hours, which amounts to 72.0% of the operation time. The GABA_AR responses that were collected were of high quality and similar to those previously reported (Figure 2.5B, Table 2.3). Additionally, the placement of the electrode resulted in consistent solution exchange times after each patch recording (Figure 2.5C).

Next, we performed a case study (Figure 2.6) where we sought to measure the main actions of a widely used anesthetic, propofol (PRO), to highlight the operational procedure and capability of the patcherBot_{Pharma} in performing an extended, tedious patch-clamp electrophysiology experiment. Propofol's main clinical actions are produced by prolonging the deactivation of GABA_AR and have been well characterized [63, 64]. We ran the patcherBot_{Pharma} with operator assistance for electrode placement (Figure 2.6A,B) followed by manual patch formation, to optimize the time of biological data collection by the patcherBot_{Pharma}. We set out to collect an 8-point concentration response curve of propofol's effect on GABA_AR deactivation, and we split it into two sets and included a propofol-free control before and after drug application (Figure 2.6C). In four, half-day recording sessions (2 per each concentration set) totaling 12.95 hours of patcherBot_{Pharma} operation, we attempted 42 recordings, obtained 39 gigaseal patches, achieved 28 whole cell conformations, pulled 24 successful outside-out patches, and completed 18 experiments (including 6 incomplete) that yielded 113 data points (Figure 2.6D-E, Table 2.4, Table 2.5). After eliminating the recordings with too large a leak current, too small a response amplitude, or recording artifacts, we were left with 71 data points that were used to calculate the concentration-response relationship of propofol's ability to prolong the deactivation of GABA_ARs ($EC_{50} = 11.8 \pm 4.6 \mu\text{M}$, Figure 2.6D-E).

Of the 12.95 hours of recording, the operator interacted with the patcherBot_{Pharma} for 2.49 hours and the patcherBot_{Pharma} collected experimental recordings for 9.07 hours, with an additional 1.39 hours of other automated processing (Table 2.4). The 2.49 hours of operator interaction includes cell selection, solution maintenance, electrode placement on the

cell, and gigaseal formation. In each iteration of the patcherBot_{Pharma} process, it spent 1.99 minutes cleaning the electrode and the operator spent 2-3 minutes placing the electrode on the cell and establishing the whole-cell conformation. If everything was successful, the patcherBot_{Pharma} would then proceed to collect the experimental data — in total a 24.6 minute process. If there was an issue with the stability of the patch during the process of pulling the outside-out patch (1.73 min process), the patcherBot_{Pharma} would clean the electrode and be ready for the next attempt in less than 2 minutes. Although the experiment yield was not overly high (24/42 attempts were successful) this did not greatly hinder the performance of the patcherBot_{Pharma} (Table 2.6). If every patch attempt was successful, the theoretical maximum number of experiments the patcherBot_{Pharma} could have performed in 12.95 hours was 25.8, which is only modestly higher than the 18 that we were successfully performed (70% full experiments performed divided by the maximum). Moreover, the rate of data collection, in terms of operator effort, was 2.1 minutes per data point. Should patching efficiency be improved further, the theoretical minimum of operator effort can be reduced to 0.97 minutes per data point.

2.4 Discussion

Patch-clamp electrophysiology research is a powerful technique, yet even for skilled practitioners, the complexity and effort required for comprehensive pharmacology experiments (pharmacological screening or evaluation of full concentration-response relationships) can be impractical. Here, we have demonstrated the capabilities of the patcherBot_{Pharma} for ligand-gated ionotropic receptor pharmacological screening, which makes patch-clamp electrophysiology experimentation rapid, less skill intensive, and more reliable. The automation of the patcherBot_{Pharma}, namely precise and accurate electrode translations, solution handling, electrode cleaning, and rapid solution exchange greatly expands the repertoire of experiments that the patcherBot can perform. This allows one to conduct nearly any pharmacological experiment typically performed on ligand-gated or voltage-gated ion

channels using the patcherBot_{Pharma} (e.g. Figure 2.7 and Figure 2.8). Additionally, the patcherBot_{Pharma} has the flexibility to be retooled as needed based off a traditional patch-clamp rig and can run autonomously or with minimal operator intervention to suit the experimental situation. Thus, the patcherBot_{Pharma} could be set up to patch adherent cells and applied compounds via the bath input, if desired, and the full automated capabilities of the system will be retained if all test compounds can be fully washed out.

The patcherBot_{Pharma} has very high yield (80-100%) of obtaining giga-ohm resistance patches and of breaking-in to achieve the whole-cell patch conformation. The methods we have employed to lift isolated patch-clamped cells and to pull outside-out patches are highly reliable (70-90% yield). These capabilities allow the patcherBot_{Pharma} to spend more time performing the intended electrophysiology experiment and less time in the process of manually guiding the position of the patch electrode throughout the course of the full experiment. With this improved system, the primary determinants for whether a particular experimental attempt concludes in a successful recording, relies more on biological factors than robotic or operator factors. In our experiments with heterologous expression systems (namely transfected HEK cells), the yield in high quality recordings, with high receptor expression, of the patcherBot_{Pharma} reaches 60-70% of the cells attempted. With this high efficiency of data collection, we could rapidly replicate previous datasets by reducing the time it takes to produce an 8-point concentration response curve of the effects of propofol on GABA_AR deactivation from weeks/months of recording down to 13 hours of recording.

This system retains the full capabilities of a traditional electrophysiology rigs. We observed solution exchange times, with our larger three-barreled manifold, in the low millisecond range (\sim 1-2 ms), which could be reduced further ($<$ 1 ms) using different solution manifolds ([61, 62]). This allows for accurate experimentation and can be used to study rapidly desensitizing receptors, which cannot be measured on commercially available multi-well high-throughput patch-clamp instrumentation. The patcherBot_{Pharma} system largely comprises typical components of a conventional electrophysiology rig (Table 2.2),

and thus does not require a substantial or prohibitive cost to upgrade. Running costs are low, comparable to the cost of operating a traditional patch-clamp rig, and primarily include the cost of the preparation (cell culture costs) and compounds being evaluated. There are no additional changes in running costs based on each data point collected, except for reduced glass consumption and perhaps reduced preparation costs that come with more efficient recording. However, as the patcherBot_{Pharma} can be in operation for extended periods of time and can execute experiments at a high rate, the running costs based on each day of operation may, in fact, be higher due to the increased bath solution usage and increased use of pharmacological compounds.

There are several improvements to the patcherBot_{Pharma} that could further increase its capabilities and productivity. Enhanced machine vision correction methods could allow for more precise placement of the electrode with less computation time thus increasing the unattended success rate and reducing human effort. Algorithms for cell detection could be employed to make cell selection agnostic, with further reduction in human effort and bias [65]. Repeatable collection of data will aid in meta-analysis of experiments, which could identify unrecognized factors that influence experimental results or experimental variability.

The patcherBot_{Pharma} facilitates pharmacological experimentation on ligand gated channels through increased productivity and the ability to address labor-intensive questions (collecting multiple concentration data points or testing more constructs). This allows more complex experimental protocols that include increased number of replicates and more controls. Many neuroscience studies have been cited as having low power in their experimental design [66], which could be rectified by utilizing the patcherBot_{Pharma}. Additionally, the patcherBot_{Pharma} reduces the chance of human bias when collecting data, as the experiment protocols are explicitly defined prior to experiment execution. Moreover, methods to introduce blinding in the experimental design could be employed along with automated analysis to allow one to easily jump to the final analyzed data point after conducting the

experiment. The data collected by the patcherBot_{Pharma} might be more reproducible due to enhanced transparency, as the full patcherBot_{Pharma} experiment data log could be documented along with the results [67]. With the reduction in human effort that comes with operating the patcherBot_{Pharma}, it becomes feasible that a single person could operate multiple patcherBot_{Pharma} at once for increased data collection. In summary, the patcherBot_{Pharma} enhances the capabilities of a researcher utilizing patch-clamp approaches by decreasing operator interaction time, reducing human bias, increasing experiment yield, allowing more complicated experimental design, and enabling experiments that require high volumes of recordings.

2.5 Additional Pharmacology Experimentation

Table 2.1: GS, gigaseal. WC, whole cell. O-O, outside-out. Success percentage is calculated for each step (i.e. WC success is calculated based on the number of GS counts), except for the overall exp. success. An attempt is deemed a successful experiment if the full experiment set was collected, in a few instances the patch was pulled, deemed to be successful but failed during the experiment data collection.

	Attempts	GS	WC	O-O Patch	Successful Experiment	Zero Current	Overall Exp. Success
All GABA _A R and NMDAR	133	108	104	79	59	19	
NMDAR (transient)	82	64	60	42	28	14	
GABA _A R (stable)	51	44	44	37	31	5	
(computer vision)	15	9	9	6	6	0	
(operator assisted)	36	35	35	31	25	5	
All GABA _A R and NMDAR		81.2%	96.3%	76.0%	74.7%	24.1%	44.4%
NMDAR (transient)		78.0%	93.8%	70.0%	66.7%	33.3%	34.1%
GABA _A R (stable)		86.3%	100.0%	84.1%	83.8%	13.5%	60.8%
(computer vision)		60.0%	100.0%	66.7%	100.0%	0.0%	40.0%
(operator assisted)		97.2%	100.0%	88.6%	80.6%	16.1%	69.4%

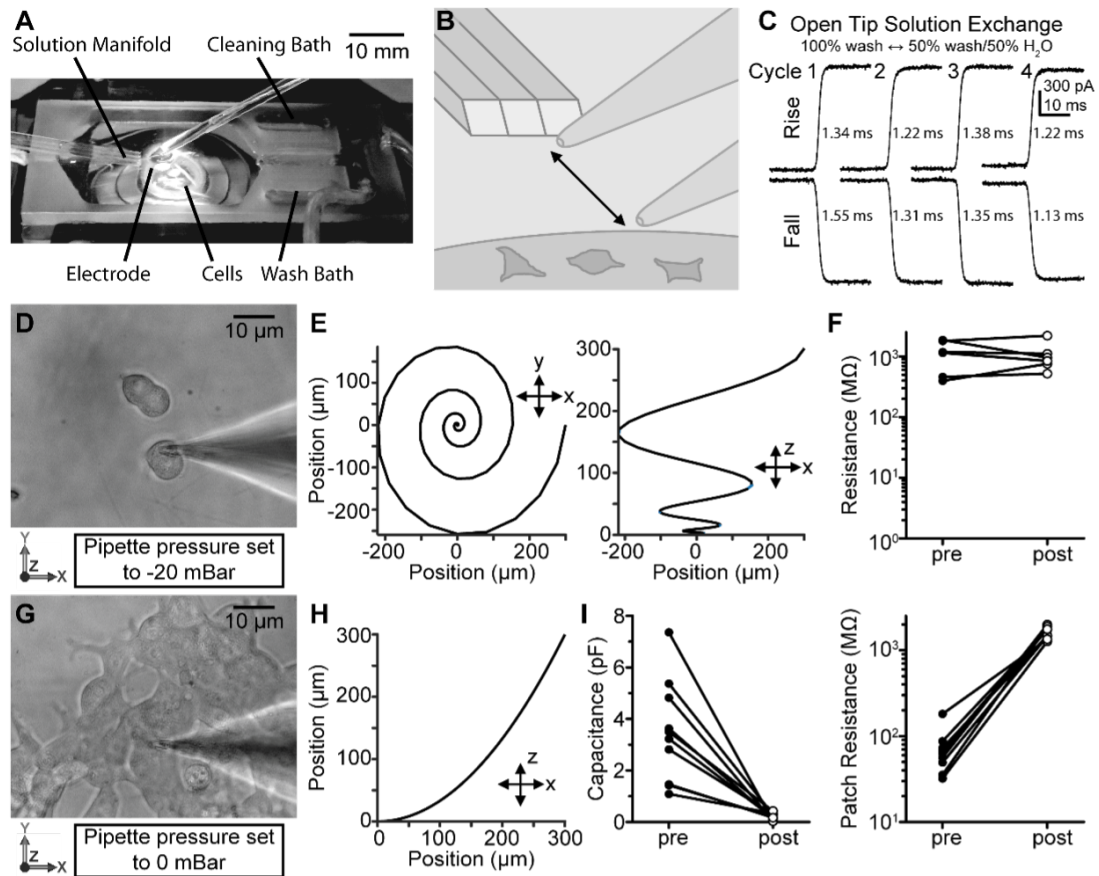


Figure 2.3: Repeatability of the physical manipulations required for fast-solution exchange electrophysiological experiments. (A) Image of the recording chamber. (B) Cartoon illustrating the large distances (e.g. X-Y mm scale) the electrode must translate during experimentation. (C) Open-tip solution exchange times, using piezo-electric translator, across many repeated experimental cycles (cell locations, solution manifold interface, cleaning/wash bath). (D-F) Cell lifting procedure. (D) Image of an isolated cell in the whole-cell conformation before lifting (isolated cells are more reliably lifted than those with cellular processes to adjacent cells). (E) Spiral path (100 discrete segments) employed to lift isolated cells. (F) Resulting resistance plot showing a high resistance seal is robustly maintained during the lifting process. (G-I) Patch pulling procedure. (G) Image of a cell in the whole-cell conformation before pulling an Outside-out (O-O) patch. (H) Arc path (100 discrete segments) employed to pull outside-out patches. (I) Resulting capacitance and resistance plots showing successful high-resistance, low-capacitance outside-out patches. We speculate the low resistance prior to pulling the outside-out patches is due to electrical connections due to gap-junctions between multiple cultured cells in physical contact with one another.

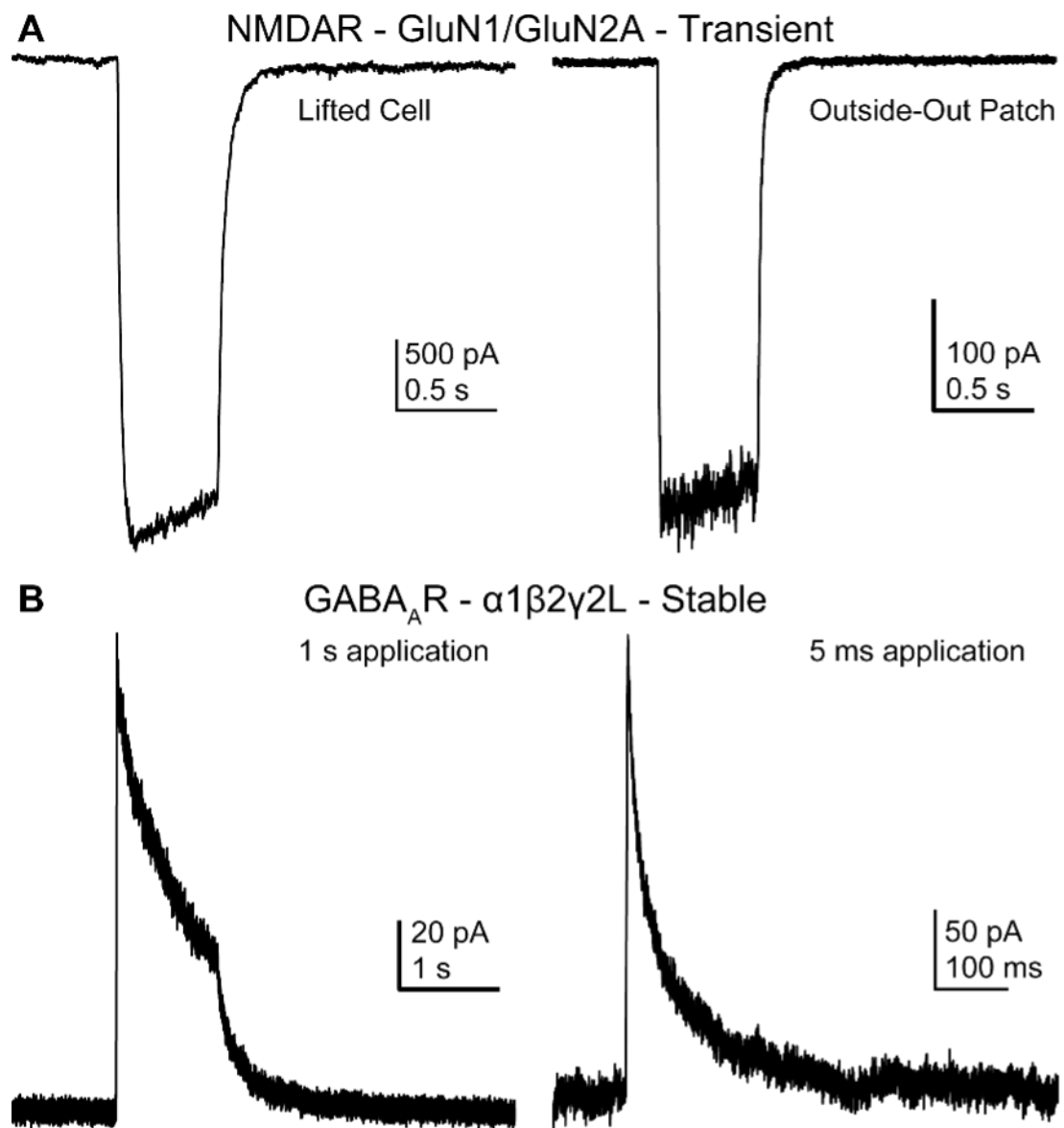


Figure 2.4: Exemplary fast-solution exchange electrophysiological experimental results. (A) NMDA_AR responses from transiently transfected HEK cells stimulated by 100 M glutamate and 30 M glycine. Recordings are from a lifted whole cell (left) and an outside-out patch using a 4 M electrode (right), at -60 mV in 0 mM Mg²⁺. (B) GABA_AR responses from stably transfected HEK cells (122L) stimulated by 1 mM Gamma-Aminobutyric acid (GABA). Recordings are from a lifted whole cell (left, 1 s application) and an outside-out patch (right, 5 ms application)

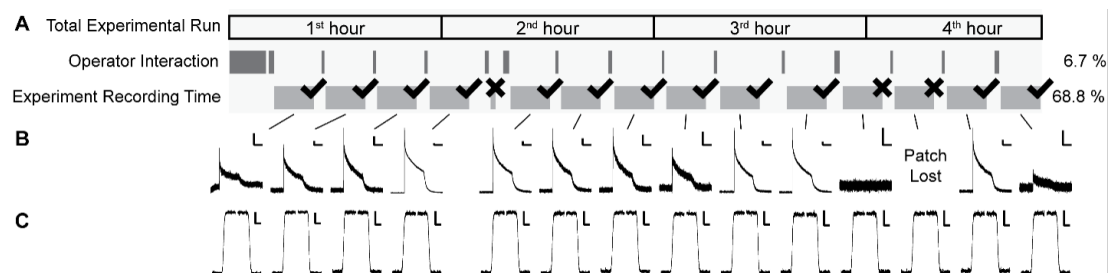


Figure 2.5: (A) Timeline of experimental progress. The time periods of operator interaction with the patcherBotPharma and recording duration are highlighted, along with recording outcome. (B) GABA_AR responses (1 mM GABA, 1 s application) from all successful outside-out patches pulled. Scale bars indicate 20 pA and 0.5 s. (C) Post-experiment open-tip position validation utilizing a 50% H₂O/50% wash solution. Scale bars indicate 200 pA and 20 ms. The average (\pm SD [Range]) 20-80 rise and fall times for piezoelectric jumps were 3.06 ± 0.78 [1.30 4.11] and 3.56 ± 0.32 [2.27 6.55].

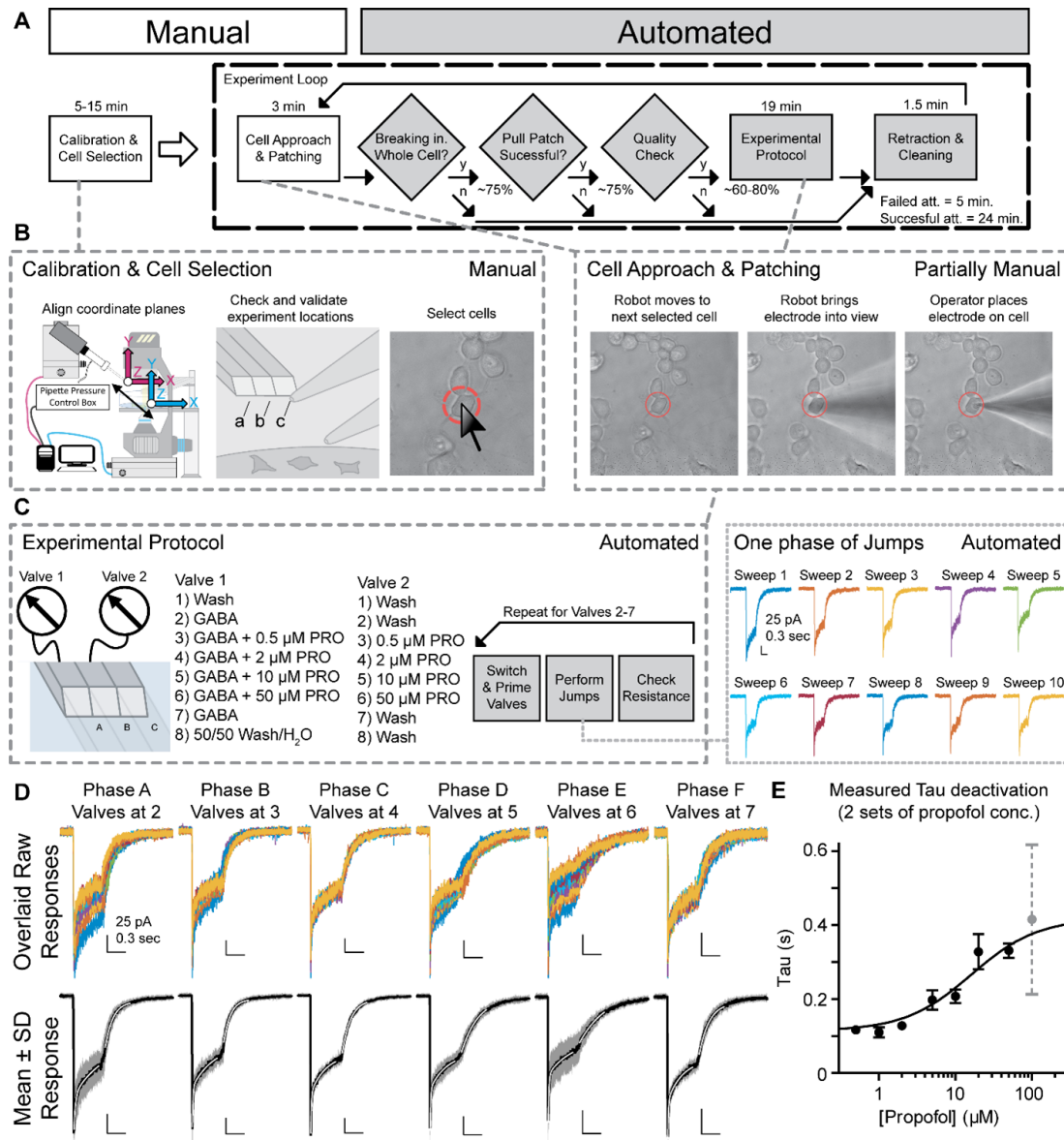


Figure 2.6: $GABA_A$ R propofol deactivation time-constant concentration response case study; the patcherBot_{Pharma} has the capability to collect pharmacological data at an accelerated rate. (A) A flowchart illustrating the patcherBot_{Pharma} operation, timing, and success rate of individual steps. The manual (white boxes) and automated (grey boxes) steps are indicated. (B) A more detailed depiction of the manual steps is shown. (C) A more detailed look at the experimental protocol step of the patcherBot_{Pharma} process. In this case, there were 6 sets of solutions that would be used during each experiment (2 control and 4 propofol solution sets, detailed on the left). Each phase of each experiment would start with the valves changing to the next set to be tested, with a wait step to allow for the solutions to be primed, followed by the collection of 10 replicates of the intended jump protocol (right).

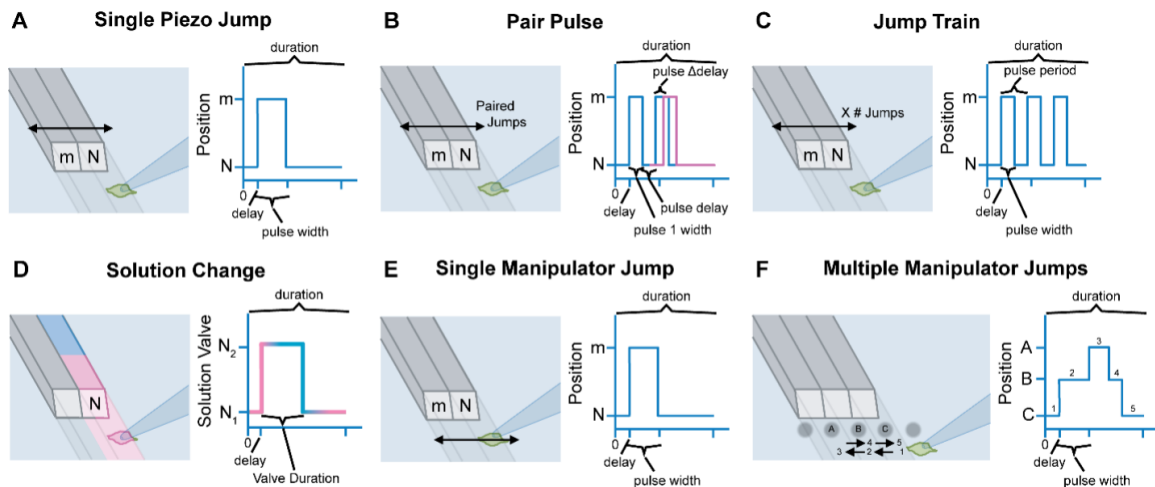


Figure 2.7: Solution exchange protocols programmed into the patcherBot_{pharma} can utilize either movement of the piezo-mounted manifold, or movement of the manipulator holding the pipette. (A-C) A piezoelectric translator is controlled by a filtered voltage pulse signal, in either individual pulses (A), paired pulses with an optional increasing delay (B), or a train of applications with variable pulse width and period (C). (D) A slow solution exchange experiment can be performed where the solution valve is switched at a specific time during the experiment to record the slow transition of the application of a second solution. (E) The smooth motion from the electrode manipulator can be used to perform a similar solution application to (A), but with a broader range of motion allowing multiple barrels to be used. (F) Any number of manipulator transitions can be combined to produce complex solution applications.

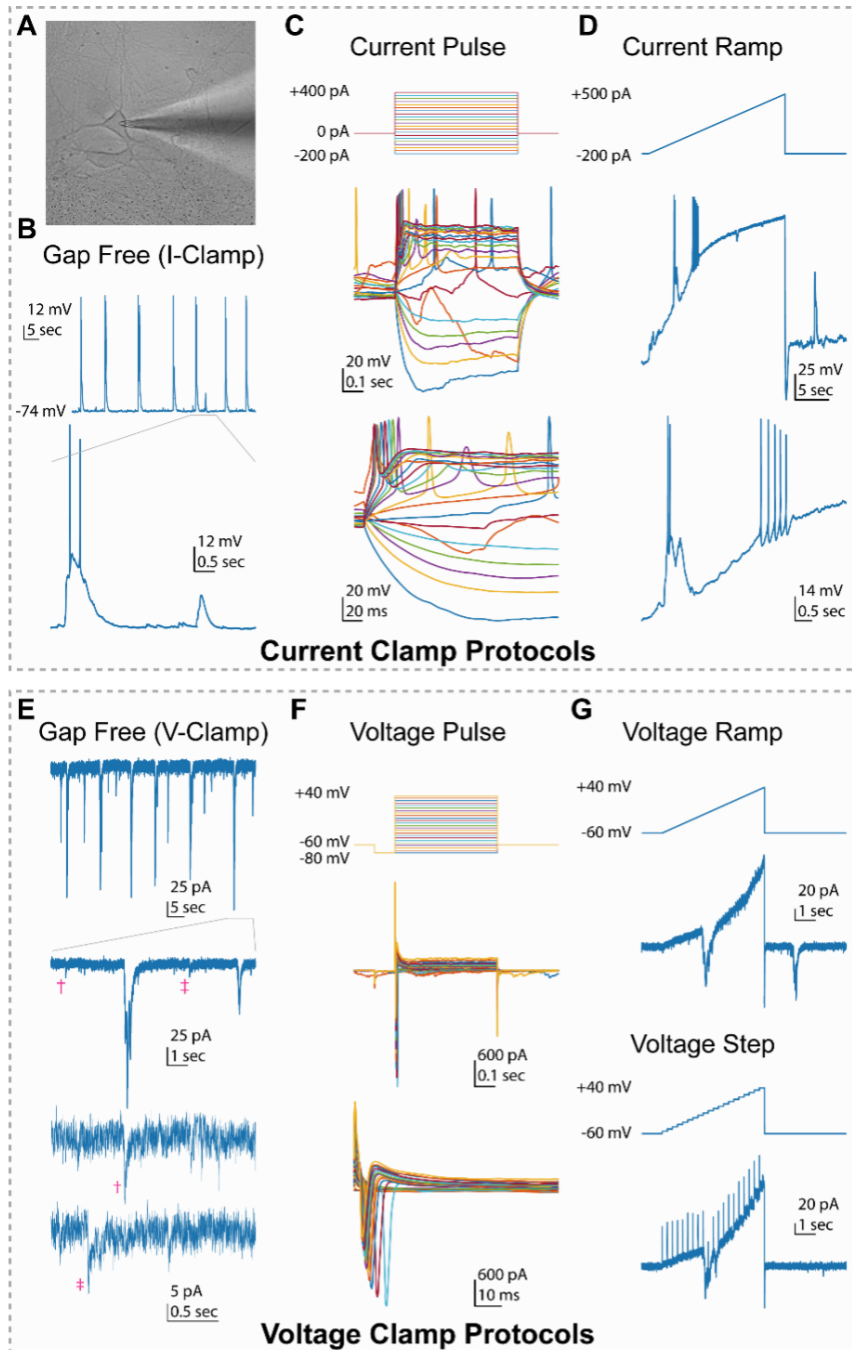


Figure 2.8: (A) Typical bright-field image of DIV14 cortical neuron during a recording. (B) An exemplary current-clamp gap-free recording ($I_{injection} = 0$ pA), showing spontaneous network activity, bursting, and the resting membrane potential (-74 mV). (C-D) A current-pulse protocol and a current-ramp protocol, illustrating the amount of injected current is required to induce an action potential. (E) An exemplary voltage-clamp gap-free recording ($V_{holding} = -60$ mV), showing spontaneous network activity and even putative spontaneous events (pink staffs). (F) Two-part voltage-pulse protocols can elucidate voltage-gated channel responses. (G) Voltage-ramp and -step protocols can also be applied to measure membrane properties.

Table 2.2: The typical components required for a patch-clamp rig that can perform rapid solution exchange experiments are shown in the traditional electrophysiology rig column and compared to the patcherBot_{Pharma}. For the traditional electrophysiology rig other components are available and could result in a lower total cost. Many of the listed prices are quoted from www.autom8.com, direct prices from the manufacturers may be less. † The patcherBot_{Pharma} does not require any specific types of this component. ‡ Suggested Minimum Requirements: 32 GB RAM, i7-8700K CPU @3.70GHz, Additional GPU

Component	Traditional Electrophysiology Rig		patcherBot _{Pharma} Rig		Notes
<i>Vibration Isolation Table</i>	CleanBench Lab Table	\$5,000	CleanBench Lab Table	\$5,000	†
<i>Faraday Cage</i>	Custom	\$1,000	Custom	\$1,000	†
<i>Microscope</i>	Ziess Axiovert 200	\$19,000	Ziess Axiovert 200	\$19,000	†
<i>Computer System</i>	Any	\$1,500	Dell‡	\$3,500	The patcherBot _{Pharma} requires a high-performance computer.
<i>Electrode Manipulator</i>	Sutter MP-285	\$10,000	Scientifica PatchStar	\$10,000	The patcherBot _{Pharma} requires Scientifica Manipulators.
<i>Microscope Manipulator</i>	Siskiyou Manual Microscope translator	\$4000	Scientifica Motorized XY Stage + Z-focus module	\$13,000	The patcherBot _{Pharma} requires Scientifica Manipulators.
<i>Peristaltic Pump</i>	-	-	Gilson MiniPuls 3	\$3,000	This helps keep the bath solution flow constant for extended periods of time but not necessary for in a traditional electrophysiology rig.
<i>Rig Platform</i>	Custom	\$300	Custom	\$300	† The patcherBot _{Pharma} has a custom machined piece of aluminum (24"x24"x10mm).
<i>DAQ</i>	Molecular Devices Digidata 1550B	\$8,000	National Instruments BNC-2110	\$2,000	The patcherBot _{Pharma} uses a National Instruments DAQ not the typical Molecular Devices Digidata.
<i>Amplifier</i>	Molecular Devices Axopatch 200B	\$15,000	Molecular Devices MultiClamp 700B	\$20,000	The patcherBot _{Pharma} requires a 700B Multiclamp for full functionality.
<i>GFP excitation LED System</i>	Thor Labs	\$1,000	Thor Labs	\$1,000	†
<i>Solution Valves</i>	Hamilton Manual Valves	\$400	Hamilton MVP Automated Valves	\$2,400	The patcherBot _{Pharma} requires computer controlled valves, whereas a traditional electrophysiology rig could use manual valves.
<i>Bath Chamber</i>	Warner Instruments	\$3,000	Warner Instruments	\$3,000	†
<i>Piezoelectric Translator</i>	Siskiyou Fast Piezo Perfusion Switcher	\$10,000	Siskiyou Fast Piezo Perfusion Switcher	\$10,000	† The Burleigh Instruments Piezoelectric translator is no longer available.
<i>Pressure Box</i>	-	-	Neuromatic Devices	\$6,000	The patcherBot _{Pharma} in this work used a custom pressure box, the pressure box produced by Neuromatic Devices as similar specification.
<i>Camera</i>	Thor Labs	\$500	QImaging, Retiga Electro	\$5,000	The patcherBot _{Pharma} requires a high sensitivity camera.
<i>Signal Filters</i>	Cygnus Technology FLA-01	\$2000	Cygnus Technology FLA-01	\$2000	†
<i>Software</i>	Molecular Devices pClamp	\$8000	National Instruments Labview	\$6000	
Total		\$88,700		\$112,200	

Table 2.3: Summary of activation and deactivation parameters of GABA_AR and NMDARs from Figure 2.4 and Figure 2.5.

		Rapid application of 1 mM GABA or Glutamate for 1 sec						
		Patch Leak	Response	Response	Desensitization	Desensitization	Deactivation	N
		(pA)	Peak Amplitude (pA)	Steady State Amplitude (pA)	Extent (SS/Peak %)	n Tau (ms)	n Tau (ms)	
GABA _A R	+40 mV	24.9 ± 18.7	586 ± 150	170 ± 54	26.4 ± 1.8%	681 ± 130	216 ± 29	12
	-60 mV	48.3 ± 36.1	173 ± 48	35.9 ± 13.6	24.8 ± 1.1%	965 ± 298	133 ± 6	12
NMDAR GluN2A WT	+40 mV	38.6 ± 32.1	271 ± 104	130 ± 68	34.2 ± 6.4%	388 ± 75	71.9 ± 11.0	11
	-60 mV	140 ± 42.6	326 ± 180	215 ± 139	54.8 ± 6.9%	984 ± 192	81.3 ± 18.4	7

Table 2.4: † The non-recording time is the time the robot is not performing the data collection protocol. ‡ This rate represents the total time the operator spent interacting with the patcherBot_{Pharma} during the entire experiment performance (cell selection, solution maintenance, electrode placement on the cell, and gigaseal formation). The theoretical maximal efficiency of data collection per the operator’s effort would be 0.97 mins of the operator’s time per data point. Each data collection phase equals the solution change time plus the data collection time, however the mean time per data point reflects the additional time needed to pull the patch and validate the jump at the end of the experiment averaged into the timing for each phase.

	Total Operation	Electrode Cleaning (Robotic Control)	Data Collection (Robotic Control)	Patch Establishment (Operator Control)	Non-Recording Time†
<i>Total Time (Percent)</i>	12.95 hrs	1.39 hrs (10.7%)	9.07 hrs (70.0%)	2.49 hrs (19.3%)	3.88 hrs (30%)
<i>Time Per Cycle (successful cycle)</i>		1.99 mins	24.6 mins	3.55 mins	5.54 mins
<i>Time Per Data Point (successful cycle)</i>			4.1 mins [‡] (~1 min solution change time) (1.67 min data collection)	2.1 mins [‡]	

Table 2.5: Concentration response of propofol (PRO) on GABA_AR activation and deactivation.

Rapid application of 1 mM GABA for 0.5 sec – Propofol concentration set 1						
GABA_AR	Patch Leak (pA)	Response Peak Amplitude (pA)	Response Steady State Amplitude (pA)	Desensitization Extent (SS/Peak %)	Deactivation Tau (ms)	N
GABA Control	20.9 ± 7.3	133 ± 36	51.1 ± 12.3	39.3 ± 2.0%	129 ± 11	8
0.5 μM PRO	28.9 ± 13.5	100 ± 20	40.4 ± 8.9	39.6 ± 1.3%	116 ± 13	8
2 μM PRO	16.7 ± 4.5	109 ± 32	45.6 ± 14.9	40.0 ± 1.7%	128 ± 13	6
10 μM PRO	18.8 ± 4.8	96.0 ± 25.2	42.1 ± 11.6	43.1 ± 2.2%	208 ± 20	6
50 μM PRO	16.0 ± 3.0	63.9 ± 17.8	23.5 ± 7.4	33.8 ± 2.7%	331 ± 21	7
PRO washout	15.9 ± 2.8	66.7 ± 22.6	29.2 ± 11.3	41.8 ± 1.7%	143 ± 25	6

Rapid application of 1 mM GABA for 0.5 sec – Propofol concentration set 2						
GABA Control	30.6 ± 6.2	93.6 ± 6.8	30.5 ± 8.1	31.8 ± 7.7%	130 ± 27	6
1 μM PRO	36.5 ± 6.4	72.2 ± 18.0	24.2 ± 6.6	34.9 ± 6.7%	110 ± 15	6
5 μM PRO	34.3 ± 8.2	37.8 ± 9.1	11.1 ± 2.4	30.0 ± 5.1%	198 ± 29	5
20 μM PRO	42.1 ± 8.0	21.5 ± 4.6	6.1 ± 2.2	25.2 ± 6.6%	328 ± 53	5
100 μM PRO	29.0 ± 5.9	8.9 ± 1.2	5.8 ± 7.5	-	415 ± 226	5
PRO washout	24.8 ± 10.1	20.1 ± 6.3	5.3 ± 3.4	25.2 ± 13.5%	129 ± 12	3

Table 2.6: † The theoretic maximum values were determined by taking the total operation time divided by the total time for one successful cycle. Since there are 6 collected data points per experiment, the theoretical maximum for total collected data points equals the number of experiments multiplied by a factor of 6.

	Counts	Yield	Theoretical Max[†]
Patch Attempts	42		
Successfully established gigaseals	39	93%	
Whole cell conformations obtained	28	72%	
Outside-out patches obtained	24	86%	
Experiments started	24	-	
Successful Experiments	18	75%	25.8
<i>Total Data Points Collected</i>	113		154.8
<i>Data Points Passed Quality Control</i>	71		

CHAPTER 3

INTEGRATE AUTOMATED PATCH CLAMPING FOR GENETICALLY ENCODED VOLTAGE INDICATORS AND EFFECTORS

3.1 Motivation

Protein sensors of membrane voltage have the potential to revolutionize the way in which we study brain activity because they provide direct report of neural activity. However, when compared to other existing protein sensors such as GCaMP, many genetically encoded voltage indicators (GEVIs) are still marred by relatively small fluorescence responses, photobleaching, or poor kinetics. The Genetically Encoded Neuronal Effectors and Indicators (GENIE) project team at HHMI Janelia performs large-scale mutagenesis of GEVI scaffolds and screens them to identify constructs with favorable fluorescent responses.

Conventionally, large-scale screening of GEVIs is performed with an automated microscope that performs field stimulation and concurrent fluorescence imaging in a 96-well plate [68]. While this approach was fruitful for screening GCaMP variants [69], it is limited for screening GEVIs. Namely, it cannot be used to infer fluorescence response to various membrane voltages, and cannot accurately provide information about sensor kinetics. Intracellular recording via patch-clamp electrophysiology provides a much richer dataset to characterize the indicators and is widely used as a "gold standard" measurement of GEVI function; however, the technique is laborious and low-throughput. The recent development of the autonomous "patcherBot" [31], a walk-away, robotic system that can perform many patch-clamp recordings sequentially has provided electrophysiologists with the opportunity to obtain patch-clamp recordings at a rate exceeding human capability. Using it for screening GEVIs could result in higher throughput and fewer man-hours (e.g. voltage imaging during electrophysiology recordings; workflow seen in Figure 3.1). However, whether the

patcherBot can perform high-quality recordings necessary for GEVI characterization was presently unknown.

Quantitatively, the GENIE project screens ~ 100 protein constructs per year using patch-clamp with one full-time employee. Practically, this translates to ~ 1 screened construct per day. On the other hand, computational simulations suggest that the patcherBot could screen 2-5 constructs per day, a potential two- to five-fold improvement in throughput Figure 3.2. Further algorithm refinements could further speed up the process. Towards this effort, in a commercial collaboration, the Finnish micromanipulator company, Sensapex, delivered to Janelia the first commercial patcherBot system in May 2019. Considerable efforts toward software, hardware, and biological optimization for GEVI screening was needed to ensure the system produced high-quality, consistent results for protein sensor screening (Figure 3.3). To ensure that the patcherBot@Janelia robot can be left completely unattended during experiments, there were improvements in cleaning of pipettes in order to ensure that pipettes could attain over 20 recordings in a screening experiment [32]. To improve data quality and throughput for screening, there was additional patch clamping refinement that included (1) mimicking best practices from trained electrophysiologists, (2) checking recording quality in real time and applying remedies if quality degrades, (3) automatically selecting cells based on health or fluorescence, and (4) performing auto-calibration. The robot will be used for large-scale studies of fluorescence response, kinetics, and photo-bleaching on the scale of ~ 4 constructs per day, or approximately 1,000 per year, and its deployment enabled high-throughput screening pipelines—particularly for sensitivity optimization of future GEVIs such as Voltron.

3.2 Introduction

Genetically encoded voltage indicators have served as an enabling technology for visualizing neuronal activity at unprecedented spatiotemporal resolution [44, 70, 71]. Nevertheless, optical imaging of voltage using GEVIs presents many challenges for the design of these

proteins. An ideal voltage sensor must concurrently fulfill many requirements, including but not limited to: (1) high sensitivity to membrane potential changes of a neuron, (2) fluorescence changes that are fast enough to follow and accurately report APs and (3) high degree of localization to neuron outer membranes. Further requirements may be desirable depending on application, such as sensitivity to sub-threshold membrane potential changes, photostability, and compatibility with two-photon excitation.

One approach to engineering GEVIs involves exploiting the native voltage sensitivity of microbial rhodopsins. The opsin Archaeorhodopsin 3 (Arch) was first successfully used to optically record APs in neuronal culture [72]; however, it was found to be too dim at physiologically tolerable imaging powers for *in vivo* applications. Subsequent protein engineering efforts of Arch yielded improvements in brightness as well as sensitivity, kinetics, and reduced photocurrents [73, 74, 44, 75, 42]. An alternative strategy to develop bright rhodopsin-based GEVIs is to create a Förster resonance energy transfer (FRET) pair between a bright fluorescent protein (FP) and the rhodopsin protein [76]. In this strategy, the bright FP is the reporter fluorophore, and the rhodopsin is used as the voltage sensitive domain. This strategy was successfully implemented to develop Ace2N-mNeon, a bright fast GEVI that was able to report single APs *in vivo* [76]. The Ace2N-mNeon member of the rhodopsin family of GEVIs has been used as a scaffold to create GEVIs with other favorable characteristics. Groups at Janelia have previously replaced the FP in Ace2N-mNeon with a HaloTag protein covalently bound to a small-molecule fluorophore (JaneliaFluor or JF [77, 78] to create a chemigenetic sensor called Voltron [79].

Integrating automated patch clamping into discovery experiments for better voltage indicators drastically improved the throughput to enable a Voltron variant discovery (Voltron.A122D) that increased the sensitivity to a single AP by 65% compared to Voltron. This variant (named Voltron2) also exhibited approximately 3-fold higher sensitivity in response to sub-threshold membrane potential changes. Voltron2 retained the sub-millisecond kinetics and photostability of its predecessor, with lower baseline fluorescence. Introducing the same

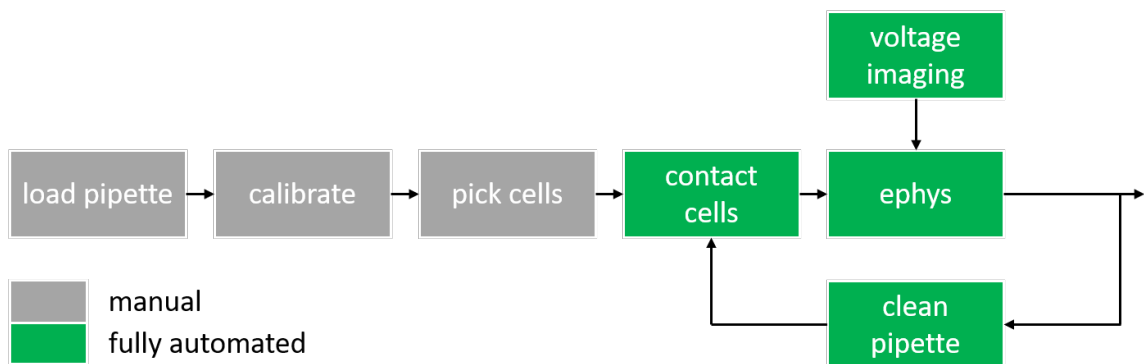


Figure 3.1: patcherBot workflow showcasing the use of voltage imaging screening within the electrophysiology experiment. The difference here versus the original patcherBot is the addition of voltage imaging during ephys recordings.

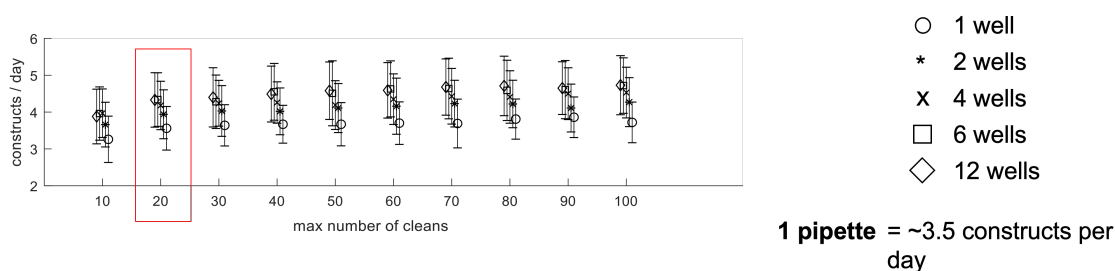


Figure 3.2: Estimated throughput model for the voltage imaging-specific patcherBot based on the maximum number of cleans per pipette. The red box shows with an average maximum number of cleans at 20, we can expect around 3.5 constructs screened per day.

A122D substitution to other Ace2 opsin-based voltage sensors similarly increased their sensitivity. Overall, the inclusion of the patcherBot to screen for better GEVIs have discovered a generalizable mutation that significantly increases the sensitivity of Ace2 rhodopsin-based sensors, improving their voltage reporting capability.

3.3 Methods and Validation of voltage imaging integration with the patcherBot

3.3.1 Current GEVIs

ASAPI

Accurate optical reporting of electrical activity in genetically defined neuronal populations is a long-standing goal in neuroscience. Accelerated Sensor of Action Potentials

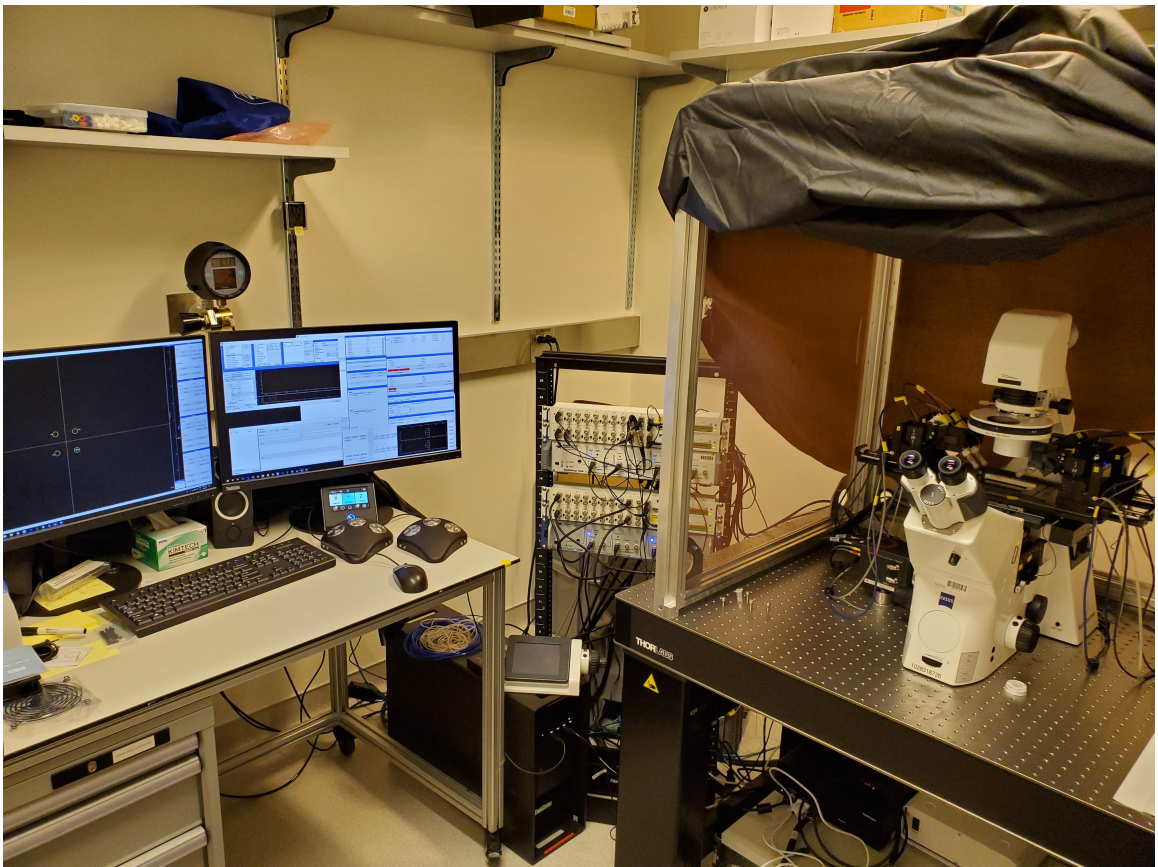


Figure 3.3: The physical setup of the patcherBot @ Janelia in collaboration with Sensapex.

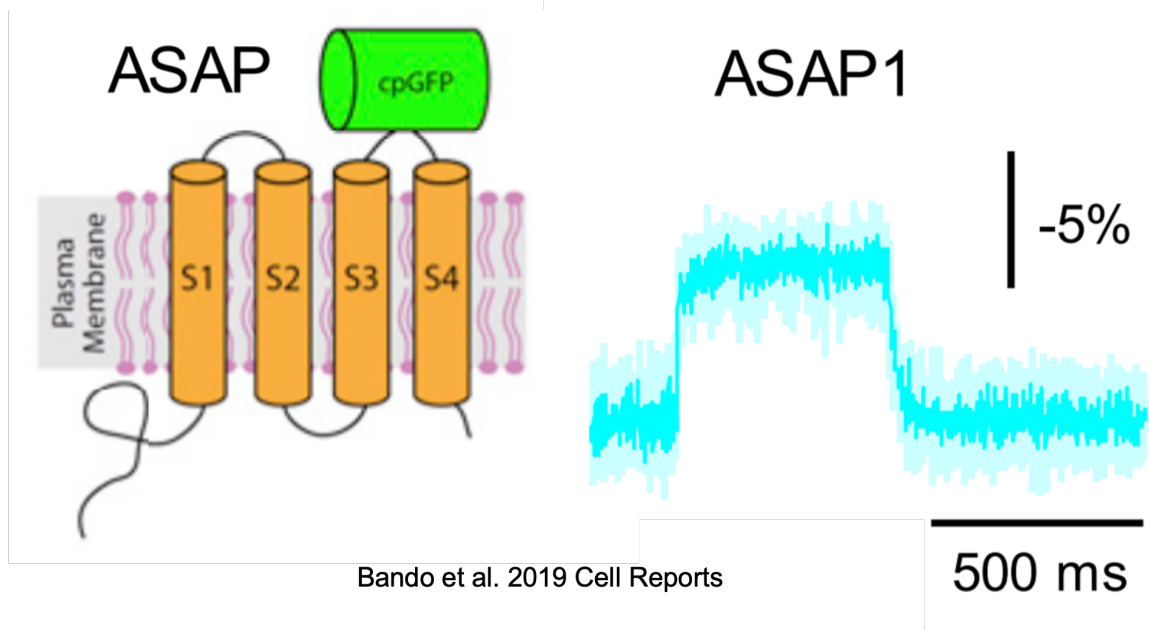


Figure 3.4: From Bando et al., a schematic drawings of the voltage indicator, Accelerated Sensor of Action Potentials (ASAP), and its representative averaged optical traces of ASAP1 during depolarizing steps (from -70 to 30 mV). Five trials were averaged for each neuron [80].

1 (ASAP1), a voltage sensor design in which a circularly permuted green fluorescent protein is inserted in an extracellular loop of a voltage-sensing domain, renders fluorescence responsive to membrane potential Figure 2.4. ASAP1 demonstrates on and off kinetics of ~ 2 ms, reliably detected single action potentials and subthreshold potential changes, and tracked trains of action potential waveforms up to 200 Hz in single trials. With a favorable combination of brightness, dynamic range and speed, ASAP1 enables continuous monitoring of membrane potential in neurons at kilohertz frame rates using standard epifluorescence microscopy. Thus, for optimization and experimental purposes, ASAP1 provides a standardized GEVI capable of validating the performance of the patcherBot@Janelia.

Voltron

Encouraged by the ability of point mutations in the rhodopsin domain to alter function, we performed a large-scale screen of point mutations to find improved versions of Voltron. We discovered that the introduction of an A122D mutation increased the sensitivity of Voltron,

particularly in the sub-threshold range, without compromising kinetics, membrane trafficking or photobleaching. Thus Voltron.A122D was named Voltron2 as a next-generation version of the sensor. Consistent with the observation in culture, in vivo imaging in flies, zebrafish and mice revealed an increased signal-to-noise ratio (SNR) of Voltron2 compared to Voltron.

3.4 Methods

3.4.1 Validation of voltage imaging

In order to validate the operation of the patcherBot for GEVI screening, a series of control experiments were conducted to highlight the efficiency and feasibility. Using ASAP1 as the voltage indicator control, automated whole-cell electrophysiology was conducted in the methods stated below.

3.4.2 Neuronal cell culture

Experiments were conducted in accordance with guidelines for animal research approved by the Janelia Research Campus Institutional Animal Care and Use Committee. Neonatal rat pups (Charles River Laboratory) were euthanized and neocortices (for field stimulation experiments) or hippocampi (for patch-clamp experiments), were isolated. Tissue was dissociated using papain (Worthington) in 10 mM HEPES pH 7.4 in Hanks' Balanced Salt Solution for 30 min at 37 °C. Suspensions were triturated with a Pasteur pipette and passed through a 40- μ m strainer. Cells were transfected by combining 5×10^5 viable cells with 400 ng plasmid DNA and nucleofection solution in a 25- μ L electroporation cuvette (Lonza). Cells were electroporated according to the manufacturer's protocol.

For patch-clamp, 2×10^5 cells were plated onto PDL-coated, 35-mm glass bottom plates (Mattek, #0 cover glass) in 120 μ L of a 1:1 mixture of NbActiv4 and plating medium in the center of the plate. The next day, 2 mL of NbActiv4 medium was added to each plate. Plates were incubated for 7-13 days prior to beginning experiments.

3.4.3 Automated whole-cell electrophysiology

Cultured neurons were patch-clamped at 7-13 DIV at room temperature (23 °C). On the day of the experiment, cell culture medium was first rinsed with imaging buffer consisting of (in mM): 145 NaCl, 2.5 KCl, 10 D-Glucose, 10 HEPES, 2 CaCl₂, 1 MgCl₂ (pH 7.3, adjusted to 310 mOsm with sucrose). The cells were then incubated with 100 nM JF525 dye for 10 minutes (for Voltron mutant screening only), rinsed twice, and kept in imaging buffer. For voltage clamp recordings, 1 μ M TTX was added to the bath to suppress the generation of APs. Micropipettes were pulled on a horizontal puller (P-97, Sutter Instruments) to a tip resistance of 3 to 6 M Ω . For voltage clamp experiments, pipettes were filled with cesium-based internal solution containing (in mM): 115 CsMeSO₄, 15 CsCl, 3.5 Mg-ATP, 5 NaF, 10 EGTA, 10 HEPES, 3 QX-314 (pH 7.3-7.4, 280-290 mOsm). For current clamp experiments, pipettes were filled with 130 KMeSO₄, 10 HEPES, 5 NaCl, 1 MgCl₂, 1 Mg-ATP, 0.4 Na-GTP, 14 Tris-phosphocreatine (pH 7.3-7.4, 280-290 mOsm).

To perform automated patch-clamp screening of the top-performing hits from the field stimulation screen, we used a custom-built Automated uM Workstation, manufactured by Sensapex (Oulu, Finland), based on the PatcherBot [31]. The system is built around an AxioObserver 7 inverted microscope (Zeiss), outfitted with a computer-controlled stage, micromanipulators, and pipette pressure controllers. Pipettes were automatically cleaned between every patch-clamp attempt with Tergazyme and reused, enabling higher throughput than possible with manual patch-clamp [60, 31]. Electrophysiology recordings were performed with a Multiclamp 700B amplifier (Molecular Devices), and digitized with a multifunction data acquisition board (National Instruments PCIe-6259). Neurons were imaged using a 40 \times /1.3 NA oil immersion objective (Zeiss), illuminated with high-power LEDs (Spectra-X light engine, Lumencor) and imaged with a digital sCMOS camera (Hamamatsu Orca Flash 4.0). To image Voltron525, we used a filter cube containing 510/25 nm excitation filter, 545/40 emission filter, 525 nm dichroic (Chroma), with a measured power of 14.7 mW/mm² in the imaging plane. To image Ace2N-mNeon, the filter cube contained

a 470/24 nm excitation filter, 525/40 nm emission filter, 506 nm dichroic with a measured power of 18.1 mW/mm² in the imaging plane. To image VARNAM, the filter cube contained 575/25 nm excitation filter, 610LP emission filter, 594 nm dichroic, with a measured power of 32.8 mW/mm².

The uM Workstation was controlled by the Python platform Acq4 [29], modified to perform fully automated electrophysiology (www.acq4.org). To generate fluorescence/voltage curves, the membrane potential was stepped from +50 to -110 mV in 20 mV increments from a resting potential of -70 mV (0.5 s baseline, 1 s step). For current clamp recordings, a short current pulse was injected (2 nA, 2 ms) to evoke APs.

Stimulus timing, baseline fluorescence calculation, background subtraction, and photobleaching correction was performed the same way as for the field stimulation assay. To identify responsive pixels, a Mann-Whitney U test was performed between the baseline and voltage step segments of the recording. The P value criterion to identify responsive pixels was empirically set to 1e-10.

The onset of each step was fit with the product of a rising and decaying exponential to capture the transient response (if any), summed with a single rising exponential to capture the steady-state response. The decay response was fit with a single exponential. Peak $\Delta F/F_0$ as well as onset and decay kinetics were calculated at each voltage step as was done for field stimulation.

3.5 Results

3.5.1 High throughput optimization of the patcherBot for GEVI screening

With Figure 3.5 and Figure 3.6, we see that the comparison for the $\Delta F/F_0$ curve of ASAP1 clamped at step-wise voltages yields a similar curve for the patcherBot@Janelia compared to manual patching. Furthermore, we were able to leave the robot for unattended recordings past 20 reuses of a single pipette—a goal achieved in order to screen for more constructs per day.

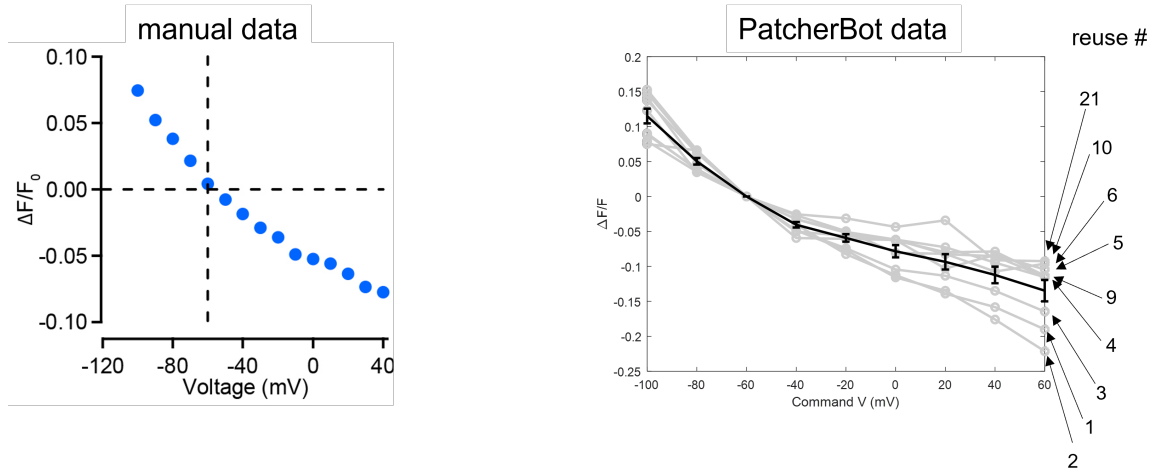


Figure 3.5: ASAP1 $\Delta F/F_0$ comparison between manual patching and the patcherBot. The multiple reuses highlights the ability of pipette cleaning for improved throughput. Error bars are S.E.M.

Further, we see more specifically with an individual cultured neuron that reuse of pipettes does not affect the quality of voltage clamp recordings. As seen in Figure 3.7, different neurons were patched sequentially, and qualitatively, their F/F_0 did not vary between neurons. In Figure 3.8, we have an example of the patcherBot in action with a pipette patched onto a cultured neuron. The active pixels represent the fluorescence change of the neuron when clamped to specific voltages e.g. the fluorescence of the neuron gets brighter as the voltage clamps higher. Figure 3.9 shows a zoomed in representation of the active image capture at 1 kHz. In Figure 3.10A, I show a secondary throughput experiment comparing the voltage clamp and fluorescence response between a manual patch experiment and the patcherBot@Janelia. The manual and robotic voltage clamp representative experiments were conducted with ASAP1 on cultured neurons. Voltage steps were for manual were from -100 mV to 40 mV in 10 mV steps while the patcherBot voltage clamp experiment voltage steps were clamped from -100 mV to 60 mV in 20 mV steps. Figure 3.10C-D show that the pipette was cleaned up to the 8th and 9th reuse of the pipette. Lastly, to validate the robustness of the robot such that it is biologically agnostic, I ran a comparative experiment of the patcherBot@Janelia on HEK cells transfected with ASAP1 to show that

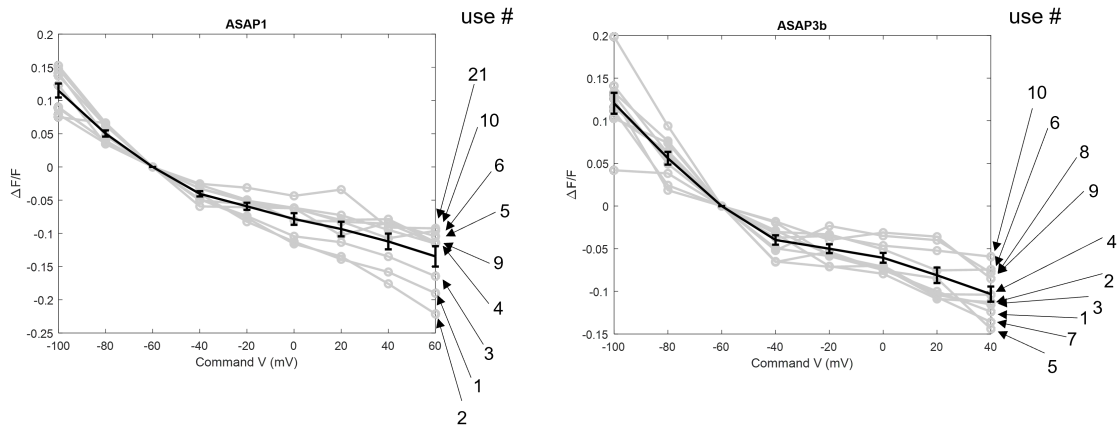


Figure 3.6: Representative examples of $\Delta F/F_0$ curves between the patcherBot collected data of commonly used voltage indicator, ASAP1, and a variant of ASAP3b. Error bars are S.E.M.

the $\Delta F/F_0$ response and voltage clamp responses were similar to literature screening in HEK cells. Overall throughput for this pilot study validating the patcherBot@Janelia are highlighted in Table 3.1.

Table 3.1: Throughput use case of the patcherBot – over multiple experiment sets (whole-cells/attempts)

ASAP1, cultured neurons	Yield	Throughput (~6 hours)
Whole-cells	51 / 66 = 77.3%	8.5 WC/hr
Whole-cells and viable voltage imaging	30 / 66 = 45.5%	5 WC/hr

3.5.2 High throughput screening of Voltron mutants in neuron culture

Voltron variants were generated using site saturation mutagenesis (SSM) performed at 40 positions within the rhodopsin domain. All screening was performed on Voltron mutants labeled with JF525 (Voltron525). Positions were chosen based on: (1) previous reports of analogous positions in other opsins that affected their thermal stability [75], (2) amino acids in close proximity to the retinal chromophore that we reasoned might affect the environment of the Schiff base, or (3) positions that were found to be important in mutagenesis of Archaerhodopsin into a voltage sensor [44] (Figure 3.12A). We performed two rounds of screening (Figure 3.12B).

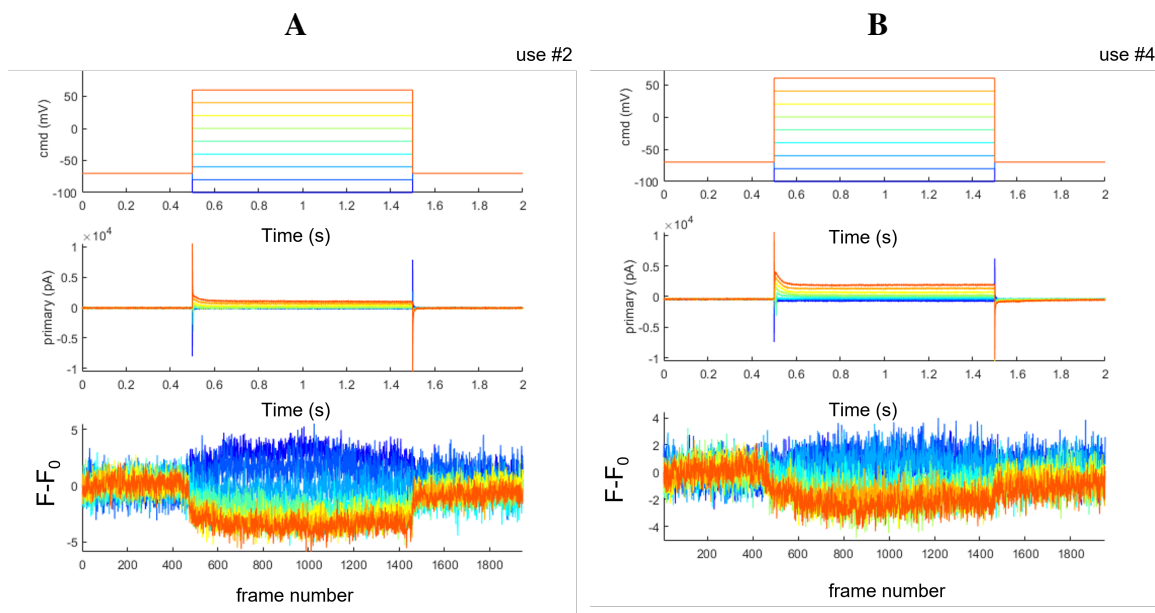


Figure 3.7: a. Representative voltage clamp and $\Delta F/F_0$ data for the patcherBot on the pipette's second reuse for a voltage imaging experiment of ASAP1. b. Representative voltage clamp and $\Delta F/F_0$ data for the patcherBot on the pipette's fourth reuse for a voltage imaging experiment of ASAP1. Frame number was recorded at 1kHz sampling frequency.

The first-round SSM screen revealed many mutations that moderately increased $\Delta F/F_0$. We therefore embarked on a second round of combinatorial (combo) screening, hoping that combining 13 of the top performing mutations (Y63L, N69E, V74E/W, R78H, N81S, L89A/C/G/T, A122D/H, V196P) would further improve the sensor. Of the 1,232 constructs screened in 106 plates, 77% passed QC. Surprisingly, only 28 of 848 combo mutants (3.3%) had significantly improved $|\Delta F/F_0|$ max over Voltron2525 ($P < 0.01$, Mann-Whitney U test;). Similarly, only a few variants had increased SNR (20 of 848, 2.4%). The A122D substitution was present in 34% of the combo variants passing QC; nevertheless, the combo screen revealed that combining it with other mutations resulted in less sensitive variants. Subsequent automated patch-clamp analysis confirmed that Voltron2525, containing the sole A122D substitution, outperformed all combo mutants.

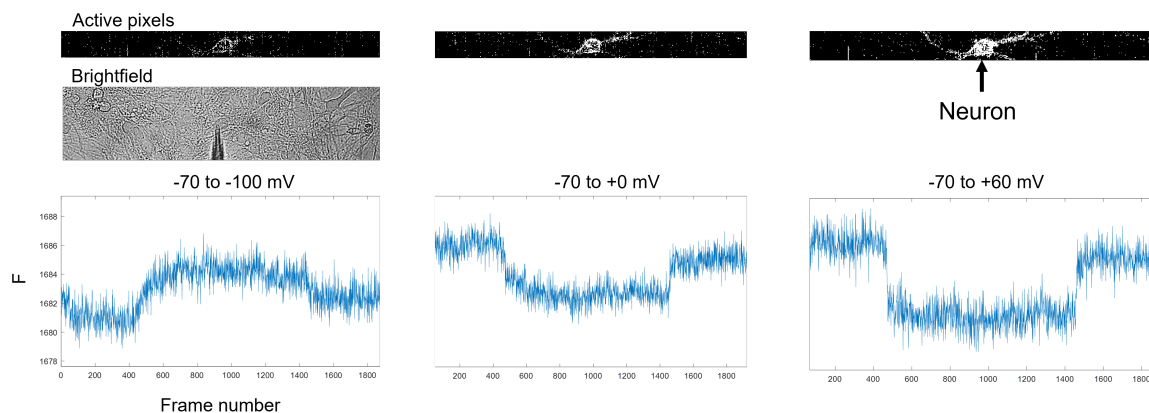


Figure 3.8: Example of the patcherBot with voltage imaging experiment for ASAP1 voltage indicator. The active pixels represent the imaging field of view at 1 kHz along with a brightfield image of the pipette patched onto the cell. The cell was voltage clamped from -100 mV to 60 mV and back to a resting membrane potential of -70 mV in 20 mV steps. Frame number was recorded at 1kHz sampling frequency.

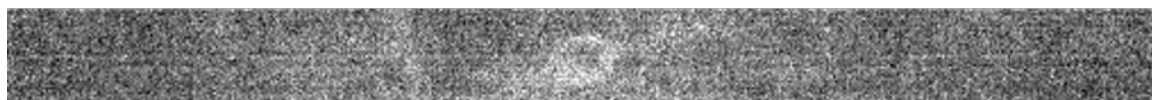


Figure 3.9: Example of the patcherBot with voltage imaging experiment for ASAP1 voltage indicator. The cultured neuron shows fluorescent change when voltage clamped from -100 mV to 60 mV and back to a resting membrane potential of -70 mV in 20 mV steps.

3.5.3 Screening and characterization with automated whole-cell electrophysiology

Many single and combo mutation hits from the neuron culture screen had improved $|\Delta F/F_0|_{\max}$ over Voltron but had very similar $\Delta F/F_0$ characteristics among them. We deemed the field stimulation screen to be insufficiently sensitive to find the one variant with the best performance, so we used the uM Workstation, a fully automated whole-cell electrophysiology platform based on the patcherBot to perform a secondary screen on top single and combinatorial mutant hits.

We first validated the throughput and performance of the automated electrophysiology platform. To mimic a small-scale screen, 10 35-mm Mattek dishes of cultured neurons were transfected with variants of the voltage sensor ASAP [81]. The uM Workstation made

103 patch-clamp attempts in 7.1 hours, with a 78% whole-cell success rate. The system operated unattended for 5 hours during that day of screening. Thus, the uM Workstation allowed us to screen 10 constructs per day, assuming 5-10 neurons per construct.

The uM Workstation achieves high throughput by automatically cleaning and reusing patch-clamp pipettes (Figure 3.13A); however, it is conceivable that the cleaning process is imperfect and whole-cell success rate degrades over subsequent attempts. To address this, we evaluated pipette performance after multiple patch-clamp attempts. Whole-cell success rate decreased over time, but likely due to cell health degradation, not due to an accumulation of debris on the reused pipette, since replacing the pipette did not recover the success rate. In a separate experiment we replaced the dish without replacing the pipette, and found that the success rate recovered, further suggesting that cell health degradation, not pipette debris is responsible for the apparent decrease in success rate. To explore the limits of pipette cleaning, we patch-clamped cells with the same pipette, replacing the plate as needed, until the time to form a gigaohm seal increased, indicating a contaminated pipette. Consistent with previous observations, a single pipette could be used for patch-clamping 50 neurons [31]. Last, we evaluated the quality of the recordings and found 85.6% (143 out of 167) of the successful whole-cell recordings had a holding current greater than -100 pA and Access Resistance (R_A) less than $30 M\Omega$, which meets the criteria for most of the published data acquired with manual patch clamp. Together, we found that the automated uM Workstation successfully increased our throughput, enabling large-scale patch-clamp studies, without compromising data quality.

Using the uM Workstation we then screened top-performing single-position mutants from the field stimulation screen (the SSM screen described above), including Voltron as a control. While Voltron525.V74G and Voltron525.V74W were the top performers from the field stimulation screen, their fluorescence response to a 100 mV voltage step was lower than that of Voltron2525 (Figure 3.13B). The other mutants were also 8% to 55% less sensitive to 100 mV voltage steps than Voltron2. Meanwhile, Voltron2525 was found to be

65% more sensitive than Voltron, consistent with the field stimulation screen. Furthermore, in the physiologically relevant sub-threshold voltage range (-90 to -50 mV), Voltron2525 exhibited a significantly steeper slope than Voltron525 (0.54 ± 0.01 and 0.21 ± 0.01 %/mV, respectively; $P = 0.0009$, Mann-Whitney U test), making it a higher-fidelity optical reporter of changes in sub-threshold membrane potential.

Surprisingly, the combo mutation screen (second round of the field stimulation assay, Figure 3.12B) yielded few variants with improved sensitivities. We nevertheless screened the 34 variants with sensitivities marginally better than Voltron2525 using the uM Workstation. As was the case with the single-position mutants, we found no combo mutants that out-performed Voltron2525 (Figure 3.13C). Therefore, for the remainder of this study, we focused on characterization of Voltron2525.

Voltron2525 exhibited fast onset and decay kinetics that were best fit with a double exponential (Figure 3.12D). Interestingly, the A122D mutation completely eliminated the transient peak in the fluorescence response of Voltron525 (Figure 3.13B inset). The fast component of the onset and decay kinetics was slightly shorter for Voltron2525 (onset: 0.67 ± 0.03 ms, decay: 0.89 ± 0.09 ms) compared to Voltron525 (onset: 0.85 ± 0.06 ms, decay: 1.13 ± 0.08 ms), though not significantly different. The slow components were likewise similar between the two sensors (Voltron525: onset 3.26 ± 0.47 ms, decay 6.27 ± 1.41 ms; Voltron2525: onset 4.76 ± 0.92 ms, decay 4.74 ± 0.32 ms). The fast component of Voltron2525 accounted for a larger percentage of the overall response in the onset but not decay response (Figure 3.13E). Overall, the kinetic properties of Voltron525 and Voltron2525 were found to be qualitatively similar.

Consistent with the improved sensitivity of Voltron2525 in response to voltage steps, it was also superior in its sensitivity to APs. Voltron2525 reported single APs with $\Delta F/F_0$ of 10.09 ± 1.47 %, significantly higher than for Voltron525 (6.16 ± 0.74 %, Figure 3.13F,G). The baseline fluorescence of Voltron2525 was 30% lower than Voltron525, which may be beneficial in some experiments but detrimental in others (Figure 3.13H). Nevertheless,

both Voltron2525 and Voltron2525-ST showed good membrane localization, qualitatively similar to their Voltron counterparts [79]. In culture, Voltron2525 photobleached slightly, but not significantly, slower than Voltron525 (Voltron525: $45\pm 2\%$, Voltron2525: $41\pm 1\%$ reduction in fluorescence; $P=0.11$, Mann-Whitney U test; Figure 3.13I).

We believe that the A122D mutation responsible for increased sensitivity of Voltron2525 could have beneficial properties when grafted onto other Ace rhodopsin-based GEVIs. We tested this hypothesis in Ace2N-mNeon and VARNAM. As expected, adding the A122D mutation to both GEVIs increased their sensitivity to depolarizing and hyperpolarizing voltage pulses (Supplementary Fig. 9). Similar to Voltron2525, A122D significantly increased the slope of the sensors in the sub-threshold range (Ace2N-mNeon: $0.091\pm 0.012\%$ /mV, Ace2N-mNeon.A122D: $0.303\pm 0.012\%$ /mV, $P=0.006$; VARNAM: $0.104\pm 0.012\%$ /mV, VARNAM.A122D: $0.147\pm 0.010\%$ /mV, $P=0.045$; Mann-Whitney U test). The mutation eliminated the transient peak from VARNAM but not from Ace2N-mNeon.

Various high-throughput platforms have been developed that have been used to screen for improved GEVIs [73, 82, 42]. The majority of these platforms utilize bacteria or tissue culture cells for screening. We instead opted to perform our high-content primary screen in dissociated neurons, a costlier and more time-consuming strategy, but one that maximized the compatibility of the resulting sensor with in vivo neuronal imaging. Even still, our field stimulation screen was insufficiently sensitive to disambiguate the top-performing sensors. We therefore relied on the automated patch-clamp system that afforded us the ability to screen dozens of sensors faster than possible manually, without compromising data quality. The system had a lower throughput than the field stimulation screen but enabled us to characterize the sensitivity and kinetics of many variants with much higher fidelity. The combination of both field stimulation and patch-clamp screens provided a high-quality assessment of top-performing variants.

Increasing the sensitivity of GEVIs (the difference in photon flux per millivolt change in membrane potential) and reducing photobleaching still remain the main challenges to

increase the adoption of GEVIs for in vivo experimentation. Protein engineering efforts devoted to creating two-photon-compatible GEVIs will also be required to address the emerging trend in the field to image deep in the brain while maintaining single-cell resolution. Chemigenetic indicators like Voltron2 continue to be promising scaffolds to address these goals.

3.6 Opsin Screening and PatcherBot Integration

In addition to screening for genetically encoded voltage indicators, the patcherBot was applied to an optogenetics screen to showcase a secondary application of the patcherBot enabling screening for genetically encoded effectors (light stimulation in the electrophysiology recording) in Figure 3.14 [42]. Here, the setup for the patcherBot screening rig is reverted to the original upright microscope.

3.6.1 Opsin autopatching significance

Patch clamp recording is the gold standard method for resolving millivolt- and millisecond-scale dynamics and ion conductances of light activated channels. Although laborious, screens that incorporate patch clamp electrophysiology have produced rich data sets to drive further opsin discovery Figure 3.15A. For example, in 2014, the Boyden Lab used 1000 manually patched cells to screen approximately 120 opsin variants from different algal species, identifying opsins that had high photocurrents (CoChR), red-shifted activation spectra (Chrimson), and improved kinetics (Chronos)[41, 43, 42].

3.6.2 Implementation towards directed evolution platform capable of high-throughput screening of optogenetic tools

With the patcherBot capable of using a single pipette to patch 12-15 cells per hour in a closed-loop process that can run unattended for 3 or more hours, I can perform directed evolution along dimensions difficult to optimize for using imaging, specifically kinetics and

potassium selectivity/conductance. Figure 3.15B shows a representative example of HEK cells transfected with channelrhodopsin-2 under the microscope of the patcherBot. In one preliminary experiment, the patcherBot was used to record photoactivated currents from HEK cells transfected with Channel-rhodopsin 2 (ChR2) at a rate of 9 whole cell recordings per hour and a whole cell yield of 92% (46 whole cells, 50 attempts, total time = 5 hrs 13 minutes) (Figure 3.16). Building on this discovery, one can imagine a systematically-optimized multi-pipette version of the patcherBot that can record light activated currents at a conservative rate of 200 cells per day that will be integrated with existing image-based multidimensional screening robot. This approach represents a dramatic expansion of the toolbox for multidimensional directed evolution and has the potential to discover tools that will address both new and longstanding needs in the field of optogenetics.

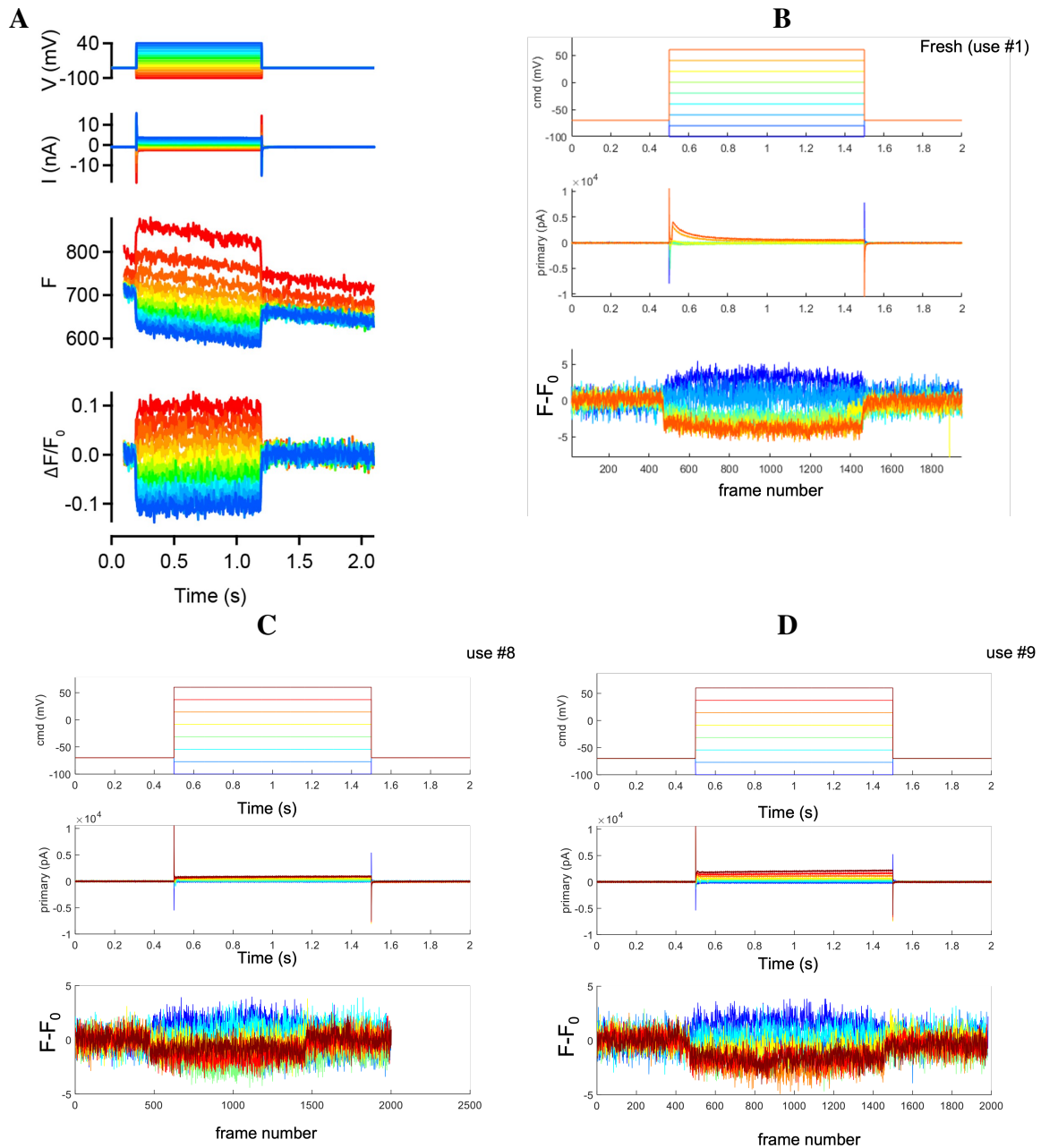


Figure 3.10: a. Manual voltage clamp representative experiment of the voltage indicator, ASAP1, on cultured neurons. Voltage steps were from -100 mV to 40 mV in 10 mV steps. b. patcherBot voltage clamp experiment of the voltage indicator, ASAP1, on cultured neurons. Voltage steps were clamped from -100 mV to 60 mV in 20 mV steps. This panel represents the 8th reuse of the pipette. c. patcherBot voltage clamp experiment of the voltage indicator, ASAP1, on cultured neurons. Voltage steps were clamped from -100 mV to 60 mV in 20 mV steps. This panel represents the 8th reuse of the pipette. d. patcherBot voltage clamp experiment of the voltage indicator, ASAP1, on cultured neurons. Voltage steps were clamped from -100 mV to 60 mV in 20 mV steps. This panel represents the 9th reuse of the pipette. Frame number was recorded at 1kHz sampling frequency.

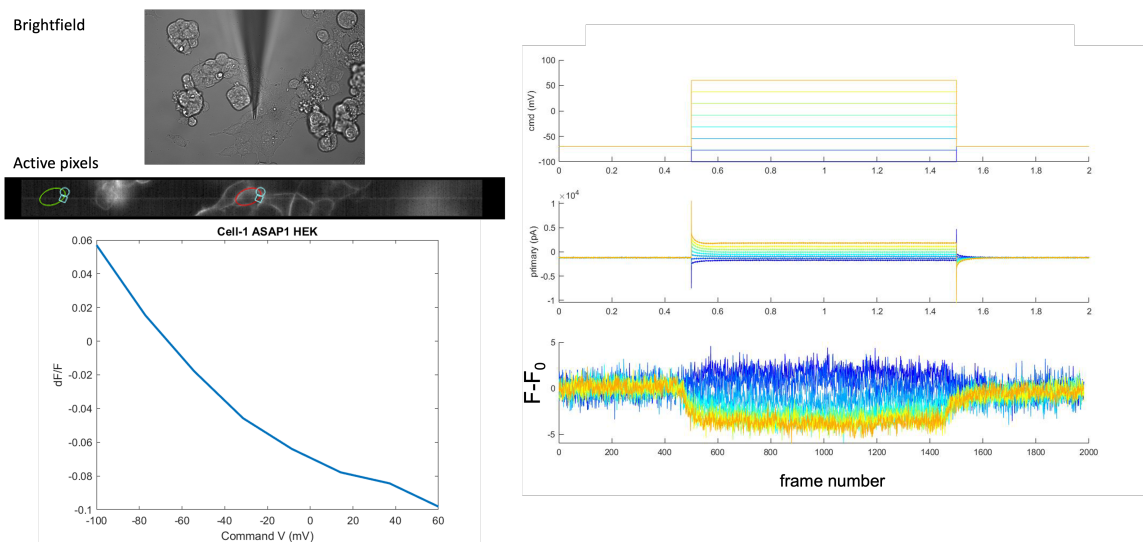


Figure 3.11: patcherBot voltage clamp experiment of the voltage indicator, ASAP1, on cultured HEK cells. Representative brightfield and active pixel FOV image. In the active pixels image, the red circle represents the current patched cell, and the green circle represents a future cell of interest to patch. Voltage steps were clamped from -100 mV to 60 mV in 20 mV steps. Frame number was recorded at 1kHz sampling frequency. Representative standard $\Delta F/F_0$ curve collected for ASAP1 HEK cells.

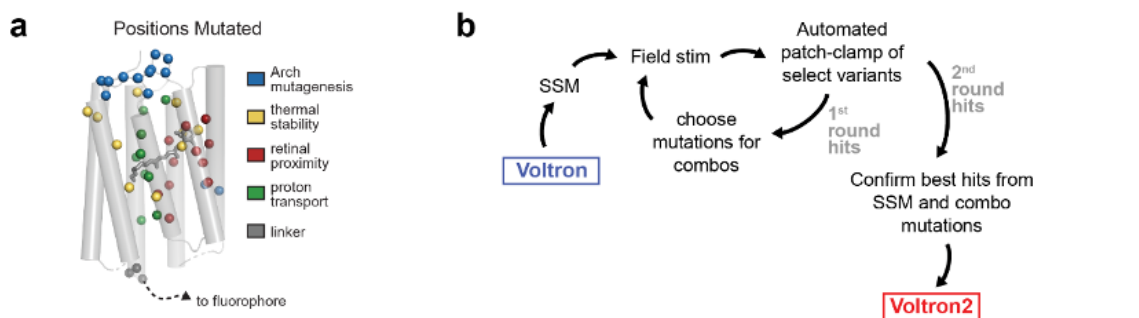


Figure 3.12: Mutagenesis and screening of Voltron in cultured neurons. a. Residues targeted for SSM in the Ace2N rhodopsin domain of Voltron, colored by the rationale for targeting them. b. Mutagenesis and screening workflow.

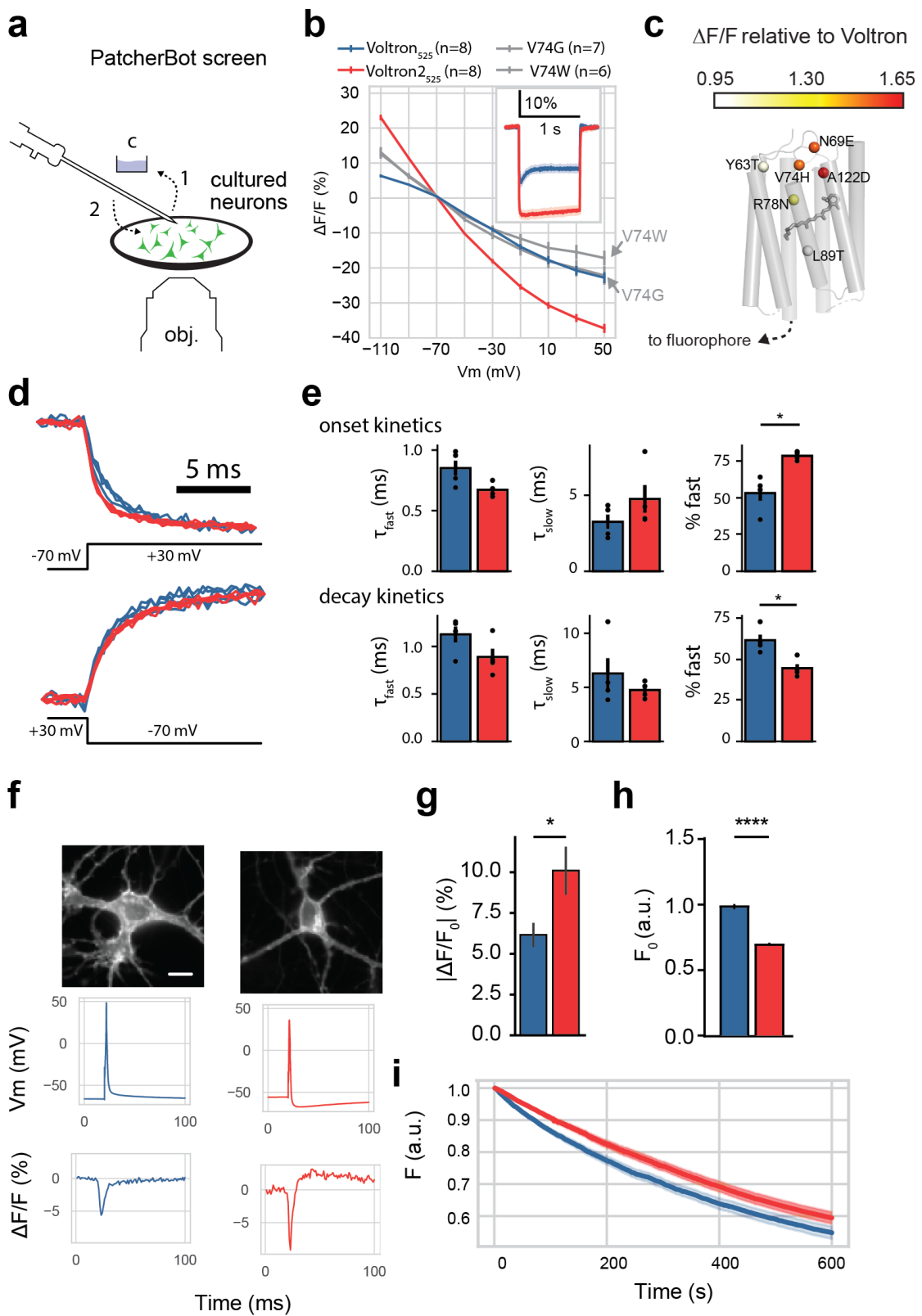


Figure 3.13: Automated patch clamp screening and characterization of Voltron2 in cultured neurons. a. Fully automated uM workstation screening platform, based on PatcherBot. The pipette cleaning procedure is shown where a used pipette is dipped into a reservoir of cleaning solution (step 1, “c”) and back to the neuronal culture for a subsequent patch-clamp attempt without the need for replacing the pipette (step 2). b. Peak fluorescence responses to voltage steps (-70 to +30 mV) of Voltron525, Voltron2525 and the top two variants from the field stimulation assay (mean \pm s.e.m.; Voltron2525 vs. Voltron525: $p=0.012$; Voltron2525 vs. Voltron525.V74G: $p=0.015$; Voltron2525 vs. Voltron525.V74W: $p=0.0003$, one-way ANOVA followed by Dunnett’s post-hoc test). Inset: Voltron525 and Voltron2525 fluorescence traces (solid line: mean, shading: s.e.m.) in response to -70 to +30 mV voltage steps. N values (neurons) indicated in figure. c. Mutated residues from 1st screening round (single sites) colored by the maximum $\Delta F/F_0$ response to 100 mV (-70 to +30 mV) voltage steps, measured with the uM workstation. Top mutations at each position are labeled. d. Onset (top) and decay (bottom) fluorescence kinetics of Voltron525 and Voltron2525 in response to a +100 mV voltage step from -70 mV. Vertical axis scaled to match $\Delta F/F_0$ between the sensors. e. Onset and decay kinetics (mean \pm s.e.m.) of the traces in (d). Onset kinetics: $*p=0.03$, Mann-Whitney U test. Decay kinetics: $*p=0.03$, Mann-Whitney U test; Voltron525: $n=4$, Voltron2525: $n=4$. f. Representative fluorescence responses to single evoked APs in current clamp. Scale bar: 10 μm . g. $\Delta F/F_0$ in response to single AP stimulation in current clamp mode (mean \pm s.e.m.; $*p=0.03$, Student’s t test, Voltron525: $n=5$, Voltron2525: $n=7$). h. Normalized resting fluorescence relative to mTagBFP2 fused to the C terminus (mean \pm s.e.m.; $****p < 0.0001$; Voltron525: $n=105$ cells, Voltron2525: $n=115$ cells, Student’s t test). i. Photobleaching comparison of Voltron525 and Voltron2525 over 10 mins (solid line: mean; shading: s.e.m.). All experiments were performed at room temperature.

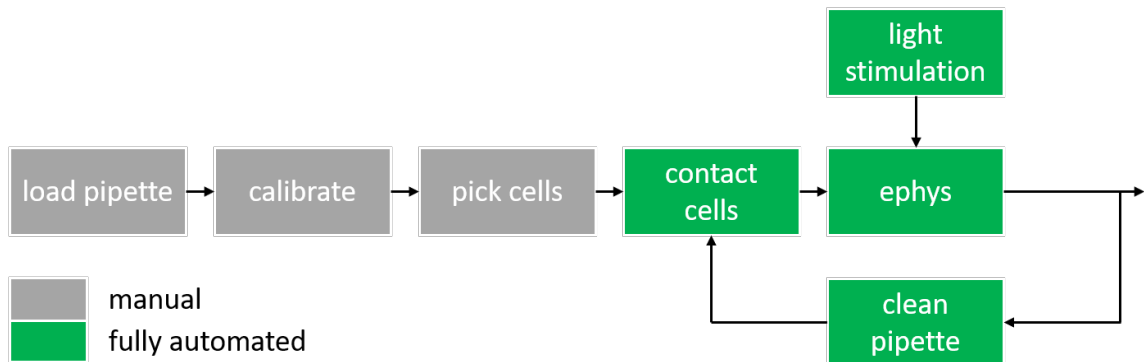


Figure 3.14: patcherBot workflow showcasing the use of opsin screening within the electrophysiology experiment. The difference between the original patcherBot is the addition of light stimulation during the ephys recording.

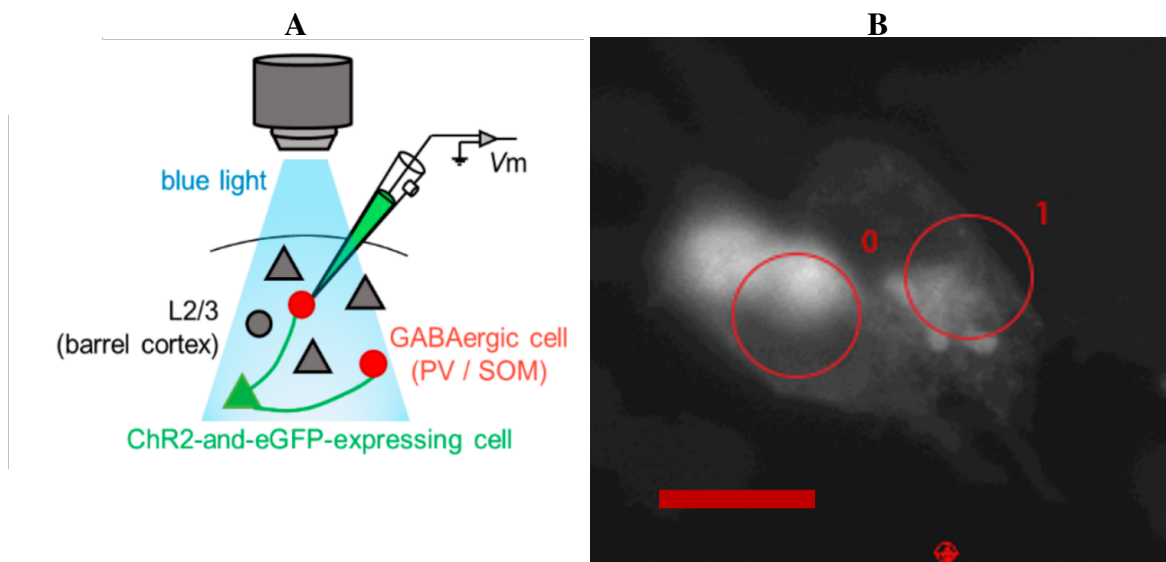


Figure 3.15: a. From Noguchi et al., an example of Channelrhodopsin 2 and eGFP are artificially expressed in specific excitatory cells (green, triangle) in layer 2/3 of the barrel cortex [83]. Whole-cell recordings are made from fluorescent-targeted cells (red, circle), and light-induced membrane potential fluctuations of these GABAergic neurons are recorded. b. HEK cells expressing ChR2 on the PatchBot. Scale bar: 10 μm

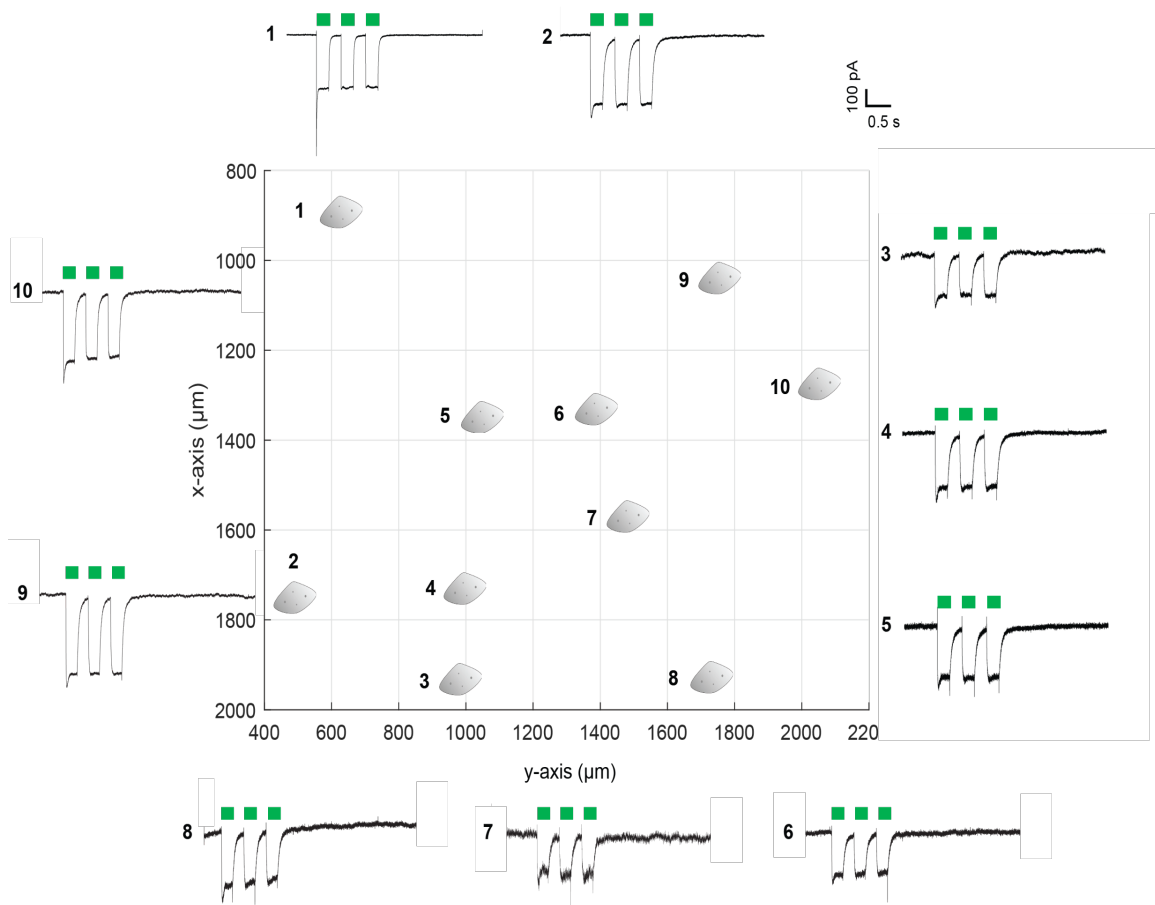


Figure 3.16: In one preliminary experiment, the patcherBot was used to record photoactivated currents from HEK cells transfected with ChR2 at a rate of 9 whole cell recordings per hour and a whole cell yield of 92% (46 whole cells, 50 attempts, total time = 5 hrs 13 minutes). Representative experiment summary of 10 cells show the position and voltage clamp recordings. Current traces are in response to 3 LED (470 nm) pulses of 500 ms.

CHAPTER 4

DEEP LEARNING-BASED REAL-TIME DETECTION OF NEURONS IN BRAIN SLICES FOR *IN VITRO* PHYSIOLOGY

4.1 Introduction

Whole-cell patch clamp electrophysiology, a gold standard technique in neuroscience, is a high-fidelity method used to monitor the biophysical mechanisms of neural activity at the single neuron level. Whole-cell patch clamp experiments allow the user to report current and voltage fluctuations at a spatiotemporal resolution beyond the capability of other techniques [2]. However, the technique is considered highly laborious and low throughput since it involves utilizing a glass micropipette to probe a cell individually—the trade-off for exceptional signal quality—preventing its widespread use for high-throughput screening. Typically, *in vitro* patch clamp experiments are done manually in which the user views an acute brain slice under a microscope, visually selects a neuron to patch, moves the pipette close to the cell, creates a high resistance (“giga-ohm”) seal between the pipette and cell, and breaks into the membrane to create a whole-cell configuration. These experiments allow scientists to monitor complex biophysical phenomena such as voltage and current fluctuations of single neurons.

One of the most crucial initial steps in the patch clamping process is identifying a healthy cell. The edges of a healthy neuron under differential interference contrast DIC are often unclear and vary widely in shape and size. Moreover, the milieu of brain tissue not only consists of neurons, but also cerebrospinal fluid, blood vessels, and glia, among other extracellular content which induce significant light scattering under DIC, an optical technique widely used for observing unstained biological samples. While fluorescence microscopy may be used for identifying somas in acute slice patch clamp experiments, it is

not always practical since it requires the use of dyes or genetically engineered production of fluorophores [84]. Rather, it is often desirable to image label-free, yet optically transparent samples which require the use of DIC.

Previous work has demonstrated success in automating cell detection in cultured cells [85, 86], via methods such as image segmentation and image enhancement techniques. Vicar et al. tested a handful of tools designed to detect cultured cells and compared them using the F1 score, a metric commonly used to measure object identification accuracy. The average F1 score reported for the methods which used DIC and additional preprocessing was 0.76. The average F1 score for the same methods on raw images was 0.50, indicating preprocessing may improve performance of object detection methods.

However, common image enhancement techniques, in concert with edge detection algorithms, are not robust enough for application in acute slice because the nature of the images under DIC yields more scattering than cultured cells. In addition, there are several cell segmentation and tracking methods that are not directly applicable to cell detection under DIC in tissue [87]. To overcome this obstacle, this work adapts a deep neural network to identify neurons in acute slice—particularly pyramidal neurons in the layer 5 cortex of the mouse brain. While there has been a myriad of convolutional neural networks (CNNs) used for identifying cells, most applications are used on images post-experiment either for cell detection on slides, cell cultures, or for cell segmentation of 3-D connectomics [88, 89, 90, 91, 92].

Since this is such a critical task, often requiring significant experience to identify healthy cells, automation of the cell identification and selection process is a difficult, necessary step towards completing full automation of patch clamp as well as in assisting novices how to identify cells. Research groups enabling the automation of patch clamp have alluded to the potential benefits of automating this task, though the problem is not yet fully resolved [31, 38, 93]. Koos et al. have recently shown a CNN that identifies somas under DIC, though their network required substantial time and over 31,000 annotated neurons for training

[45]. In this study, we aimed to achieve similar accuracy on a smaller, faster CNN that can quickly nominate cells for patch clamp experiments. Our deep learning-based method, quantified by F1 scores and mean average precision (mAP), is comparable to published work on cultured cell identification and other deep learning based solutions for cell detection. Thus, we show that transfer learning using the YOLOv3-CNN architecture can require minimal training resources and enable fast, accurate neuronal detection for images gathered on live, acute brain slices.

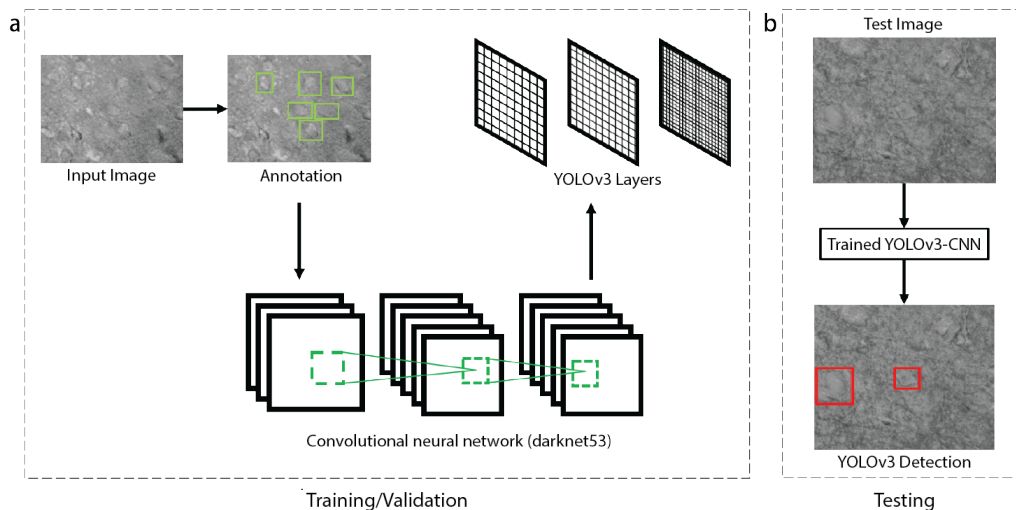


Figure 4.1: After initial (a) training and validation using annotated input images, testing (b) shows a successful detection of neurons in unannotated, unaltered images.

4.2 Methods

For the purposes of automated neuronal detection in acute brain slices, we utilize the default architecture of the YOLOv3 neural network, most notable for its speed and accuracy of detection [94, 95]. In order to increase speed in object detection, YOLO reframes object detection as a single regression problem, mapping straight from image pixels to bounding box coordinates and class probabilities. In addition, YOLO looks globally on the entire image when making predictions. The primary motivation for selecting an architecture optimized for speed and accuracy is to apply the network to a video or real-time imaging.

Thus, our methods include using transfer learning with the YOLOv3 architecture to provide a default model to fine-tune. A representative workflow is represented in Figure 4.1.

4.2.1 Implementation

Acquisition of Acute Brain Slice Images

All acute brain slice samples and images were captured utilizing the hardware and software configuration according to Kolb et al [96]. The system was based on a conventional electrophysiology setup (SliceScope Pro 3000, Scientifica Ltd), and the samples were imaged using a 40x objective (LUMPFLFL40XW/IR, NA 0.8, Olympus) on a motorized focus drive, illuminated under DIC with an infrared light-emitting diode (Scientifica), and captured with a Rolera Bolt camera (QImaging). All animal procedures were in accordance with the US National Institutes of Health Guide for the Care and Use of Laboratory Animals and were approved by the Institutional Animal Care and Use Committee at the Georgia Institute of Technology.

Annotation Procedure

Annotations were made manually using LabelImg, an open source graphical image annotation tool written in Python [97]. Annotations were saved as XML files in PASCAL VOC format, the format as used by ImageNet [98]. Healthy neurons were annotated and labeled by drawing a bounding box around them. The rectangular boxes varied in size and were allowed to intersect with each other.

The training, validation, and test data sets consisted of 1280x1024, 8-bit raw images of acute slices under DIC. Within the training and validation data sets, 369 original, raw images were used with a total of 1138 annotated neurons. For the trained CNN test data set, a smaller set of 37 images was used containing 107 annotated neurons. Since we are using transfer learning on a pre-trained model, a smaller data set for training and validation is appropriate to obtain sufficient accuracy. All data sets will be made publicly available at

autopatcher.org.

Convolutional Neural Network: YOLOv3

As mentioned previously, healthy cells from raw images of acute slice under DIC are difficult even for humans to identify. As an immediate effort to improve our ability to detect cells, using Python, we applied traditional image enhancement techniques to increase contrast and sharpen edges to the human eye. However, the advantages of preprocessing training data in machine learning have not been confirmed, motivating this work to also compare two training models to reveal whether or not image enhancement (using custom Python scripts and the OpenCV library) improved the performance of the neural network. Histogram equalization, an image processing technique commonly used for improving contrast, both enhances contrast and preserves detail in the images. We compared a network trained on raw, unaltered images to a network trained on histogram equalized images. Histogram equalization was the only image enhancement technique used to create training and validation data sets, so hereafter we will refer to those data sets as "enhanced" for conciseness. Data sets without image enhancement will be referred to as "unaltered."

For both the unaltered image and the enhanced image data sets, they were randomly divided into a training and validation set at a 10:1 ratio. The input image resolution was set to 416x416 pixels. While downsampling the images to 416x416 introduces some unintended artifacts of reduced resolution, there is a desired trade-off between computational time and accuracy. Secondly, the dimensions of the input image are resized while maintaining the image aspect ratio. For example, the longer dimension, 1280, is scaled to 416 and the secondary dimension, 1024, is scaled to 332.8 pixels. The remaining pixel area is black pixels. The YOLOv3 network architecture consists of a backbone network called Darknet-53, an up-sampling network, and the detection layers called YOLO layers [94, 95].

As stated previously, transfer learning fine-tunes a pre-trained neural network model. Since the model does not need to be trained from scratch, transfer learning is often a suitable

choice when training with limited training and validation data sets. Moreover, transfer learning has the potential to improve network performance and training time [99]. The initial model of our CNN was pre-trained on the Imagenet data set [95]. The final 3 layers were initially trained with our custom acute brain slice data set for 10 epochs before all layers were unfrozen and the entire network was trained on the data set for 40 more epochs for a total of 50 epochs. If loss reached a steady state value, the training would stop early.

In addition, YOLOv3 object detection utilizes non-max suppression (NMS) which was also utilized here to classify the determined predictions. The intersection over union for NMS was set to 0.45 as based on machine learning standards.

Training computations were conducted on a desktop PC with a 3.7 GHz Intel Core i7-8700K, 32GB RAM memory and an NVIDIA GeForce GTX 1080. For trained model evaluations, the software was run on a notebook PC with a 2.8 GHz Intel Core i7-7700HQ and 16GB RAM memory.

4.2.2 Evaluation metrics of YOLOv3 performance

Generally, trained networks can be assessed quantitatively through the metrics of precision (P) and recall (R),

where T_p is the number of true positive classifications, F_n is the number of false negatives, and F_p is the number of false positives. Precision represents how likely a prediction will be accurate. On the other hand, recall represents how accurate the model is based on correct classifications and classifications it failed to identify. Therefore, for an ideal model, it is desired to have both precision and recall equal to 1, or 100%.

In this study, PASCAL VOC-style Average Precision (AP) at a single intersection over union (IOU) threshold of 0.45 was calculated to evaluate the models trained by the loss function of YOLOv3 [100]. Although the general definition of AP is the area under the precision-recall curve,

$$AP = \int_0^1 P(R)dR, \quad (4.1)$$

the interpolated precision-recall, "P(R)", curve is piece-wise constant. Therefore, with the number of recall values, we define AP as described in Cartucho et al. [101]

Since AP is the integration of precision with respect to recall, and the ideal precision and recall values are both 1, the ideal AP is also 1, or 100%. Mean average precision (mAP) is especially helpful for multi-class studies, since it is the average AP of each class the network can identify. While there is only one class ('neuron') in this study, we will use the common notation of mAP hereafter.

Another common metric used for quantifying the performance of neural networks is the F1 score, [92]:

$$F1 = 2 \frac{PR}{P + R}, \quad (4.2)$$

which is particularly useful when determining the optimal balance between precision and recall. Since the ideal network would yield precision and recall equal to 1, the F1 score would then also be 1.

The last metric used describes the accuracy of the model using true positives (TP), false positives (FP), and the ground truth (GT) annotations where,

$$\text{Accuracy} = \frac{TP}{GT + FP} \quad (4.3)$$

such that the ideal model would be 100% accurate should all its guesses match the ground truth annotations without false positives.

4.2.3 Real-time detection and patch clamp validation

Brain slice preparation

All animal procedures were in accordance with the US National Institutes of Health Guide for the Care and Use of Laboratory Animals and were approved by the Institutional Animal Care and Use Committee at the Georgia Institute of Technology. For the brain slice experiments, male mice (C57BL/6, P31–P46, Charles River) were anesthetized with isoflurane,

and the brain was quickly removed. Coronal sections (300 μm thick) were then sliced on a vibratome (Leica Biosystems VT1200S) while the brain was submerged in ice-cold sucrose solution containing (in mM) 40 NaCl, 4 KCl, 1.25 $\text{NaH}_2\text{PO}_4\cdot\text{H}_2\text{O}$, 7 MgCl_2 , 25 NaHCO_3 , 10 D-Glucose, 0.5 $\text{CaCl}_2\cdot 2\text{H}_2\text{O}$, 150 Sucrose (pH 7.3–7.4, 300–310 mOsm). The slices were incubated at 37 °C for 1 h in Artificial Cerebro-Spinal Fluid (aCSF) consisting of (in mM) 124 NaCl, 2.5 KCl, 1.25 $\text{NaH}_2\text{PO}_4\cdot\text{H}_2\text{O}$, 1.3 MgCl_2 , 26 NaHCO_3 , 10 D-Glucose, 2 $\text{CaCl}_2\cdot 2\text{H}_2\text{O}$, 1 L-Ascorbate $\cdot\text{H}_2\text{O}$ (pH 7.3–7.4, 290–300 mOsm). Prior to recording, the slices were maintained at room temperature for at least 15min (22 °C–25 °C). The sucrose solution and neuronal ACSF were bubbled with 95% O_2 /5% CO_2 . Recordings were performed in mouse primary visual area cortex.

Patch-clamp recording

Borosilicate pipettes were pulled on the day of the experiment using a horizontal puller (P-97, Sutter Instruments) to a resistance of 4–5 $\text{M}\Omega$. The intracellular solution was composed of (in mM) 135 K-Gluconate, 10 HEPES, 4 KCl, 1 EGTA, 0.3 Na-GTP, 4 Mg-ATP, 10 Na₂-phosphocreatine (pH: 7.2–7.3, 290–300 mOsm). Recordings were performed at room temperature with constant superfusion of oxygenated neuronal ACSF. During the patch clamp experiment, the YOLOv3 neuron detection algorithm, using the unaltered trained network, was run on the desktop PC with the NVIDIA GeForce GTX 1080 GPU on a custom python script to interact with the Rolera Bolt camera. Pipette pressure during patch clamp steps was digitally controlled and pipettes were cleaned according to Kolb et al [60, 31].

4.3 Results

4.3.1 Digital Image Processing for Acute Brain Slices

Conventional Cell Detection and Image Enhancement

To the human eye, Figure 4.2A shows conventional image enhancement techniques marginally improve the visual aid of acute, brain slice images. With binarized thresholding using Otsu's Method (threshold = 144), we have improved contrast on the edge of neurons, but parts of the image become completely blacked out. Contrast stretching and intensity-level slicing do not enhance the soma boundary of the neuron. Likewise, Gaussian sharpening, while increasing the brightness of the image, also does not enhance the soma boundary of the neuron. The inverse, binary mask of the Gaussian adaptive threshold filter shows enhanced soma boundaries but removes any background signal. The contour and Laplacian techniques support the consensus that it is difficult for conventional image processing to determine what is a healthy neuron in a brain slice. However, the best enhancement amongst the group, histogram equalization improves neuron edge contrast while maintaining a majority of the contrast in the background signal. While the adaptive filters and histogram equalization individually make promising image enhancement changes to the original image, the combination of the two in series create a broad generalization of the brain slice image that also reduces the overall information of the image.

To demonstrate that deep convolutional neural networks are necessary for detecting healthy neurons in acute slice, Figure 4.2B shows the results of Canny edge detection on the original image, histogram equalization, and a series of histogram equalization and bilateral filtering. The edge detection images (top) show Canny thresholding prior to any dilation, but on closer inspection, any dilation mask would significantly change the information of neurons present in the slice. Furthermore, in the cell segmentation images (bottom), the white circles overlaid the original image show that the predicted cells, according to the cell segmentation by Hough Circle Transform, are inaccurate.

4.3.2 YOLOv3 Neuron Detection

As previously described, we compared the performance of a network trained on only unaltered images to a network trained on enhanced images. A representative example image of an unaltered image and an enhanced image is shown in Figure 4.3a.

When evaluating the performance of these networks, two metrics can be adjusted to increase or decrease the accuracy of the network's predictions: (1) the confidence threshold, a measure of the probability that a prediction contains an object and (2) the aforementioned IOU. In order to optimize confidence threshold, we evaluated the networks with the F1 scores, using a constant IOU according to machine learning standards (0.45) and a range of confidence thresholds from 0.1-0.9. The relationship between F1 score and confidence threshold for the unaltered network tested on unaltered images can be found in Figure 4.3b. Since there is a peak in F1 score over the range of confidence thresholds, the optimal confidence threshold of 0.3 was used for all further analyses.

In order to test the unaltered and enhanced trained YOLOv3 networks, we evaluated and compared their performance using precision recall and mAP. Precision recall is a useful measure of prediction success. In information reasoning, precision measures the accuracy or percentage of correct predictions, while recall measures how good it is at finding all the correct objects. Figure 4.3c shows the precision-recall curves for both networks, tested on both enhanced and unaltered inputs. The mAP is the area under this curve, summarized in Table 4.1 and displayed in Figure 4.3d.

The unaltered trained network was trained on images without preprocessing. The mean average precision of this network tested on an unaltered test image data set was 77.00%, while the same network tested on a enhanced data set was 54.62%. Conversely, the enhanced trained network was trained on images enhanced with histogram equalization [102]. The mean average precision of this network was 59.10% with unaltered test images and 71.93% on enhanced images.

The F1 scores of both networks are summarized in Table 4.2 and displayed in Fig-

ure 4.3e. The F1 scores of the unaltered network tested on unaltered and enhanced images were 0.8 and 0.67, respectively. The F1 scores for the enhanced network were 0.61 and 0.76, respectively.

4.3.3 Inference Results

The training loss and validation loss for both networks shown in Figure 4.4a highlight the neural network quickly fitting to the training set and converging towards a steady-state of trained weights.

While the results of the models over enhanced images provide relevant information over the precision of the networks, generally, preprocessing each frame during a real-time live-imaging experiment would cause latency issues so further accuracy and confidence score distributions are studied using only the unaltered test images data set. As seen in Figure 4.4b, the mean accuracy of the unaltered net was 0.703 ± 0.296 while the enhanced net was 0.378 ± 0.306 (student's t-test $p < .001$). Figure 4.4c shows the confidence scores distribution for unaltered and enhanced networks tested on the unaltered data set test images. The notches represent the Confidence Interval (CI) around the median, 0.599 and 0.711, respectively. The ends of the boxes are at the first and third quartiles while the whiskers represent the minimum and maximum confidence scores.

Examples of each network identifying neurons in a test image can be found in Figure 4.4d and Figure 4.4e. On the left half side of each subfigure display, each model's reasoning for a neuron is overlaid with red prediction bound boxes on a representative test image. On the right half side of each subfigure, the prediction of the CNN is graded against the expert-annotated test image. A green box represents a correct prediction (true positive). A blue box represents the original annotated bounding box. A red box represents a model prediction that is a false positive. And lastly, a pink box denotes an annotated neuron that was missed by the model (false negative).

Although our average reported inference time for an image was 580 ± 147 ms, this can

be attributed to testing the trained models on the CPU of the notebook PC described in the Methods section. Average inference time testing the trained models on the GPU described in the Methods section was 56.7 ± 1.43 ms. This provides an 18 frame per second real-time detection rate. Furthermore, the training time for each of the models was 18 minutes.

	Unaltered Input	Enhanced Input
Unaltered Trained Network	77.00%	54.62%
Enhanced Trained Network	59.10%	71.93%

Table 4.1: Mean average precision of unaltered and enhanced trained networks tested on unaltered and enhanced input images.

	Unaltered Input	Enhanced Input
Unaltered Trained Network	0.80	0.67
Enhanced Trained Network	0.61	0.76

Table 4.2: F1 score of unaltered and enhanced trained networks tested on unaltered and enhanced input images.

4.3.4 Patch Clamp Experiments

To validate the health of the identified cells, we performed a set of patch clamp experiments on neurons identified by one of the trained neural networks. We chose to use the unaltered trained network since it demonstrated the greatest mAP and F1 scores. A representative image of a neuron identified by the network in patch clamp whole-cell configuration is shown in Figure 4.5a. The distribution of access resistance from these experiments ($n = 9$) is displayed as a box plot in Figure Figure 4.5b. The average R_A was $29.25 \text{ M}\Omega$. The ends of the boxes are the first and third quartiles ($18.7 \text{ M}\Omega$ and $28.27 \text{ M}\Omega$, respectively) while the whiskers are located at $12.97 \text{ M}\Omega$ and $37.86 \text{ M}\Omega$. Further, 8 of 9 patched cells were within the accepted range among patch clamp experts ($< 40 \text{ M}\Omega$) [31]. Representative current clamp and voltage clamp traces are shown in Figures Figure 4.5c and d, respectively.

4.4 Discussion and Conclusion

The use of patch clamping in mammalian brain slices is well documented [103, 104], yet the majority of the technique is still done manually. While research groups have made improvements to automate many of the painstaking steps involved with patch clamping *in vitro* [60, 38, 31, 26], the initial act of selecting a healthy neuron to patch still has yet to be resolved. Thus, the development of this tool enhances patching not only for automated rigs but also for manual patching.

In this study, we developed a method for detecting neurons in acute, rodent brain slice for anticipatory use towards assisting patch clamp experiments. We then validated the method's ability to identify healthy cells by patch clamping neurons identified by the best performing network (unaltered trained network). The application of this neural network in the context of patch clamp has great potential to help fully close the loop towards complete automation of the patch clamp technique on acute brain slices and reduce the need for immense training and skills required for manual identification of healthy cells. The YOLO network architecture's speed and accuracy are conducive for nominating healthy neurons in acute brain slice in real-time with a display and detection rate of 18 frames per second. Thus, this neuron detection method is a tool not only valuable for initially identifying neurons for patching, but it could also provide tracking of the cell location as the slice is moved during an experiment to aid in throughput and quality of the recording. In addition, this work could have several secondary benefits that address the requirements for highly reproducible data [67]. By removing the user from the cell selection process, it inherently reduces experimenter bias, reduces type I & II error and increases experimental rigor.

Both networks performed best when tested with input images that were similar to their respective training data sets. Interestingly, while preprocessing may have improved the contrast of cell boundaries to the human eye, it did not improve the network performance most likely because the enhanced contrast has introduced artifacts that interfere

with the boundaries of the cells. The statistically significant difference in the mean accuracy between the unaltered and enhanced networks support this finding by a student's t-test ($\alpha=0.05$), $p<.001$. Most likely, the non-linear contrast enhancement degraded the image and reduced detectable linear features that may improve a model's precision and accuracy. Furthermore, while the median for the enhanced net is higher than the unaltered net in the distribution of confidence scores, the lower mean accuracy score for the enhanced net shows it may be misleading to determine a neural network's efficiency and precision based on its confidence score.

This study also had some limitations. Since only one class of neurons were chosen, and image acquisition was time-consuming, there was a limited number of images—thus, neurons—for training the neural network for neuron detection. However, further collaboration with patch clamp research groups can help increase the speed and quality of image acquisition. While Koos et al. have conducted a similar deep learning-based method for neuron detection in slice [45], our method achieves similar precision while being more efficient and user-friendly. Using YOLOv3, our F1 score of 80% is comparable to the F1 score of 83.5% by Koos et al. In addition, our CNN has a reduced neural net training time of 0.3 hours while Koos et al. took 159 hours—a 98% reduction. Thus, the deep learning method presented here demonstrates the promise of implementing CNNs even further in the field of electrophysiology. Our study introduces the feasibility of performing classification tasks on acute brain slices by using a sparsely annotated data set (our sparsely annotated data set of 1138 neurons compared to 6344 annotated neurons by Koos et al.) Furthermore, we have demonstrated the advantage of transfer learning in improving network performance, especially when limited data is available, and confirmed that current image enhancement techniques do not necessarily help neural network performance.

The image enhancement techniques used in this method are not comprehensive, and other image enhancement techniques can also be explored particularly for low-contrast, gray-scale images [105] and use of Kalman filtering [106]. In addition, future work can

include customizing the YOLO architecture to optimize network training for our data sets, training on a greater number of annotated images, and upgrading the object detection architecture to YOLOv4 for improved precision. Pruning the YOLO architecture can also improve neuron detection speed [107]. Moreover, this technique could be used to detect and analyze subcellular features such as spines, dendrites, or axons.

Current software will be publicly available on Github (<https://github.com/mightenyip/neuronDetection>). Future work will focus on applying existing models to detecting neurons in real-time prior to patch clamp experiments. In addition, data augmentation methods and the detection model will be optimized to further improve the detection accuracy. Moreover, additional classes can be annotated to expand neuronal detection to other types of neurons. Thus, paving the future for an object detection-based neural network capable of reasoning the entire environment of an acute brain slice.

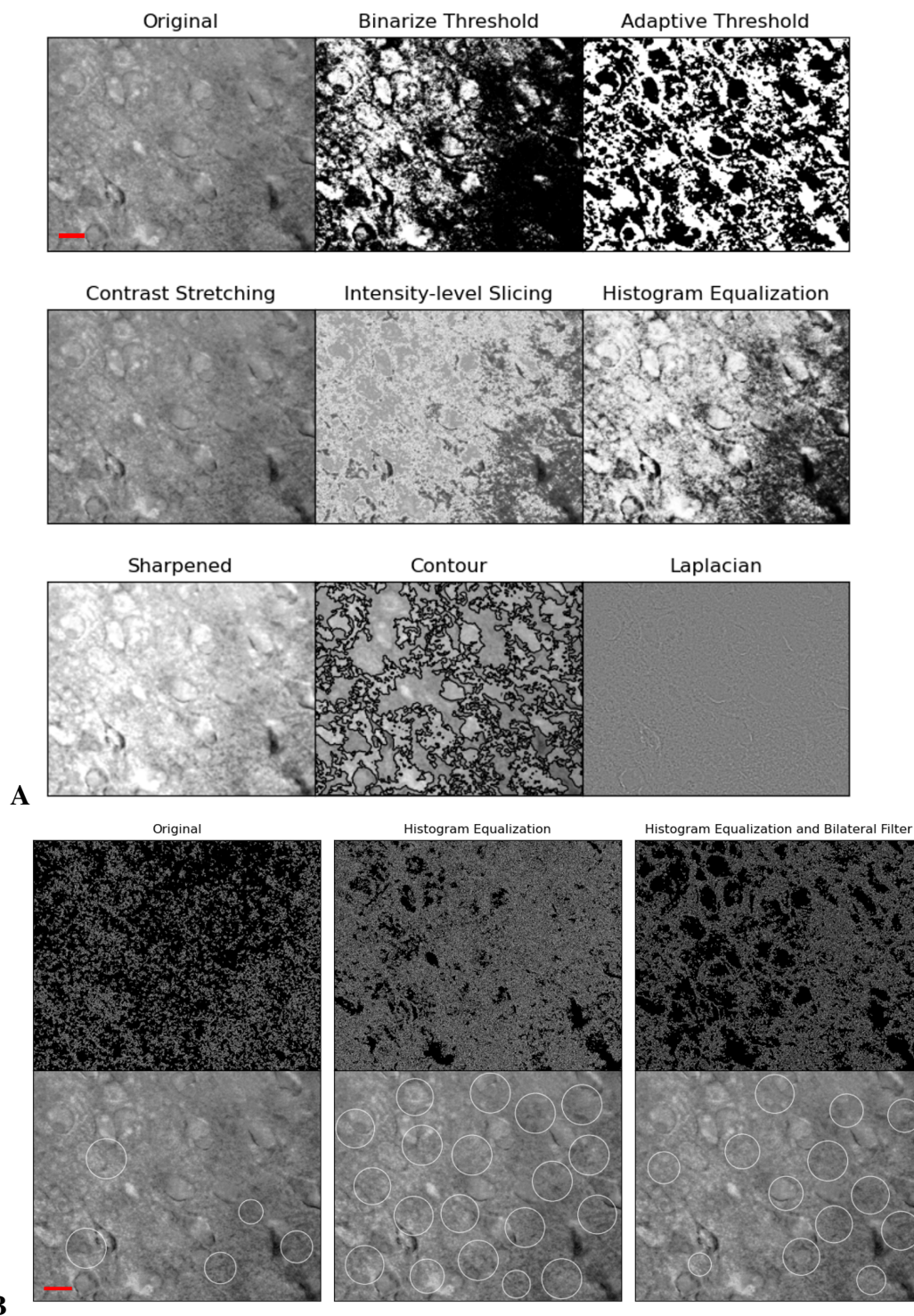


Figure 4.2: (A) Examples of image enhancement techniques: binarize threshold, Gaussian adaptive filter, contrast stretching, intensity-level slicing, histogram equalization, Gaussian sharpening, contour, and Laplacian filtering. (B) *top*: Example of Canny edge detection for original image, histogram equalization, and histogram equalization with bilateral filtering. *bottom*: Subsequent cell segmentation prediction using Hough Circle Transform. Scale bars: $10\mu\text{m}$

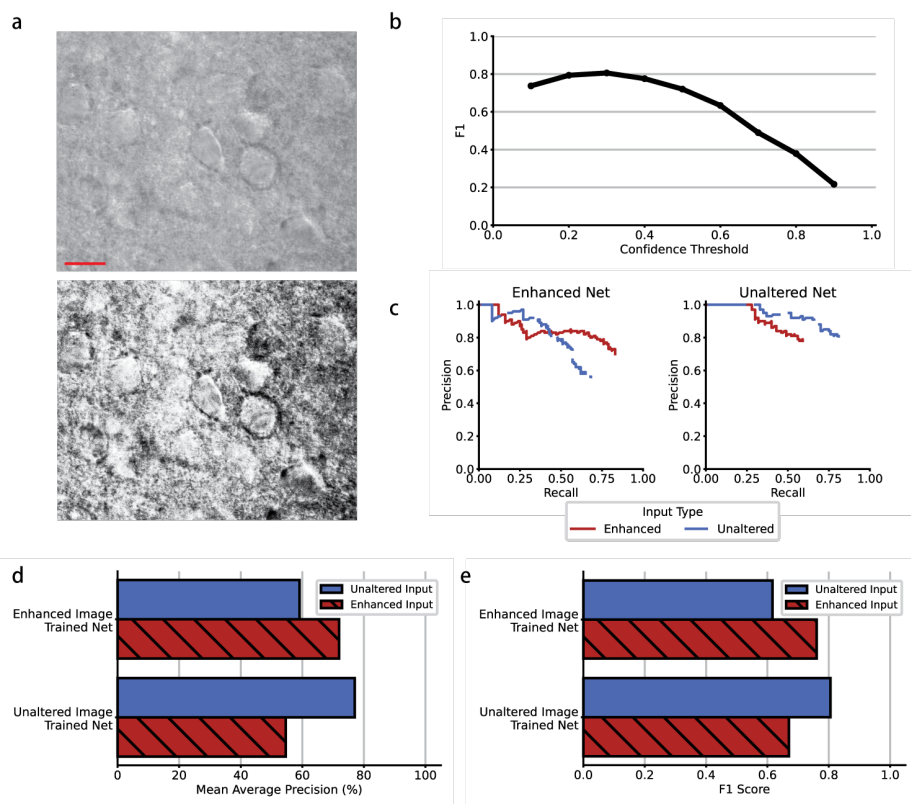


Figure 4.3: (a) Representative example of unaltered (top) and enhanced (bottom) images of acute slice under DIC. Scale bar: 10 μm (b) Representative plot of F1 score vs confidence threshold, demonstrating peak in F1 score at a confidence threshold of 0.3. (c) *left*: Relationship between precision and recall for the enhanced network tested on enhanced and unaltered data set test images. *right*: Relationship between precision and recall for the unaltered network tested on enhanced and unaltered data set test images. (d) Summary of mean average precision of both networks for both enhanced and unaltered inputs (e) Summary of F1 score of unaltered and enhanced networks for both enhanced and unaltered inputs.

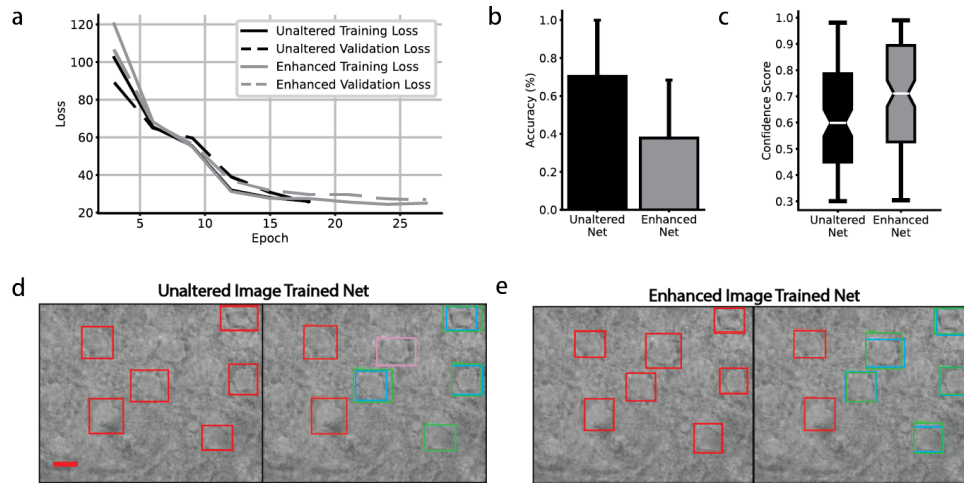


Figure 4.4: (a) Convergence on training and validation loss with respect to number of epochs. Black lines represent the unaltered trained model losses, and gray represents the enhanced trained model losses. Solid lines represent training loss, and dashed lines represent validation loss. (b) The bar chart shows mean \pm SD comparison of the average accuracy between the unaltered net and enhanced net on the unaltered data set test images. A student's t-test ($\alpha=0.05$) acknowledges that the difference between the means is statistically significant; $t(36)=5.12$, $p<.001$. (c) Box plot comparison of the confidence scores distribution for unaltered and enhanced networks tested on the unaltered data set test images. The notches represent the confidence interval around the median using a Gaussian-based asymptotic approximation. The ends of the boxes are at the first and third quartiles while the whiskers represent the minimum and maximum confidence scores. (d-e) Example of both networks identifying neurons in a test image. *left*: initial prediction (red) of neurons. *right*: bounding boxes for annotation (blue), correct prediction (true positive—green), incorrect prediction (false positive—red), and undetected neurons (false negative—pink). Scale bar: 10 μm

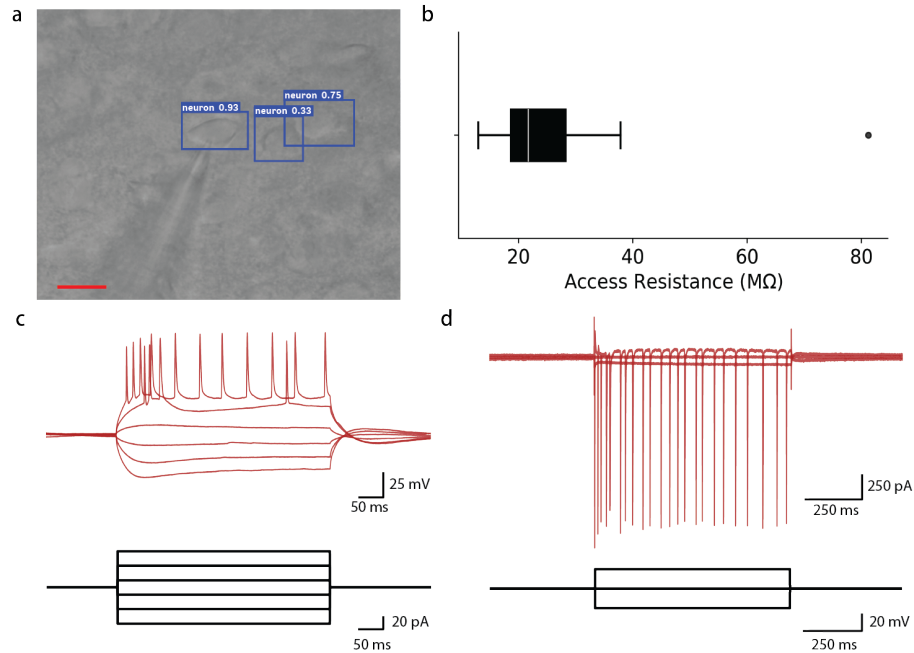


Figure 4.5: (a) Image of a network-identified neuron in patch clamp whole-cell configuration. The blue bounding boxes indicate identified neurons. The numbers ranging from 0 to 1 indicate the network's confidence that the box contains a neuron. The pipette recording electrode is visible on the lower left quadrant resting on the leftmost of the three identified neurons. Scale bar: $10\ \mu\text{m}$ (b) Distribution of access resistance indicate that 8 out of 9 cells (89%) yielded high quality whole cell recordings. The white line indicates the median (21.7), the box width indicates the interquartile range (9.6), and the whiskers indicate the range of the data, excluding outliers. (c) Representative current clamp trace and (d) voltage clamp trace from a neural network-identified neuron in whole-cell configuration.

CHAPTER 5

COORDINATED MULTI-PIPETTE PATCH CLAMP FOR ENABLING HIGH THROUGHPUT SYNAPTIC CONNECTIVITY STUDIES

5.1 Introduction

Patch clamp recording remains the gold-standard technique for high-quality electrophysiological measurements of single cells in brain slices. We have previously developed a robotic system, “the patcherBot,” capable of performing unattended, multi-hour patch clamp experiments in brain slices, with a whole cell success rate of 50%. While this system is broadly useful across neuroscience (i.e., drug screening, cell typing, etc.), the fields of connectomics and synaptic physiology could benefit uniquely from scalable automation. Patch clamp recordings of synaptically connected neurons, traditionally performed with a single user operating multiple manipulators (up to 12) simultaneously, is an incredibly challenging experimental method to master. While the patcherBot has been scaled to two manipulators for high throughput patching in cultured cells and blind, *in vivo* patch clamping, the ability to use multiple manipulators and microscopy to identify connected clusters of neurons in brain slices requires additional algorithm development. Specifically, careful positioning and translation of the electrodes must be performed to maximize the probability of patching synaptically connected neurons, and, simultaneously, avoid potential electrode collisions.

The development of this premeditated manipulator route planning is an advancement towards automated multi-manipulator patch clamping, and it allows for labs to conduct easier “mesoscale” studies on local brain circuits. Figure 5.1 shows the lack of multipatching recordings once there are more than two manipulators involved. The goal of patch-walking is to allow labs to enable higher number of manipulators to probe local brain circuits with

much better efficiency. With the addition of cleaning, to the end of a patch clamp recording, electrophysiologists will be able to prolong the use of one pipette rather than constantly replacing a used pipette. The strategy increases the efficiency for multipatching (Figure 5.2), and its advantages were first shown by Peng et al [104]. The idea in Figure 5.2B is that the addition of forward-thinking route planning along with pipette reuse can maximize the number of potentially probed connections in an experiment. This method of "walking" (which we shall term as patch-walking) can enable a more efficient method than the traditional multipatching idea of "clumping" where electrophysiology experiments would come in with all pipettes to patch and then subsequently remove them all after an attempt.

Dual-patching (two manipulators simultaneously for paired recordings) will validate this novel ideology as a proof-of-concept [108]. Here, we define paired recordings as successful simultaneous recordings from two potentially monosynaptically-connected neurons. The multipatch algorithm utilizes a parallel performance to synchronize the pipettes. While it may seem trivial to scale linearly from 1 to multiple automated pipettes, previous robotic attempts never made each pipette truly independent from each other. The serial approach to linearize the state machine of each manipulator such that functions pertaining to manipulator-1 execute first, followed by functions pertaining to manipulator-2, and so on is cumbersome and requires too much user input. With this architecture, it is unlikely to achieve truly parallel performance— that is manipulator-1 and -2 will never be performing any function concurrently. In addition, manipulators could not be in different stages of the state machine, e.g. one cleaning and one patching. Finally, code organization and individual manipulator timing suffers because every manipulator-related function must be called as many times as there are manipulators. To avoid this conundrum, each manipulator applies a mutex to reserve the camera and stage for calibration and navigation purposes. The camera and stage can therefore only be reserved by one manipulator at a time. The indices of cell locations are kept in a single queue that is accessed by the manipulator modules. To avoid collisions of pipettes, each manipulator is given a set "path" of cells to patch in

order to optimize the number of probed neurons for connections. Furthermore, the previously published version of the patcherBot for brain slices was a single manipulator-based system [31]. Based on previous validation experiments at this scale, the patcherBot can successfully patch 9 cells per hour completely unattended. One can imagine with more manipulators, the yield of recorded cells would increase. Indeed, computational simulations show that a robot with four manipulators has an expected throughput of 25 total cells patched per hour [31].

5.1.1 Motivation

Multipatch setups increase the complexity and time of experiments, necessitating automation. Various groups were able to increase the number of simultaneous recordings [47, 104, 20, 30, 17], but the operation of multiple manipulators is challenging. To address this, several approaches have been reported that automate the patch-clamp process, utilizing automated pressure control systems and algorithms for manipulator movements guided by visual or electrical signals [26, 38, 31]. However, these setups generally are specific to one manipulator while other papers from the Allen Institute and the Geiger lab use eight or more manipulators, a feat currently used by only a few labs. Thus, there is a missing opportunity on two to four manipulators, the mesoscale for multipatching, to enable larger data sets to be gathered in a short amount of time for studying synaptic connectivity.

In Song et al., they discovered that synaptic connectivity in local cortical circuits carried highly nonrandom features [109]. Measurement of the euclidean distance of cell locations for paired recordings compared to Perin et al.'s showed that the previously reported rate of connectivity at $p = 11.6\%$ (931 connections out of 8,050 possible connections), was similar to that reported for rat somatosensory cortex layers 5 and 2/3, as well as those previously reported for rat visual cortical layers 5 and 2/3 [20].

In order to maximize the mesoscale of multipatching, several optimization methods must be considered. First, cleaning pipettes for immediate reuse increases the size of

recorded neuron clusters and enables a more complete view of the microcircuit. The maximum number of simultaneously recorded neurons is highly limited by the spatial constraints imposed by the manipulators. Furthermore, the success of a whole-cell (WC) recording depends on mechanical interference, deterioration of recording quality during prolonged experimental time and tissue quality. These factors are aggravated when the number of pipettes is increased. This technique has already been implemented for automated patch-clamp of multiple neurons in vivo or single neurons in vitro [110, 31]. Sequential recordings from multiple cells using the same pipette would also overcome the limitation on maximum cluster size given by the number of manipulators in use. This will provide a more complete view of the microcircuit enabling the analysis of more complex network motifs and higher degree distributions [20, 109]. In order for sequential recordings from multiple cells to succeed however, a forward-thinking route-planning algorithm must be developed in order to maximize the probability of connection between two probed neurons.

Thus, we introduce a fully automated, user-free in vitro multipatch approach with a pipette route-planning system to "walk" across a brain slice and record up to 10 neurons. Here, we show that this approach further increases the rate of potential neurons probed, decreases experimental time and enables sequential patching of additional neurons.

5.2 Methods

5.2.1 Computational multipatching modeling

A series of simulations, modeling, and algorithm development were conducted to showcase the advantage to using the full automation of the patcherBot towards coordinated, multipipette patch clamping ("multipatching"). The computational model was built in MATLAB (Mathworks) and integrated into the patcherBot software in LabView.

For the route planning and collision avoidance algorithm ("patch-walking"), we assumed that an automated, multipatching system can be operated and unattended for multi-

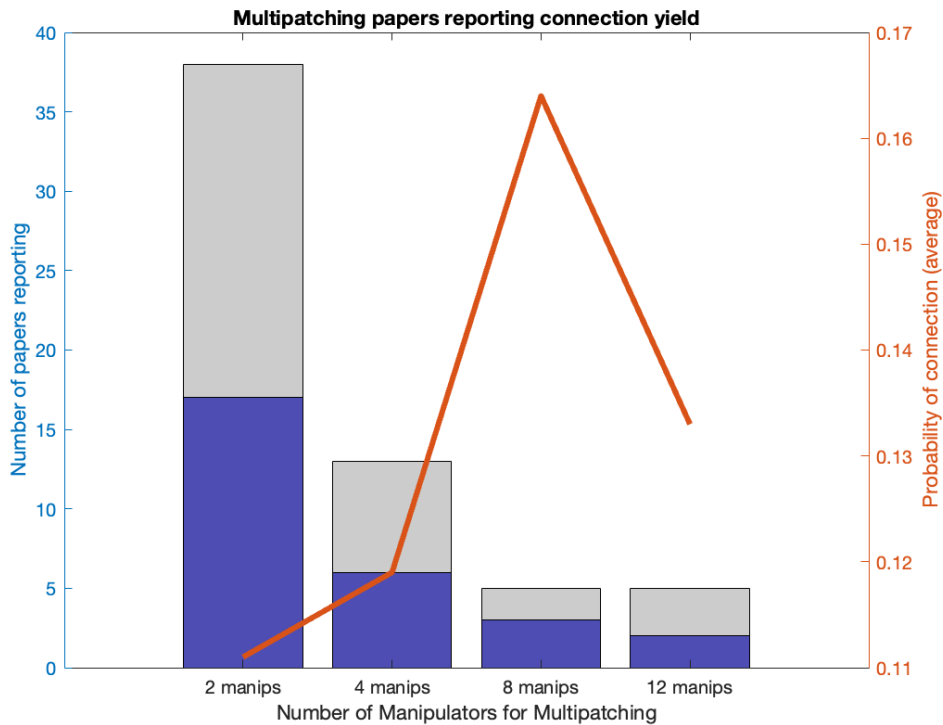


Figure 5.1: Multipatching recordings are desirable but difficult to perform. A literature review (done in 2020, total of 75 papers) of papers that performed multipatching in vitro in mice and rats were analyzed to determine the average number of measured connections. The bar chart shows the number of papers that used X manipulators for a patch clamp connectivity experiment. The blue part of the bar chart shows how many of the papers reported their probability of connection yield. This showcases the low efficiency for probing connectivity amongst a local brain circuit. The line graph shows the probability of connections reported for the number of manipulators used.

ple hours. Using experimental data gathered from the single-manipulator PatcherBot [31] and literature data on connectivity rates [20], we built a computational model to simulate how a multipatching robot could sample a greater number of possible connections in a single experiment (Figure 5.2A). The methodology of clumping vs. patch-walking was also incorporated to highlight the efficiency in using the patch-walking algorithm to profile connections in brain slice (Figure 5.2C). Lastly, the patch-walking algorithm shows a unique route-planning pathway based loosely on the Monte Carlo Tree Search algorithm (Figure 5.2D).

For the Monte Carlo Tree Search Monte Carlo Tree Search (MCTS) algorithm, nodes

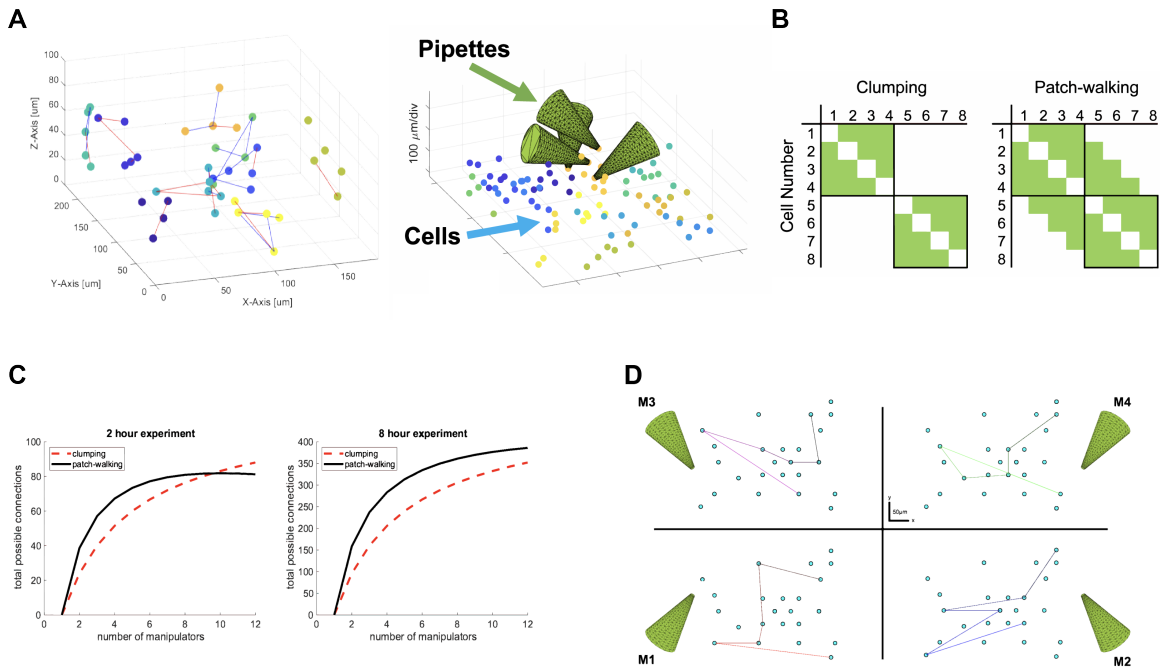


Figure 5.2: a. Representation of a computational simulation modeling the connection of neurons with each other with respect to their clusters in a brain slice. Further, an example of the computational model showing multiple pipettes patching different cells. b. An argument for patch-walking rather than clumping as a desirable multipatching algorithm in order to optimize efficiency of probing connections. This a 4-manipulator example showing the increased number of probed connections in green squares outside the black bounding boxes. c. Modeling throughput simulation of how patch-walking increases the number of maximum probed connections as a function of number of manipulators (4-minute patch attempts per manipulator). The 2-hour and 8-hour time representations show the time-cost generally for setting up a large number of manipulators.

(or in this case, neurons), are the building blocks of the search tree. These nodes are formed based on the outcome of a number of simulations. The process of the Monte Carlo Tree Search can be broken down into four distinct steps, selection, expansion, simulation and backpropagation. Selection begins the initial strategy to traverse from the root node down the tree using a specific strategy. Here, we used (1) neuron location, (2) locations of other pipettes, and (3) maximum distance between two probed cells as the primary criteria for node selection. During tree traversal, a node is selected based on the scoring of these parameters to return the maximum value [111]. For the neuron selection criteria, we categorized the bounding box of neurons to a 200 x 200 μm Field of View (FOV) window. We then prioritized for route-planning to avoid collisions between pipettes such that there was a 10 μm safety buffer around the modeled pipette. The base location of each pipette was standardized to the safe space calibrated within the patcherBot software for each manipulator. Lastly, the maximum distance allowed between two patched neurons was less than 200 μm in order to have at least a 10% probability of connection according to Perin et al. [20].

The order for patching neurons was then updated for the maximum or best score attributed to a successful "walk" across the brain slice with specified number of manipulators. Using a prescribed set of neurons, we validated the method of the model within the patcherBot software seen in Figure 5.3. We also validated, for a given random distribution of cells within a large field of view, the patch-walking algorithm would avoid collisions (Figure 5.4).

5.2.2 Multipatching patcherBot

Hardware

We ran multipatching, automated patch clamp experiments using a standard electrophysiology rig with two PatchStar micromanipulators. Samples (brain slices) were imaged using a 40X objective (LUMPLFL40XW/IR, NA 0.8, Olympus) on a motorized focus drive, il-

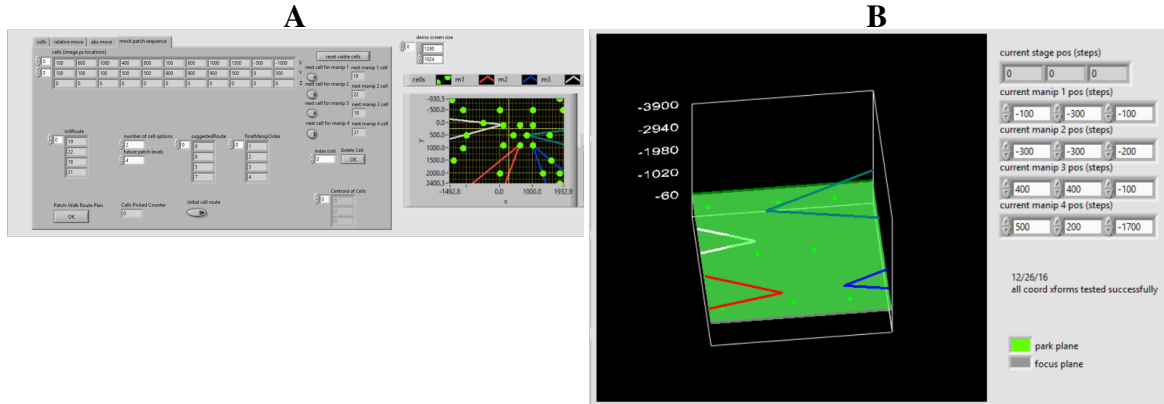


Figure 5.3: GUIs made to theoretically demonstrate the route-planning of patch-walking. a. Representative patch-walking sequence of cells represented in a 2D plane. b. Representative patch-walking validation in a 3D plane highlighted by the position of the manipulators.

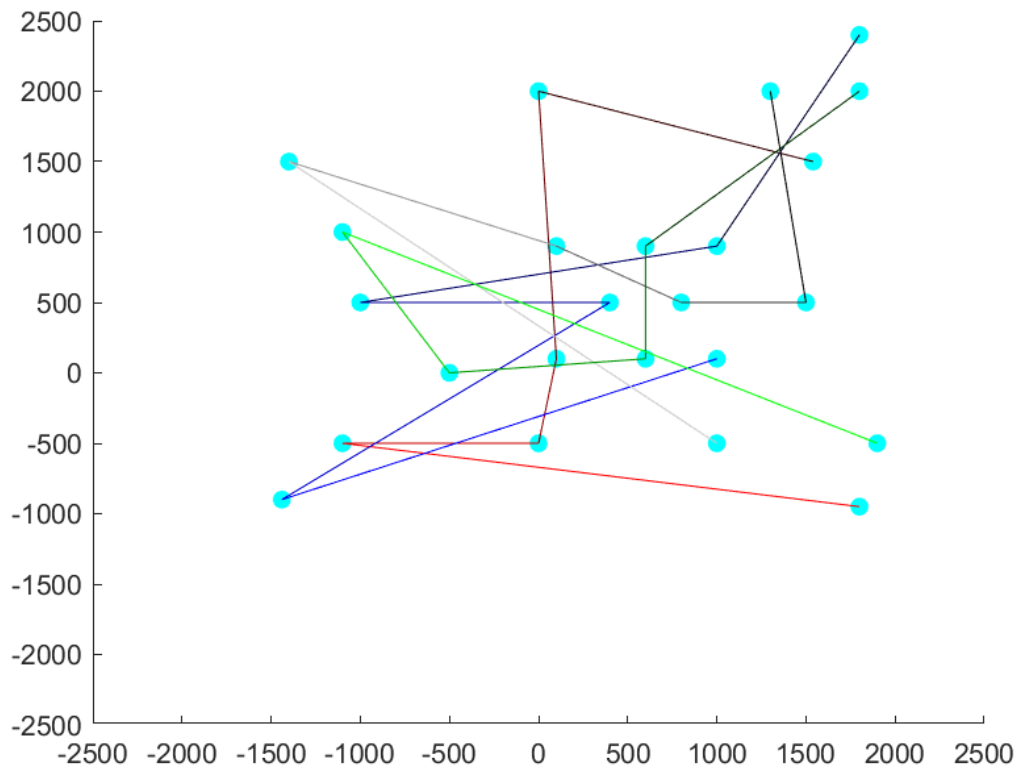


Figure 5.4: Representative route-planning path for 4 manipulators in a large ($> 200 \mu\text{m}$) field of view. Axes are in steps which are a 10:1 ratio to μm . The cyan dots represent cells. The line getting increasingly blue represents the path of manipulator-1. The line getting increasingly red represents the path of manipulator-2. The line getting increasingly gray represents the path of manipulator-3. The line getting increasingly green presents the path of manipulator-4.

luminated under DIC with an infrared light-emitting diode (780 nm), and captured with a Rolera Bolt camera (QImaging). We used a peristaltic pump (120S/DV, Watson-Marlow) to perfuse the brain slices with aCSF solution. We also a custom machined brain slice sample holder with a smaller side chamber for cleaning solution. We followed the cleaning protocol as suggested by [60], however we did not include rinsing in the cleaning protocol because recent literature found that there is no impediment to the whole cell yield or quality of recording [32, 104].

Electrode pressure was controlled using a custom pipette pressure controller enabled up to four-channels. For each pipette, pressure was controlled by a ± 10 psi regulator (QPV1TBNEEN10P10PSGAXL, ProportionAir) using an analog (0-10 V) control signal. The control signal for each regulator was generated by a microcontroller (Arduino Due) via a digital-to-analog converter (MAX539, Maxim Integrated). In order to minimize valve switching to efficiently scale up the patcherBot to multiple manipulators and pipette pressure control, a custom PCB circuit board was developed to control up to a maximum of 4 manipulators. Individual pressure regulators for each pipette were necessary to ensure that different pressures could be maintained on each pipette, e.g. if one pipette is forming a seal (atmospheric or negative pressure), and another is approaching a neuron (positive pressure). The custom pressure controller regulates house-air line to deliver -500 to +700 mbar using an inline venturi tube (SMC) and solenoid valve (Parker Hannifin) for rapid pressure switching [31, 26, 112].

For real-time electrophysiology feedback and collection, we used the Multiclamp 700B amplifier (Molecular Devices), and cDAQ-9263/9201 and USB-6221 OEM data acquisition boards (National Instruments) to collect recordings. In addition, we used the Axon Digidata 1550B during paired recordings. A unique DAQ was used for each manipulator in order to simultaneously acquire different signals from each pipette. This is particularly important for asynchronous and independent pipette control.

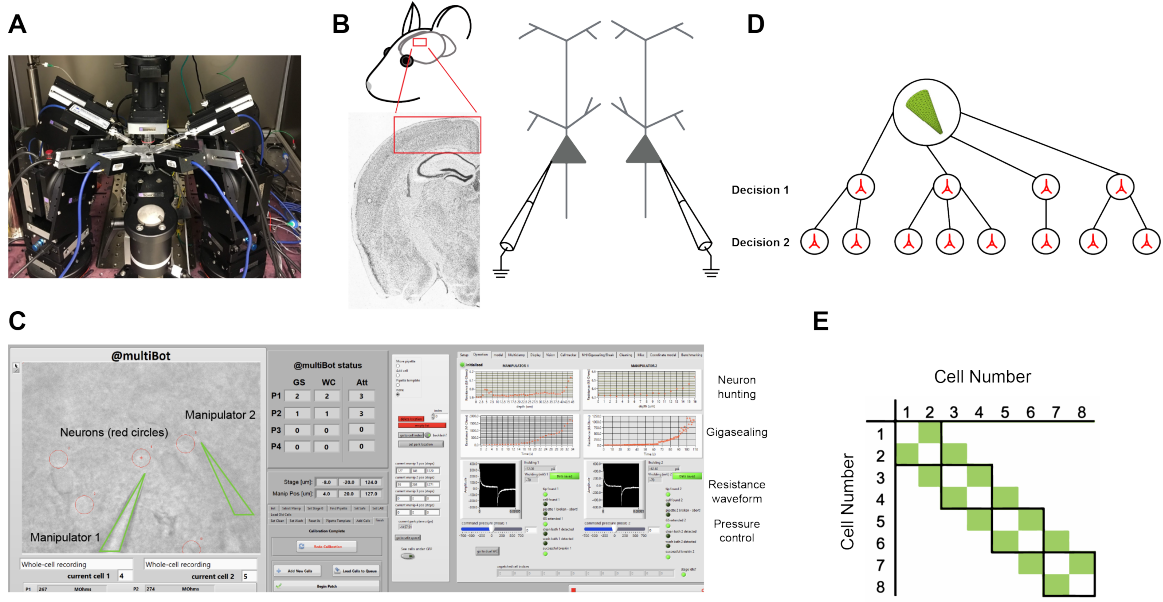


Figure 5.5: a. Multi-manipulator patcherBot system. b. Specific mouse brain regions of patching where in the primary visual and somatosensory cortex. c. Software overview of the patcherBot LabView graphical user interface. d. Monte Carlo Tree Search decision tree example for a pipette. e. Matrix representation for patch-walking efficiency upgrade with 2 manipulators (dual-patching).

Software

Custom LabVIEW code (National Instruments) integrating manipulators (electrode and microscope), camera view of the microscope stage, and pressure control box was implemented to control the rig and enable automated experimentation based off the patcherBot software developed by Kolb et al. 2019. The Graphical User Interface (GUI) was designed with tabs to help the user keep track of different parameters with the main module displaying the critical information: DIC imaging, pressure control, manipulator position, electrophysiology data, real-time resistance feedback, and current state machine of the automated patcherBot.

For the demonstration of patch-walking with multiple pipettes, we focused on using 2 pipettes to highlight the functionality of the idea and method. In order for independent pipette control to continually probe new neurons, each manipulator was required to function asynchronously of other manipulators. This included unique resistance feedback during the patch clamping protocol, a re-entrant sub-module for the state machine of each pipette (as

described in Kolb et al. [31], and independent calibrations to ensure the positioning errors were mitigated.

The patch-walking algorithm was implemented within the “pick cell” state of the patcher-Bot state machine. The “pick cell” state ensures that each manipulator is assigned to the cell closest to its home position from an array of un-patched cell indices or in this scenario, based on the MCTS-based patch-walking algorithm which assigned a score to each neuron indicating its overall suitability for the route path. The second addition to the dual patch algorithm was the “microscope reservation” feature which ensured that each manipulator could “reserve” the microscope stage and imaging system for the pick cell, calibration, pipette descent, and cell approach states. It was essential that each manipulator had complete control over the microscope during these steps since they rely on camera output. If a manipulator was ready for the “pick cell” stage, but the microscope was reserved by the other manipulator, it would wait until the microscope was unreserved.

5.2.3 Brain slice preparation

All animal procedures were in accordance with the US National Institutes of Health Guide for the Care and Use of Laboratory Animals and were approved by the Institutional Animal Care and Use Committee at the Georgia Institute of Technology. For the brain slice experiments, male mice (C57BL/6N, P19–P36, Charles River) were anesthetized with isoflurane, and the brain was quickly removed. Coronal sections (300 μm thick) were then sliced on a vibratome (Leica Biosystems VT1200S) while the brain was submerged in ice-cold sucrose solution containing (in mM) 40 NaCl, 4 KCl, 1.25 $\text{NaH}_2\text{PO}_4\cdot\text{H}_2\text{O}$, 7 MgCl_2 , 25 NaHCO_3 , 10 D-Glucose, 0.5 $\text{CaCl}_2\cdot 2\text{H}_2\text{O}$, 150 Sucrose (pH 7.3–7.4, 300–310 mOsm). The slices were incubated at 37 °C for 1 h in neuronal artificial cerebro-spinal fluid (aCSF) consisting of (in mM) 124 NaCl, 2.5 KCl, 1.25 $\text{NaH}_2\text{PO}_4\cdot\text{H}_2\text{O}$, 1.3 MgCl_2 , 26 NaHCO_3 , 10 D-Glucose, 2 $\text{CaCl}_2\cdot 2\text{H}_2\text{O}$, 1 L-Ascorbate $\cdot\text{H}_2\text{O}$ (pH 7.3–7.4, 290–300 mOsm). Prior to recording, the slices were maintained at room temperature for at least 15min (22 °C–25

°C). The sucrose solution and ACSF were bubbled with 95% O₂/5% CO₂. Recordings were performed in mouse primary visual area and somatosensory cortex.

5.2.4 Patch-clamp recording

Borosilicate pipettes were pulled on the day of the experiment using a horizontal puller (P-1000, Sutter Instruments) to a resistance of 4–6 M Ω . The intracellular solution was composed of (in mM) 135 K-Gluconate, 10 HEPES, 4 KCl, 1 EGTA, 0.3 Na-GTP, 4 Mg-ATP, 10 Na₂-phosphocreatine (pH: 7.2–7.3, 290–300 mOsm). Recordings were performed at room temperature with constant superfusion of oxygenated neuronal ACSF. Pipette pressure during patch clamp steps was digitally controlled and pipettes were cleaned according to Kolb et al [60, 31].

5.2.5 Dual-patch experimental validation

During the patch clamping experiments, the user first identified all viable neurons within a 200 x 200 μ m FOV of the sample. The algorithm then evaluated each neuron based on the patch-walking criteria described above. To evaluate the dual-patching and patch-walking performance, the user chose 4-10 neurons. An attempt was considered successful upon the successful completion of the break-in state. After an automated whole-cell recording protocol, the software switched over to Clampex (Molecular Devices, San Jose, CA, USA), a electrophysiology recording software, for connectivity studies. After successful attempts by both pipettes, paired recordings were conducted to test for connectivity.

After the both manipulators conducted their first attempts, the algorithm re-evaluated the remaining neurons in the un-patched cell index and updated the next cell to be patched for that specific manipulator. After the first successful paired recording, the manipulator that held its cell under whole-cell configuration the longest would then release the cell, clean the pipette, and come back for another patch attempt with the next, updated cell to patch. The algorithm then repeated the process of selecting until all viable neurons had

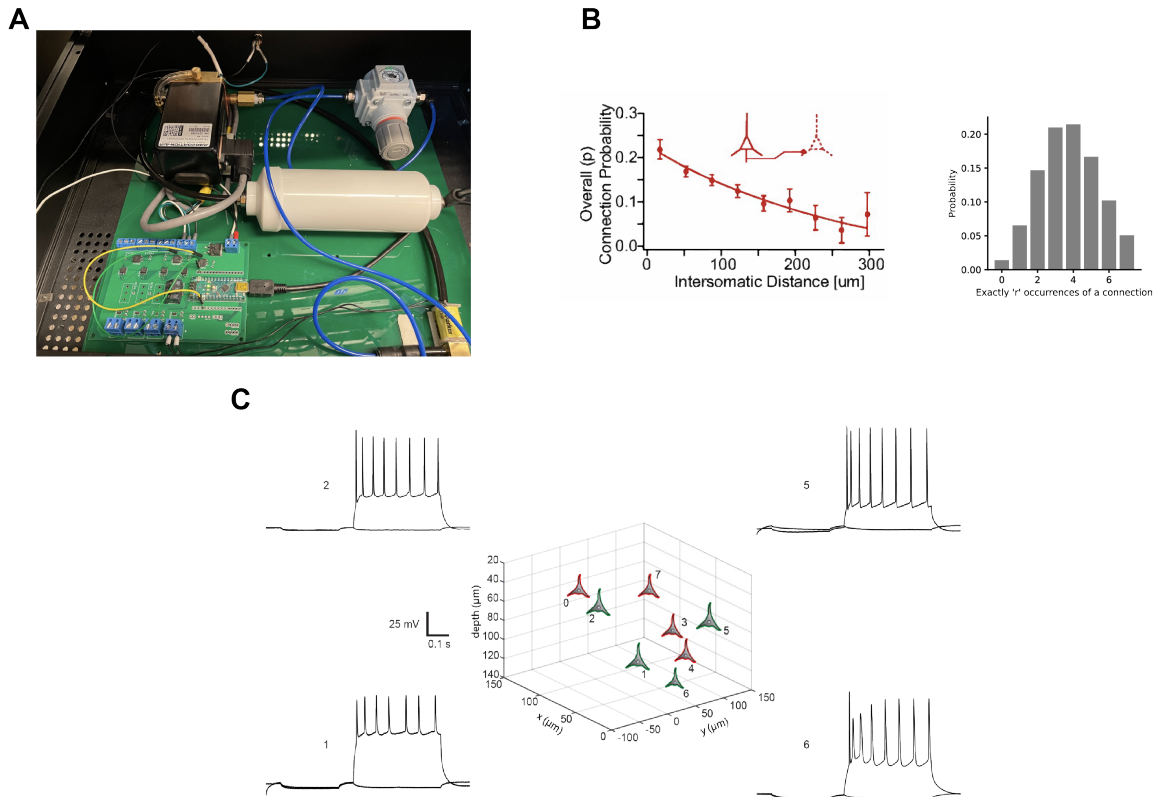


Figure 5.6: a. Picture of the custom pressure control box. b. Connection probability as a function of intersomatic distance between neurons from Perin et al. [20]. c. Representative 3D-example of throughput for dual-patching explicitly not for connectivity. The cells in green indicate successful patches while red indicates failed patches. Representative current clamp traces are included for the successfully patched cells.

been patched.

To validate the performance of automated dual-patching as a proof-of-concept, we wanted to benchmark the efficiency of our patch-walking algorithm to that of the Allen Institute [46]. Similar to Peng et al., we wanted to benchmark the utility of patch-walking in a connectivity matrix [104]. Furthermore, general quantitative cell statistics for quality of recording will be conducted.

5.2.6 Statistics

The success rate of the dual-patcherBot was considered as a function of (1) number of paired recordings per experiment per pipette, (2) time to paired recordings, (3) distance be-

tween neurons for paired recordings, and (4) binomial probability of connection,. Standard whole-cell electrophysiology cell quality statistics were also conducted for access resistance, input resistance, capacitance, tau, and resting membrane potential. Analyses and statistics were computed using Python. Data are presented as mean \pm standard deviation unless otherwise stated.

5.3 Results

(For a demonstration of the first ever forward-thinking multipatching robot using a coordinated route plan for automatic, sequential recordings in a brain slice. We aimed to show a representative dataset for dual-patching throughput of paired recordings with the ability to "walk" through a slice and avoid pipette collisions. As a first validation step, we conducted a short dual-patch throughput experiment for two pipettes patching in a brain slice without testing for connectivity or any route-planning Figure 5.6C. We achieved whole-cell success rates of 45.5% (n=15) with manipulator-1 achieving 44.4% (n=8) and manipulator-2 achieving 46.7% (n=7). This is similar to success rates for manual patching as well as previously reported automated patch clamp robots (43%-51% for Kolb et al.) [31].

For dual-patch connectivity recordings, we then implemented a simultaneous recording state to test for connections between paired recordings. To demonstrate the utility of the coordinated, dual-patching robot, we conducted a pilot study over 6 experiments. We determined several stages– neuron-hunting, gigasealing, and whole-cell success– as stages during the patching process to categorize for throughput success. Out of 122 total attempts for both pipettes, we had 116 successful neuron-hunts (95.1%), 64 successful gigaseals (52.5%), and 64 successful whole-cells (52.5%). This was also in line with previously reported automated patch clamp work such as Kolb et al. (mentioned above), Wu et al. (43.2%), and Koos et al. (63.6% for rat, 37% for human) [45, 38]. In addition, our success rates fall within the highly variant success range of manual users (30-80%) on DIC-based patch clamp systems [113].

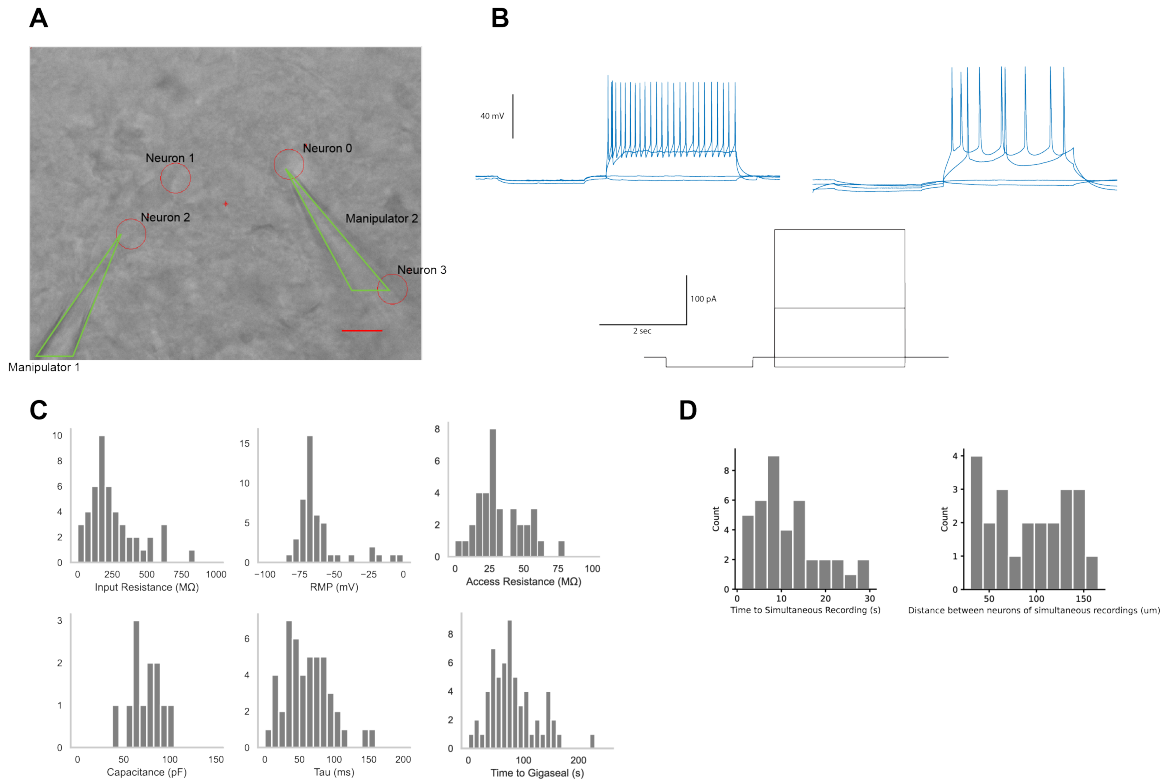


Figure 5.7: a. Representative field of view for dual-patching with the pipettes in view (green) and neurons in the un-patched cell index (red). Scale bar: $10 \mu\text{m}$. b. Representative current clamp traces of both cells prior to connectivity testing. c. Histograms of standardized quality control whole-cell electrophysiology statistics along with time to gigaseal. d. Histograms of time to simultaneous, paired recordings and the distance between neurons during paired recordings.

In Figure 5.7A, we show a representative example of both pipettes in the imaging camera's field of view as well as neurons of interest that are being patched or in the un-patched cell index. Figure 5.7B then shows example current clamp traces in response to current pulses applied during whole-cell recording prior to the simultaneous recording state. Injected current pulses were 3 sec-long pulses from -20pA to +280 pA in 20 pA steps with a 2 sec, -20 pA hyperpolarizing step 500 ms prior. Figure 5.7C shows a histogram of standard quality cell statistics of whole-cell recordings. The average input resistance for these recordings were $286.7 \pm 207.5 \text{ M}\Omega$, the average access resistance for these recordings were $34.2 \pm 16.7 \text{ M}\Omega$, and average resting membrane potential was $-63.8 \pm 17.4 \text{ mV}$. In addition, the time to gigaseal was also monitored with an average of $80.6 \pm 43.4 \text{ sec}$.

Towards studying connectivity with paired recordings, we also tracked the time to simultaneous recordings between two pipettes as well as the distance between two neurons. This was helpful in two ways, to validate that the patch-walking algorithm did not pass the maximum distance requirement during route-planning and the utility of this robot to quickly and sequentially search for connections in a brain slice. The histograms in Figure 5.7D shows the time to simultaneous paired recording with an average of $11.6 \pm 6.83 \text{ sec}$, and the average distance between two neurons for screened for connection to be $93.7 \pm 0.170 \mu\text{m}$, well under the MCTS threshold in the patch-walking algorithm.

For the final validation step of the patch-walking, dual-patching robot, we set out to demonstrate a connectivity matrix similar to those done by previous labs such as Peng et al. and the Allen Institute for Brain Science [104, 114]. From the 64 whole-cell recordings we gathered from the dual-patcherBot, we report a yield of 38 total simultaneous recordings. Of those 38 recordings, 23 paired recordings (i.e. 46 probed connections) passed quality control checks and were used to validate the efficiency of the patch-walking algorithm. Given the difficult nature of patching in brain slice, out of the 64 WCs, only 56 had a potential to be paired with a second neuron for connection screening. From Equation 5.1 and Equation 5.2, we see the additional connections screened with the effect of patch-

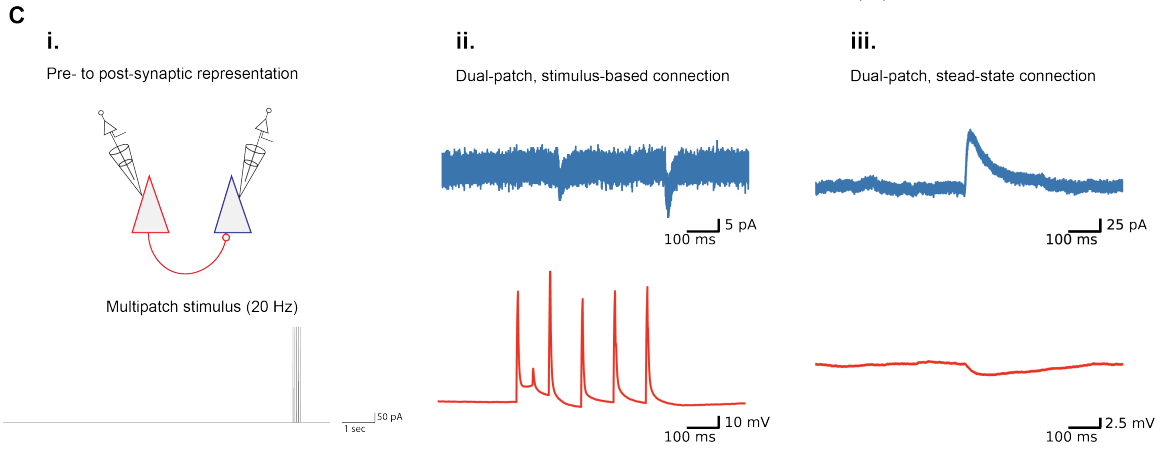
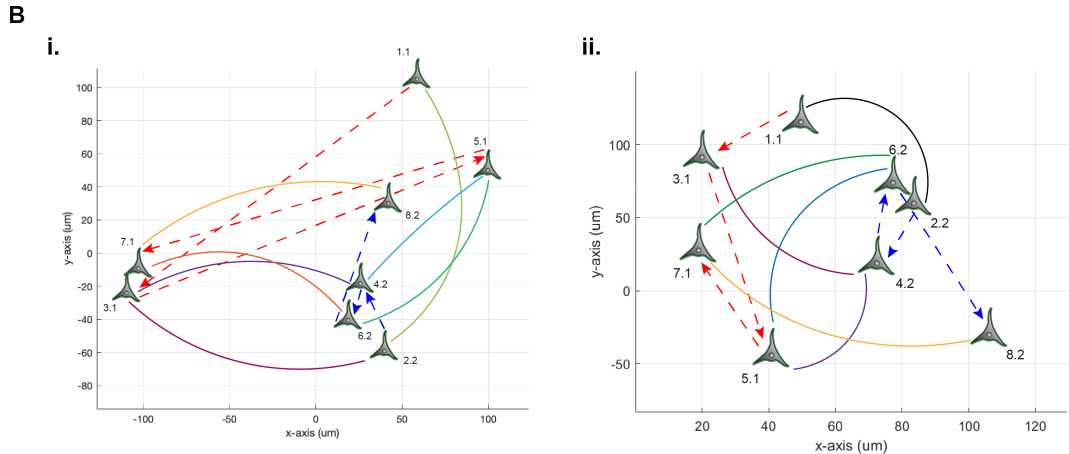
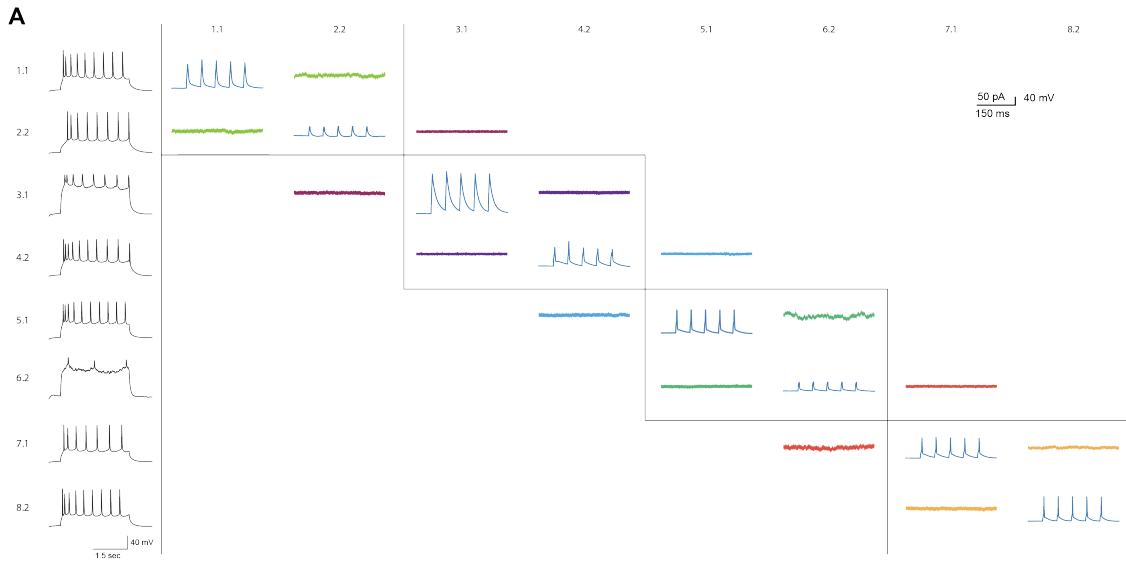


Figure 5.8: a. Matrix of voltage and current traces from 8 neurons in one acute brain slice recorded using the patch-walking algorithm for the dual-patcherBot. Left column shows the firing pattern of the recorded neurons. Cells are numbered such that the first number represents the cell and the second number represents the manipulator. In the first session, two neurons were patched simultaneously (cells numbered 1.1 and 2.2). Traces recorded from one cell are shown in a row with the same color. Five action potentials were elicited in each neuron consecutively (diagonal of the matrix). The postsynaptic responses of the other neurons are aligned in the same column. After recording of the first pair of neurons, the pipette with the earlier whole-cell was cleaned and an additional neuron based on the patch-walking algorithm was patched and recorded with the same stimulation protocol (2.2 and 3.1). After the second recording session, the second pipette was sent to clean and a new cell was patched while manipulator-1 on cell 3.1 was not removed. This allowed screening of additional connections due to the pipettes "walking" across the slice rather than just only a single paired recording. Scale bars: Horizontal 1.5 s for firing pattern, 150 ms for connection screening. Vertical 40 mV for action potentials, 50 pA for postsynaptic traces. b. (i) Patch-walking scheme of all neurons from the experiment matrix in (a). The dashed arrows represent the patch-walking route plan for manipulator-1 (red) and -2 (blue). The curved lines between neurons represent probed connections as color-coded in the matrix in (a). (ii) Second example of patch-walking scheme for a different experiment. The clumping method was initiated for the first paired recording session (1.1 and 2.2) before patch-walking was initiated. c. (i) Schematic representation for connection screening with the pre-synaptic cell in red and post-synaptic cell in blue. The connectivity stimulus to screen for connections is shown below with a train of 5 action potentials elicited at 20 Hz. (ii) Representative connection between two neurons from the connectivity stimulus. (iii) Representative connection between two neurons during steady-state, spontaneous recordings.

walking. Without patch-walking, we would have only been able to screen a maximum of 28 paired recordings. Empirically, we also note from quality metrics, we would have only been able to probe 12 paired recordings. Thus, utilizing the patch-walking algorithm highlights immediate dividends of its efficiency increase.

$$\text{possible connections}_{clumping} = n_c * (m^2 - m), \quad (5.1)$$

$$\text{possible connections}_{patch-walking} = (m^2 - m) + 2(n_{pw} - 1)(m - 1), \quad (5.2)$$

for $n_{pw} \gg n_c$,

where n_c is the number of cells, n_{pw} is the number of cells in a patch-walking experiment, and m is the number of manipulators.

In Figure 5.8, we showcase a connectivity matrix as well as example cases of connections found during the 6 experiments. The matrix in Figure 5.8A shows both voltage and current traces from 8 neurons in one acute brain slice recorded using the patch-walking algorithm for the dual-patcherBot. The left column shows the firing pattern of the recorded neurons. Cells are numbered such that the first number represents the cell and the second number represents the manipulator. In the first attempt, two neurons were patched simultaneously (cells numbered 1.1 and 2.2). Traces recorded from one cell are shown in a row with the same color. Five action potentials were elicited at 20 Hz in each neuron consecutively (diagonal of the matrix). The postsynaptic responses of the other neurons are aligned in the same column. After recording of the first pair of neurons, the pipette with the earlier whole-cell was cleaned and an additional neuron based on the patch-walking algorithm was patched and recorded with the same stimulation protocol (2.2 and 3.1). After the second recording session, the second pipette was sent to clean and a new cell was patched while manipulator-1 on cell 3.1 was not removed. This allowed screening of additional connections due to the pipettes "walking" across the slice rather than just only a single paired recording. In Figure 5.8B(i), the patch-walking route is shown for the experiment matrix.

The dashed arrows represent the patch-walking route plan for manipulator-1 (red) and -2 (blue). The curved lines between neurons represent probed connections as color-coded in the matrix. With Figure 5.8B(ii), it was another patch-walking route for a different experiment (matrix not shown) which includes an initial method of clumping such that there was no immediate walking after the first paired recording attempt. Patch-walking was initiated for the remaining 6 neurons to showcase the versatility of the patch-walking algorithm.

In Figure 5.8C, we see in a schematic representation for connection screening with the pre-synaptic cell in red and post-synaptic cell in blue. In the following panels (ii) and (iii), we show traces that highlight connections found between two neurons from the connectivity stimulus recording as well as a connection during steady-state, spontaneous recordings. Stimulus spike trains were able to produce excitatory postsynaptic currents (EPSCs) and inhibitory postsynaptic currents (IPSCs).

To validate the performance of automated dual-patching as a proof-of-concept, we benchmarked the efficiency of our patch-walking algorithm to that of the Allen Institute [46]. According to their results, the Allen Institute probed 20,949 possible connections over 1,715 experiments with 8 manipulators for an efficiency rate of 1.5 possible connections per experiment per pipette. While a small sample size, here we show that the patch-walking dual-patcherBot was able to achieve 46 possible connections over 6 experiments with 2 manipulators for an efficiency rate of 3.8 possible connections per experiment per pipette. A two-fold improvement for labs unable to or uninterested in maximizing the number of manipulators on their rig.

In the literature review (Figure 5.1) done for multipatching papers, 2-manipulator papers that reported their connection yield had on average a $11.1\% \pm 11.5\%$ probability of connection. The maximum probability of connection yield reported was 38.4% which explains that there are many low values and a tail off to the right (i.e. strong right skewness and a peak near the minimum). To compare our patch-walking, dual-patching robot to

reported results, we first used Perin et al.'s model (Figure 5.6B) for probability of intersomatic connectivity as a function of distance [20]. From the average distance between two probed neurons we determined a connection probability, P , of 17.0% between probed neurons. Utilizing Equation 5.3, which describes the likelihood of at least one connection being found within our 23 paired recordings, we see that:

$$P(\text{at least 1 connection}) = (1 - P(\text{probability of no connection based on distance}))^n, \quad (5.3)$$

which describes the probability of at least one connection occurring based on the distance between two probed neurons and n is the number of trials.

Given the probability connection, P , the probability of us finding at least one connection was 98.6%. With our connectivity recordings, we were able to find 2 connections amongst the 23 paired recordings. While our 4.35% success rate of finding connections is relatively low, it still falls within the standard deviation range for other reported yield of dual-patching papers. Furthermore, we also look at the binomial distribution (probability density function) of exactly 0, 1, 2...etc. connections being found given our empirical data. Figure 5.6B shows the distribution from Equation 5.4 stated below:

$$\binom{n}{r} (P^r)(1 - P)^{n-r}, \quad (5.4)$$

where n is the number of trials or connections probed, r is the number of occurrences expected to be a connection, and P is the probability from Equation 5.3. This equation describes the binomial distribution of exactly 'r' number of connections occurring from the dual-patcherBot paired recordings. For the lower distribution, the chance to find exactly 0, 1, or 2 connections is a combined 22.6% which is close to finding exactly 3 (21.0%) and exactly 4 (21.4%) connections.

5.4 Discussion

The results and methods presented here facilitate previously significant technical limitations for probing synaptic connections on the whole-cell electrophysiological level. This optimized method of patch-walking enables increased efficiency and is widely applicable to not just heroic efforts to atlas the brain but also to study small-scale changes between pairs of neurons for neurological diseases.

Previously, local circuit connectomics was inefficient and deemed only possible for labs with massive electrophysiology resources because synaptic physiology studies require simultaneous pipette patch clamping with up to 12 manipulators. With the fully automated dual-patcherBot and the inclusion of a forward-thinking, route optimization plan, we enable a pivotal increase in the throughput and efficiency for probing connections for research labs that do not have the resources or experimental plans for a large number of manipulators.

Towards the goal of answering questions regarding the role of synaptic connectivity in physiological networks and for providing “ground truth” data to inform higher throughput experimental and computational work, the patch-walking, dual-patching robot can play an important role in the broader experimental tool-set available to neuroscientists interested in the brain function or neurological diseases. Other alternatives to utilize the patch-walking algorithm could include the use of channelrhodopsin-assisted circuit mapping [115] to enable larger circuit mapping with multiple patch electrodes. In addition, patch-walking could be used for fluorescent-targeted cells where one pipette could target a specific subset of cells while the other pipette would probe non-targeted cells. A third alternative could be that one pipette patches a deep cell and stays patched onto it while pipette 2 continues to automatically patch other cells and search for connections in that manner. From these alternative uses of patch-walking, future work of automated multipatching could include optimization such that the first pipette patches the deepest cell first before the other pipettes patch cells above. Experiments could be done to probe specific layer to layer connections as well.

During validation experiments in brain slice, some pitfalls occurred with stability of the pipettes as some manipulators move while others are whole-cell recording from neurons. Steps were taken to mitigate this issue by stiffening the stage of the electrophysiology rig, dampening the manipulators, and slower movement of the manipulators.

Based on this promising pilot representation of patch-walking, we foresee that the patch-walking algorithm will enable multiple-pipette patch-clamp electrophysiology more accessible to a wider range of laboratories that usually conduct simultaneous recordings with a lesser number of manipulators. Further, the automated, dual-patching robot could also be altered to include users in the loop if they want to have control over certain aspects of the patching process or enable experienced patchers with digital pressure control. Even the best human electrophysiologists can only control one manipulator at a time, but the dual-patcherBot can control multiple manipulators, pressure lines, and command signals independently. The ability to patch clamp multiple cells simultaneously using the dual-patcherBot provides throughput improvements over manual patching, especially for those looking to utilize paired recordings in their experiments [116, 117, 118, 119].

CHAPTER 6

CONCLUSION

The study of the brain seems to be the final frontier of the human body to understand due to the immense challenges that still remain in the field. While a scientifically fruitful discipline, there are drastic deficiencies in our ability to systematically and efficiently study it whether it be on the molecular level or cross-regionally. The thesis presented here addresses a particularly challenging field of electrophysiology that aims to study as close to ground-truth data about an individual neuron. As the gold-standard technique for high spatiotemporal resolution study of neurons, patch clamping provides access to multi-dimensional data sets of electrophysiology, morphology, connectivity, plasticity, etc. In order to enhance experimental studies by labs around the world, the automated patch-clamp recording technology discussed here is particularly suited to address three major challenges in neuroscience discussed below.

The first challenge is high throughput pharmacological screening of compounds. Previously, screening multi-concentration point curves would require herculean efforts where a set of 100 data points would take several weeks. With the introduction of the patcher-Bot into the field of pharmacology, the reduction in human time requirement (13 hours of time to collect the same 100 data points) allows for significantly larger data sets collected in a shorter span of time. The inclusion of a millisecond fluid exchange handling with the robotic system along with a repeatable, precise physical manipulation (utility patent filed in April 2022) for solution exchange quickly improves the efficiency of ligand-gated ionotropic receptor experiments.

The second challenge is molecular screening for neuronal activity monitoring. Genetically encoded calcium indicators (GECIs) allow for simultaneous activity imaging of thousands, to, potentially, millions of neurons [69]. Similarly, genetically encoded voltage

indicators (GEVIs) are promising due to their ability for direct voltage transduction [81]. However, to date, no fluorescent sensor has been discovered that has single-spike resolution, fast response time and low photobleaching rate. However, the patcherBot showed its usefulness by enabling the discovery of Voltron2—a step in the right direction, and its effectiveness could continue towards other screening methods such as those considering directed evolution.

Integrating the patcherBot into an image- and electrophysiology-based multidimensional directed evolution platform could screen for new types of optogenetic tools. Highly innovative new tools could be discovered such as an infrared neural activator, a neural activator that cannot be driven by blue light, a two-photon neural silencing toolbox, a three-photon neural control suite, and an optimized light-gated potassium conductance. Screening of entire libraries of opsin variants with no human interaction, first through imaging, and then with select mutants further characterized with the patcherBot could have similar effects to that of the factory-like assembly for brain connectivity and function.

The third challenge is creating a single-cell map of neurons and connections in many parts of the brain [120]. Dysfunctions in cell-type specific connectivity are implicated in diseases such as autism [15], Alzheimer’s disease [52], and others. Discovering principles of inter-neuronal connectivity could begin to explain brain function (either in local circuitry or cross-regionally) as well as possible interventions for diseases. To do this, automated patch-clamp recording could become a platform or benchtop reader in an assembly line where technicians would set up slices to feed into the patcherBot which in turn could patch cells with minimal human supervision. Indeed, with the autonomous nature of the patcherBot, a single technician could operate multiple rigs at a time, increasing the experimental data sets collected. Standardizing data collection for electrophysiology is crucial for reducing variability for reproducibility and enabling large-scale studies.

6.1 Major Contributions

The major contributions of this work include algorithm development, as well as development and validation of techniques that are shown to be widely applicable in the neuroscience community. In this work, I:

- Validated the patcherBot, an integration of image-guided Autopatching and machine vision. The software package enables fully unattended, walk-away automation for patch clamp experiments.
- Enabled the extension of pipette cleaning to over 100 reuses for patch-clamp pipettes.
- Built and validated the first system to perform sequential patch clamp recordings automatically for pharmacological screening. Tested the system in adherent HEK-293 cells.
- Built and validated the first system to perform sequential patch clamp recordings automatically for genetically encoded voltage indicator screening. Tested the system in adherent HEK-293 cells and neuronal cultures.
- Designed and pioneered a pilot study for the first system to perform sequential patch clamp recordings automatically for opsin screening. Tested the system in transfected HEK-293 cells.
- Leveraged machine learning techniques to enable the first, fastest, and real-time automated neuron detection in brain slice under IR-DIC.
- Designed and validated the first automated, multi-pipette patch clamping robot to sequentially profile inter-neuronal connectivity using an algorithm for coordinated route-planning to enable high-throughput synaptic connectivity studies.

6.2 Future Work

The patcherBot, in its integration into many fields of neuroscience, has expanded its functionality towards pharmacology and opsin screening to machine learning developments and local brain circuit electrophysiology. Future work for the patcherBot can undergo several other hardware and software revisions to expand functionality.

The pipette cleaning technique, while shown to be transformative, can be improved and applied towards better pipettes. The effective cleaning and reuse (> 20 cleans) of pipettes has enabled higher quality pipettes, such as quartz, to be used. Unlike borosilicate, quartz has a lower dielectric effect and enables low-noise recordings which is especially important for very demanding recordings of single-ion channel [1].

While I have extended the capabilities of automated patch clamping towards studying local synaptic connectivity and screening for multiple-types of assays, the automated method can be further enhanced and modified to enable the the throughput of various other experiments.

First, the automated patch clamping software could be augmented to include the additional capability to perform patchSeq [121], enabling the collection of gene expression information from single cells. This would require hardware and software modifications such that the chambers of the sample dish would be RNase-free and programmed so that manipulators deposit the cell contents into designated wells. Cross-contamination would be of great concern and would require an additional cleaning step for genomic removal.

Second, the software could be coupled with optogenetics [44] to perform circuit discovery experiments similar to Channelrodopsin-2-assisted circuit mapping (CRACM) [115]. In such an experiment, a pipette would patch clamp a cell and then targeted presynaptic cells would be optogenetically stimulated to produce post-synaptic potentials (PSPs) on neighboring cells. The cell that produces PSPs on the patched cell would be patched with another pipette, and the process repeated again, until a connected network is traced.

Third, the robot could be applied specifically towards a neurological disease study. Specific neuronal types such as PV-int are highly vulnerable to stressors and have been implicated in many psychiatric diseases like autism and Alzheimer's disease [50]. The deployment of the patch-walking algorithm to profile local circuitry of a region of the mouse brain or for studying the effects of PV-int stressors may lead to understanding the pathologies towards Alzheimer's disease.

Appendices

APPENDIX A

PHARMABOT MANUAL

A.1 patcherBot_{Pharma} - Manual and SOP

A.1.1 Important Considerations

The following protocol to set up a patcherBot_{Pharma} robot is intended for an inverted microscope. A major component that should be mentioned is the digital pressure control box. This is important in conducting the patch clamp experimental steps and reuse of the pipette after each attempt. The majority of the components (e.g. microscope, vibration isolation table, computer, faraday cage, etc.) are generally widely available in a patch clamp electrophysiology lab. Particular components are also required (manipulators) due to their ease in communication with the Labview software. Not all versions of the available manipulators, amplifiers, valves, etc are coded in the present patcherBot_{Pharma} code but most can be programmed into LabView.

During patcherBot_{Pharma} operation, please note that while automated, specific items should be monitored (noted in step E.3).

Components

Microscope: Axiovert 200 Vibration Isolation Table Faraday Cage Computer: Suggested Minimum Requirements: 32 GB RAM, i7-8700K CPU @3.70GHz, Additional GPU Amplifier: Multiclamp 700B Motorized Stage: Scientifica Motorized Stage

Setting up the patcherBot Manufacture cleaning dish according to microscope stage dimensions in-house or using an on-demand production service (e.g., Protolabs, Neuromatic

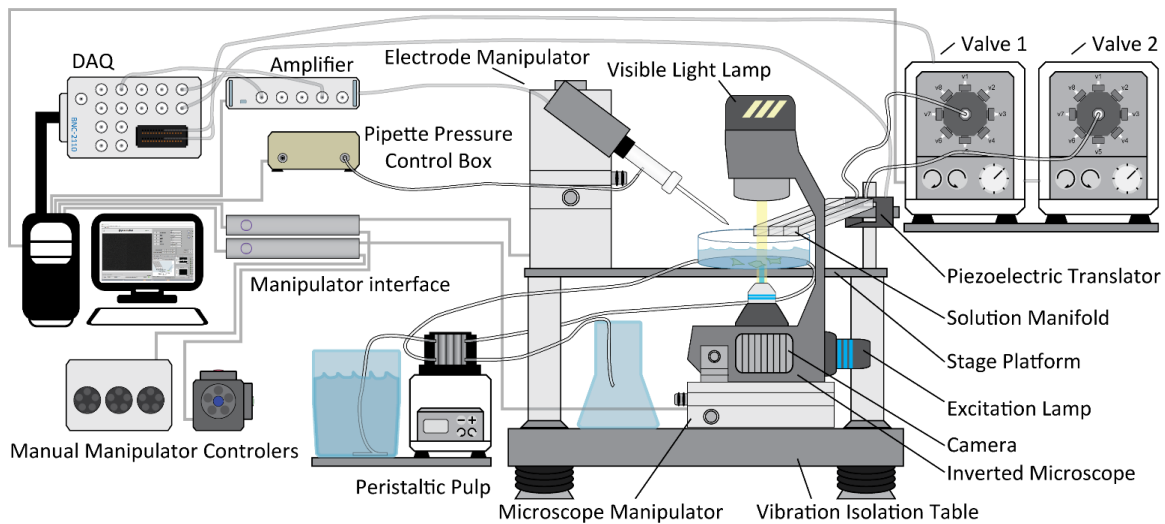


Figure A.1: Cartoon Representation of the patcherBot_{Pharma}



Figure A.2: Camera: QImaging Retiga Electro

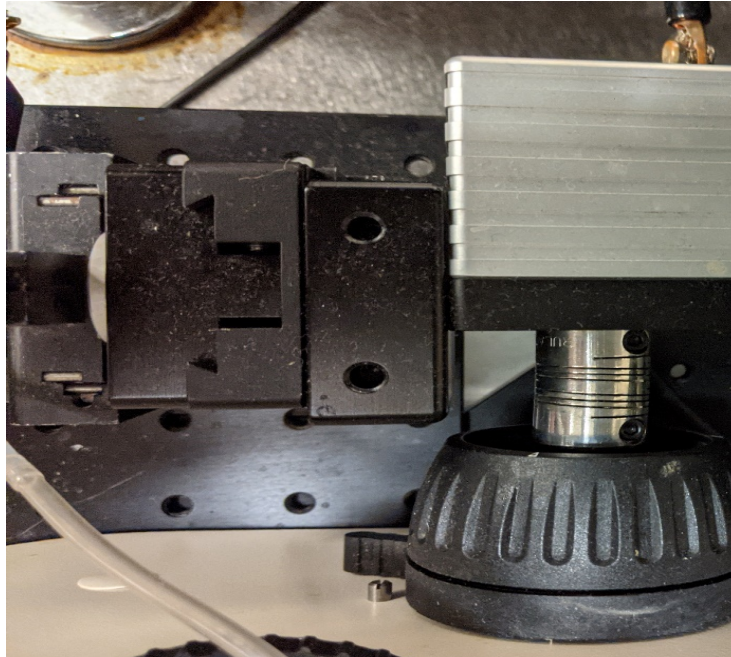
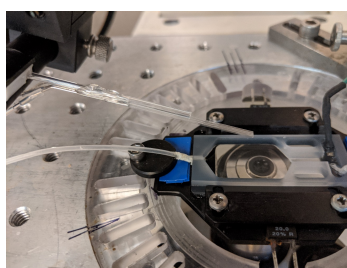
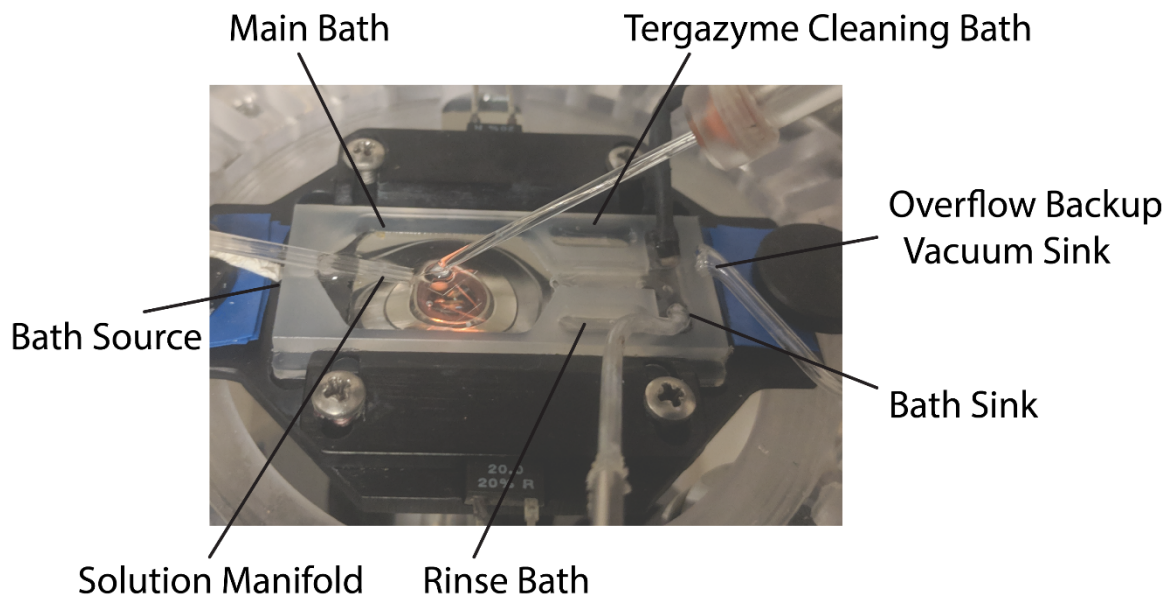


Figure A.3: Z-focus Module



Figure A.4: Elevated Microscope Platform. This is a custom milled sheet of aluminum.



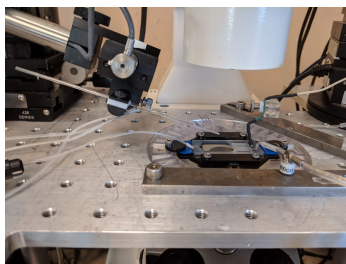


Figure A.8: Piezoelectric translator.



Figure A.9: Peristaltic pump.

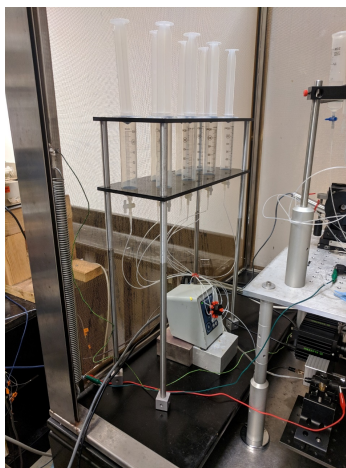


Figure A.10: Solution valves.

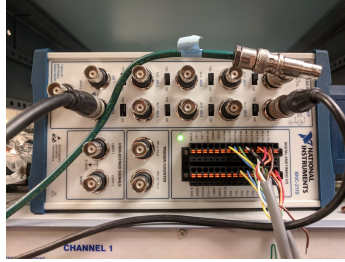


Figure A.11: DAQ.

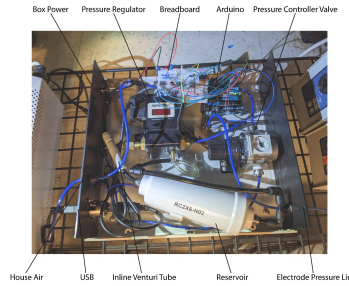


Figure A.12: Pressure Control Box (custom version). A comparable pressure control box can be built from scratch according to plans presented by [26]. Schematics, instructions, and parts lists are also available for download on autopatcher.org. Alternatively, a compatible pressure control box can be purchased directly from Neuromatic Devices (neuromaticdevices.com)

Devices). Note: .STL files for the depicted chamber is posted on Github.

Install pressure control box on existing patch clamp electrophysiology rig. Download and install software from Github. Perform initial software setup. The QImaging Retiga Electro requires additional registration (<http://www.rcubedsw.com/sitk-with-labview.html>). All components software and drivers need to be installed. Register manipulator and pressure control box according to manufacturer and COM port.

Panel Interface Components

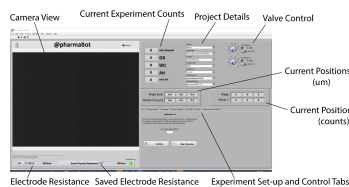


Figure A.13: Main VI Left Panel.

Here listed is an overview of most of the options and setting available to enable human assisted and fully automated patcherBot_{Pharma} operation.

Camera View This is the live view of the Camera, Setting can be found on the right panel **Display Tab**.

Current Experiment Counts This shows the number of cells selected as well as the number of attempts (Att). Out of those attempts, it also shows the number of gigaseals (GS) and whole cells (WC) achieved as well as the number of cells remaining.

Project Details Designated organization of metadata for the current experiment. This information is written to the file named “pharmaBotLedgerSeeds.txt” in each experiment folder.

Valve Control Controls available for assigning the valve of choice for experiment. These are controllable while setting up the patcherBot_{Pharma}. Set the dial to the valve of choice, then click go for the signal to be sent. The lamp will go on while moving and the indicator will then update after the valve terminates its motion. Note: the valve control does not ping the valve regularly, meaning that if you manually control the valve, the Labview code will not know the present selected valve.

Current Positions (m) Current position of the manipulator and stage (in microns). This is a relative number calibrated to the zero designated at the beginning of the calibration stage.

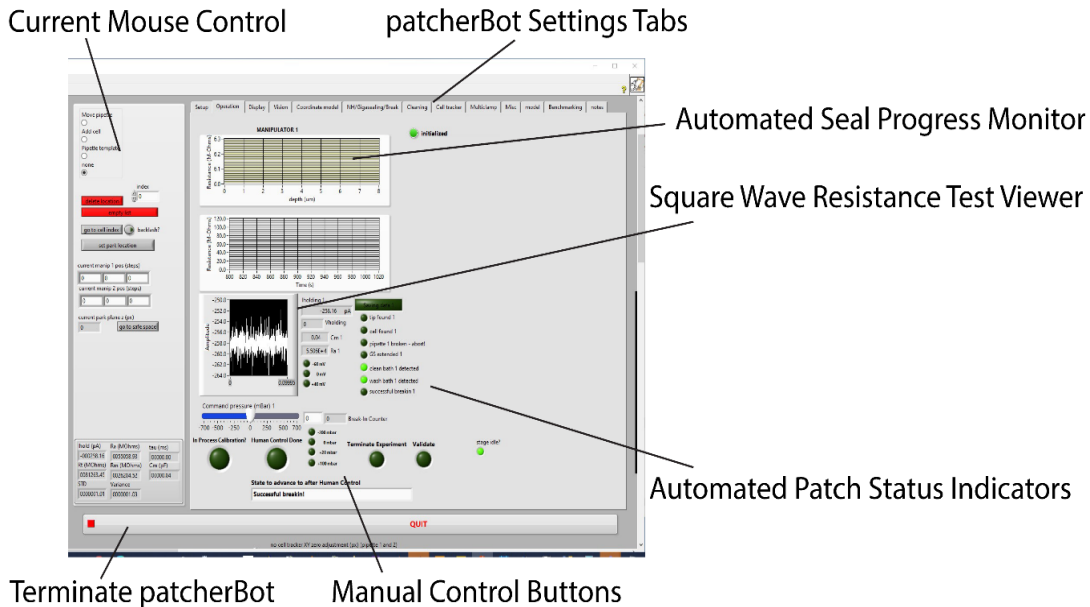
Current Positions (counts) Same as e) except the position is denoted in “counts” where 10 counts = 1 m.

Electrode Resistance Resistance of the pipette electrode.

Saved Electrode Resistance Saved resistance of the pipette electrode prior to an experiment. Click the lamp next to the indicator at after installing a new pipette, this saves the naïve resistance. After patching takes place, the in-bath resistance can be compared as an indication if the pipette cleaning process was successful.

Experiment Set-up and Control Tabs Setup tabs to help with experiment design and robot calibration. This where most of the user interaction occurs during set-up.

Main VI Right Panel



Current Mouse Control Indicates the role of a left mouse click on the live image of the camera: move pipette, add cell, pipette template, or none. Based on which Left Panel: Set-up and Control Tab is selected the result of left mouse click changes. For “add cell” the third (wheel) mouse button translates the stage to the location that was clicked.

patcherBot Settings Tabs Settings tabs for tuning patch clamp parameters. The following sections explain the features of these panels.

Automated Seal Progress Monitor Real-time pipette monitoring during automated cell approach and sealing.

Square Wave Resistance Test Viewer Real-time feedback of pipette electrode square wave seal test, resistance measurement from this is used for automated cell approach and sealing.

Automated Patch Status Indicator Lamp indicators that show if automated patch clamp steps of the robot have been completed.

Terminate patcherBot Lamp Stop button to end the software controlling patcherBot.

Manual Control Buttons Lamp buttons that can be toggled to allow human operator control over patch clamp steps.

“**Validate**”, if clicked at the end of a set of recordings the patcherBot will validate any solution jump positions (piezo or manipulator jumps; the solution valve will be changed to the 8th valve and any jumps will be repeated).

In short, the patcherBot will remove the cell with high positive pressure. The values are programmed to switch to the 8th position. After solution priming, all the jumps (piezo or manipulator) will be repeated and the open tip current response is recorded. (note: the solutions in the 8th position must produce a salt concentration differential to produce a sufficient change in junction potential to detect readily).

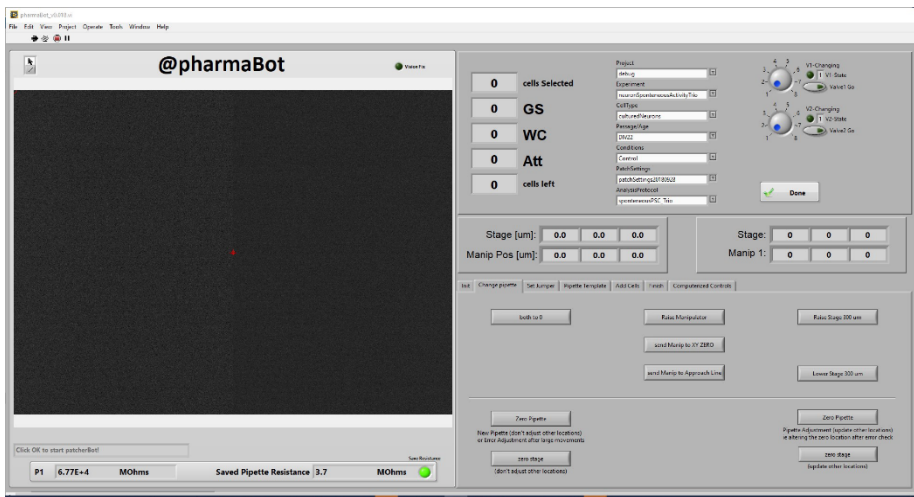
“**Human Control Done**”, this lamp button is used when the patcherBot enters the “human positioning. . .” state, when clicked the patcherBot will continue to the state that is selected in the “state to advance to after human positioning” drop down box. The patcherBot state the user selects should be limited to “detecting cell” if the user corrects the pipette location to a position directly over the cell, “cell detected” if the user places the pipette on to the cell, “gigaseal established” if the user places the electrode on the cell and forms a

gigaseal with manual pressure control, “Successful breakin” if the user achieves the whole cell conformation manually, “unsuccessful breakin” if at any point in the patching process there is an issue which tells the patcherBot to move on to the next cell. (The “whole cell recording” state can also be used, if the cells patched generally are leaky, perhaps due to gap junctions with neighboring cells, and this is not going to cause issues with the experimental protocols. For instance, in pulling a patch, the break-in resistance may be low, but may improve when the patch is removed from the rest of the cell.)

“**Command Pressure Slider**” and “**Fixed Pressure Level Lamp Buttons**”, these allow the user to select and send commands to the pressure box to apply to the pipette.

“**In Process Calibration**”, click this lamp to have the patcherBot pause before starting the next cell iteration. The pipette can be replaced or the solution manifold locations can be checked or updated. To continue the patcherBot process, unclick the “In Process Calibration” lamp button.

Left Panel: Change Pipette Tab



Changing Pipette Comands

These are generally the most useful commands when setting up the patcherBot, learning to use these will speed up new pipette loading and general use of the patcherBot.

Both to 0 Brings pipette and stage to the set (0,0,0) position in (x,y,z). Note, this command is typically not safe when a new pipette is loaded as variation in pipette pulling usually means that pipette are all not the same length.

Raise Manipulator Brings the manipulator up 1 mm in z-direction.

Send Manip to XY Zero Brings the manipulator to the zeros of the x,y-locations. This option is typically the safest way to bring a new pipette into the area of the zero stage location, then dropping the pipette down to the plane of the stage Zero usually allows one to locate a shadow of the pipette on descent, and then allows for quick manipulation of the new tip to the zero location and zeroing of the manipulator coordinates.

Send Manip to Approach Line Brings the manipulator into the experimental bath axially (removed 300 m tip to zero along the axis of the manipulator). This can cause some issue when replacing the electrode, as pulled electrodes typically have a slight asymmetry and so as the electrode is moved along the manipulator axis they may be out of the camera field of view and the user may have difficulties in zeroing the pipette.

Raise/Lower Stage 300 um Raises or lowers the stage in z-direction by 300 m.

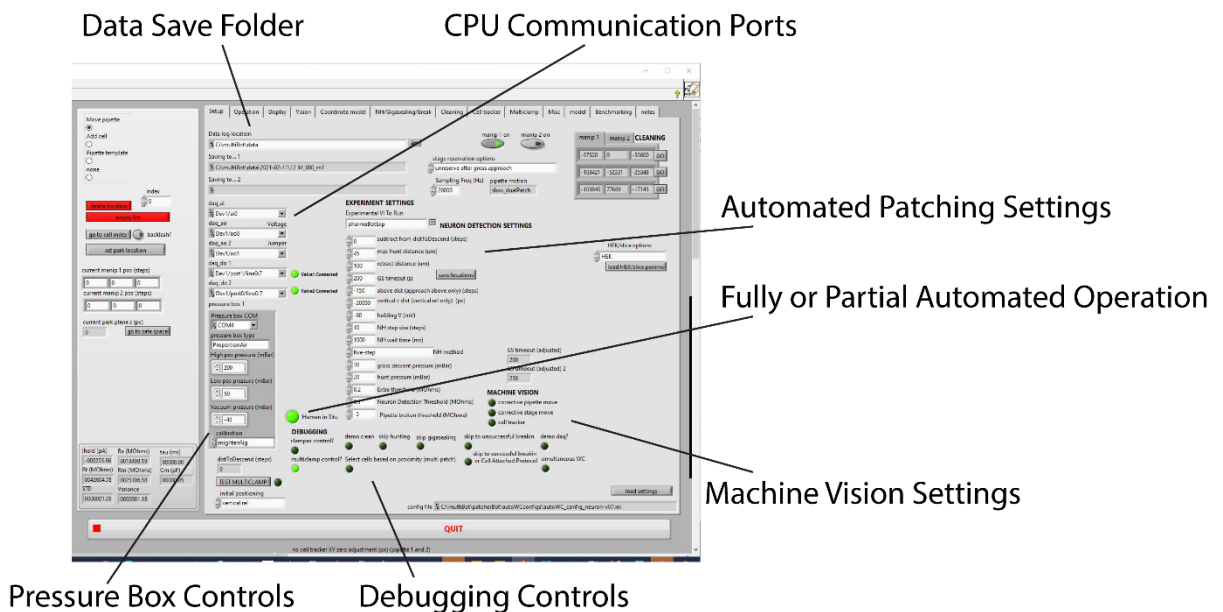
Zero Pipette (left, new Pipette) Set the current position of the pipette to zero (if new pipette). This does not update any other locations. If you are unsure which Zero Pipette to click, click this one.

Zero Stage (left) Set the current position of the stage to zero (if starting new experiment). This does not update any other locations. If you are unsure which Zero Stage to click, click this one.

Zero Pipette (right) Set the current position of the pipette to zero. This button will zero the pipette coordinates, and update all other locations (cleaning/wash baths and solution manifold locations). Use this only if you have a previously zeroed pair of pipette/stage and you are updating the zero location.

Zero Stage (right) Set the current position of the stage to zero. This button will zero the pipette coordinates, and update all other locations (cleaning/wash baths and solution manifold locations). Use this only if you have a previously zeroed pair of pipette/stage and you are updating the zero location.

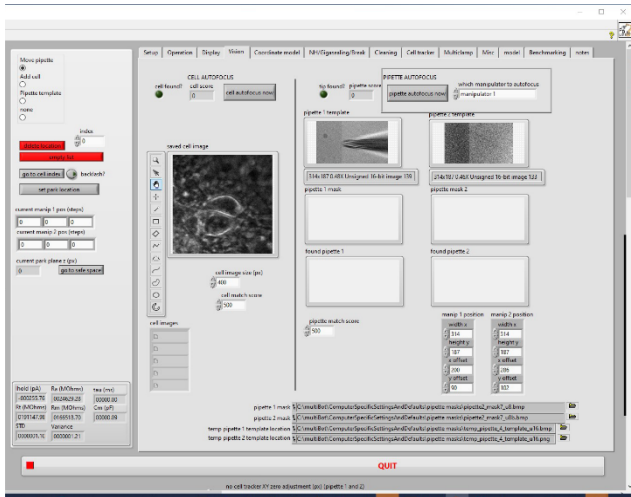
Setup Tab Panel



Data Save Folder Designated folder where data will be saved.

CPU Communication Ports Communication ports for controlling the DAQ. The DAQ connects to the amplifier (input current/voltage, output voltage/current), the piezo-translator control box, and the serially controlled solution valves.

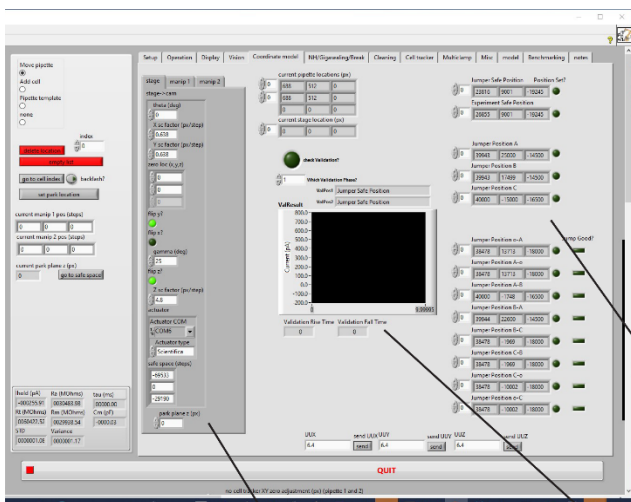
Automated Patch Settings Automated patch clamp parameters.



Computer Vision

Computer Vision This tab shows the image of a selected cell as well as the pipette image and templates for pipette detection.

Coordinate System Tab Panel



Coordinate System Settings

Manipulator Coordinate Parameters Past Validation Run Viewer

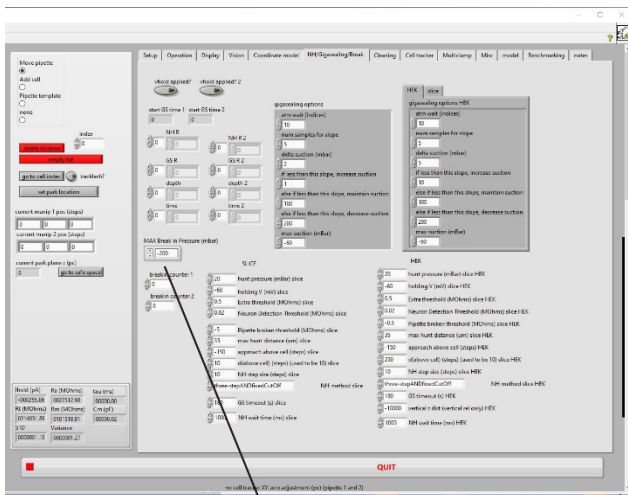
Solution Manifold Locations

Solution Manifold Locations Designated locations of the solution manifold. The Lamp indicators show if the location has been updated since the labview code has been in operation.

Past Validation Run Viewer The “check Validation” lamp can be enabled to show the most recent position validation set that has been run. It is best to disable this while the patcherBot process is running, and only checking this while in “Human positioning”, “in Process Calibration”, or the default initialized state “Click OK to start patcherBot”.

Manipulator Coordinate Parameters Coordinate transform and communication settings for the manipulator. When building the patcherBot, these parameters need to be determined, in simple terms these are the cartesian parameters that orient the two manipulator settings to one another.

Extra Patching Settings Tab Panel



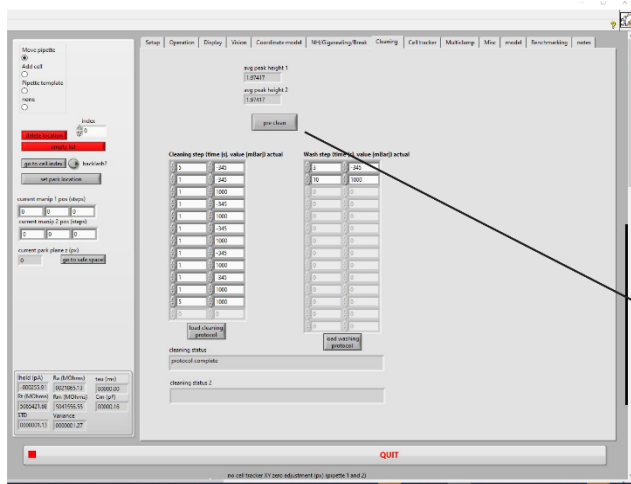
Extra Patching Settings

Max Break-in Pressure Setting

Max Break-in Pressure Setting Set the maximum pressure for break-in of cell.

The rest of the settings on this tab are backup/preset values, that can be loaded to the current setting on the operation tab. Two sets of cell finding/patching settings can be set and then swapped at will.

Pipette Cleaning Tab Panel



Pipette Cleaning Settings

Pre-Clean Button

Pre-Clean Button Toggle on or off if pre-cleaning of the pipette is desired. Pre-cleaning can be turned on when the labview process must be stopped in the middle of an iteration, before the cleaning steps, and allow you to clean the pipette as you restart but before attempting to patch the first cell.

The other settings are for the protocol control for cleaning the pipette, you shouldn't have to modify this.

Designing a patcherBot Experiment Protocol

Planning Your patcherBot Protocol There are many things to consider when designing your patcherBot Experiment Protocol.

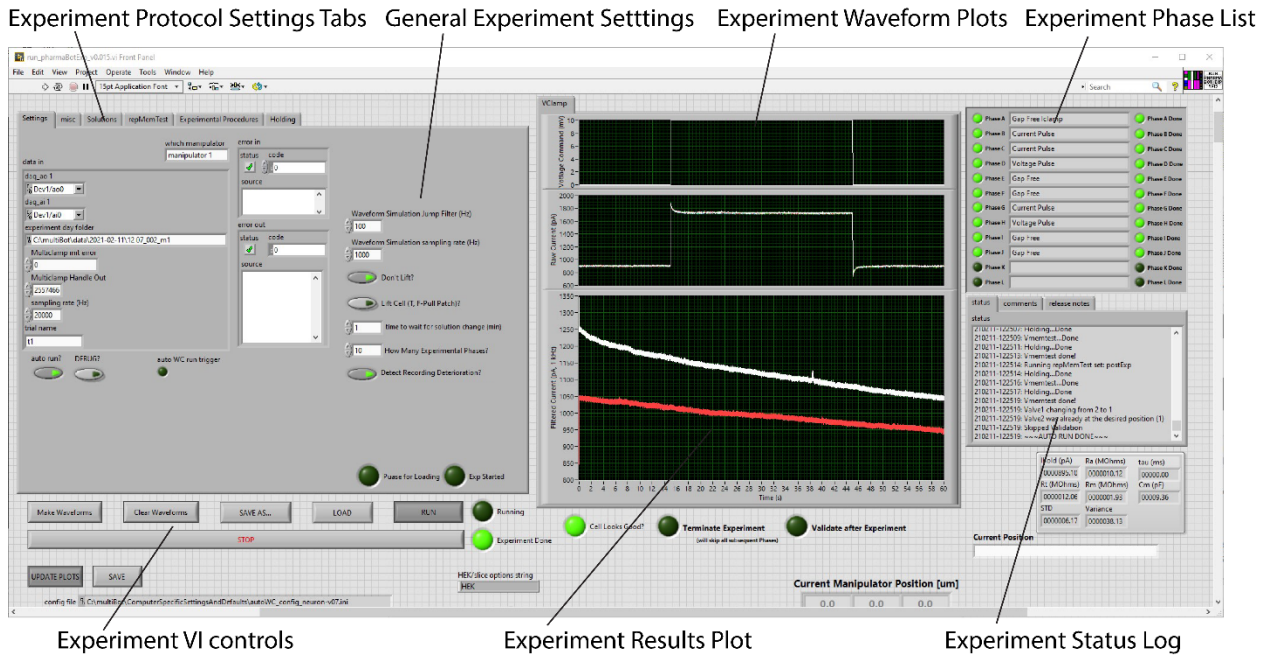
Fully automated or minimal user assistance

Adherent cell experiment, lifted cell, or excised patch

Then choosing your number of experimental phases and what specific types of protocol for each phase

As always transfection efficiency and cell health are important factors, so choosing the right number of cells to attempt to record from needs to be decided. We will revisit these topics, after showing the experiment protocol interface.

Whole-cell Recording Application (opens upon successful break-in into cell)



Experiment Protocol Settings Tabs

Find here the options to design and document your patcherBot protocol.

General Experiment Settings

Waveform Simulation Jump Filter – computational frequency to filter the square wave signal that is sent to the piezoelectric translator

Waveform Sampling Rate – Rate of data collection (also see setting box on the main VI, set both to the same rate)

Don't Lift button – Activate this button if you intend to do an experiment on adhered cells

Lift Cell (or Pull Patch) – Activate this option if you want to lift the entire cell; light suction will be applied after achieving whole cell and a spiral lifting trajectory should

result in lifting the cell off the coverslip. In order for high efficiency cell lifting, the cells should be plated on coverslips with a low concentration of cell adhering glass coating (PDL) and the selected cells should be isolated ideally. If the button is not activated, the patcherBot will attempt to pull a patch; the atmospheric pressure will be applied to the pipette and will be pulled back in a withdrawing arch. In order for high efficiency patch excising, the cells should be plated on coverslips with a normal (to high) concentration of cell adhering glass coating (PDL) and the selected cells should be in a patch of multiple cells to provide additional resistance to prevent cell detachment from the coverslip.

Time to wait for solution change – This should be determined empirically for each individual patcherBot. Ideally the exchange times for all valves are similar, and should simply be based on the length of tubing from the valve to the solution manifold (if the solution reservoir level, top of the solution's height above bath, and the tubing/manifold cross sections are also similar).

How many Experimental Phases – Select the number of experimental phases you wish to record in your experiment. Select 1-12 (corresponding to A-L) phases. The experiment VI must be running (not running an experiment) for the experiment phases to update, the selected number of experiment phase tabs will become active when as the input field is changed (use the arrows).

Detect Recording Deterioration – If this option is selected, after each phase if the leak current is $>1000\text{pA}$, a dialog box will pop up asking if the user wants to terminate experiment and move to the next iteration.

Experiment Waveform Plots

Signals being sent to the voltage control on the amplifier or the piezoelectric translator.

Experiment Phase List and Lamps

When an experiment is initiated, after cell patching, the lamps on the left will light up to indicate how many phases there will be in total, the fields will display which types of phases will be performed, and the right lamps will light up when each phase is completed.

Experiment Status Log

During the experiment, time stamped log of the patcherBot activities are recorded here and saved at the conclusion of the experiment (status.txt).

Experiment Results Plot

The current/voltage response of the patcherBot activities are displayed here. There is no live display, a sweep must be completed before it is displayed.

Experiment VI controls

Make Waveform – Calculate and display phase waveform previews (all previews live update when they are modified).

Clear Waveform – This clears the phase waveform previews to free up space.

Save As – Saves all experiment settings to an .ini file.

Load – Loads an .ini file to the experiment subVI, only files created from the same version can be loaded to prevent allocation errors.

Run – Starts the experiment according to the settings (during normal operation the patcherBot will auto start when the it activates the experiment subVI).

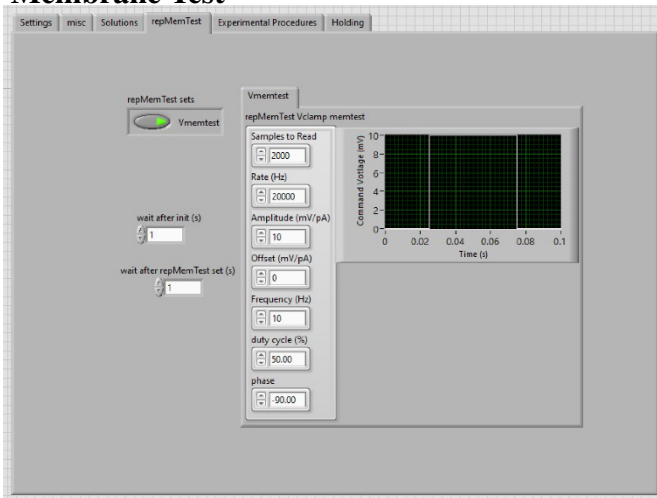
Solution Documentation

The screenshot shows a software interface for documenting solutions. It features three columns of input fields for solutions A, B, and C. Each column has eight rows labeled 'Solution1' through 'Solution8'. Below the input fields are three dropdown menus labeled 'Lane A Controlled by which valve?', 'Lane B Controlled by which valve?', and 'Lane C Controlled by which valve?'. A central diagram shows a three-lane microfluidic chip with 'Valve 1 (A)' and 'Valve 2 (C)' positioned above it. On the left side, there are three time-of-change fields: 'time of Last V1 Change' (8.771691), 'time of Last V2 Change' (0), and 'time of Last V3 Change' (0).

Solution Documentation

Here the solutions can be recorded, these fields are documented in a .txt file (experimentalHeader.txt).

Membrane Test

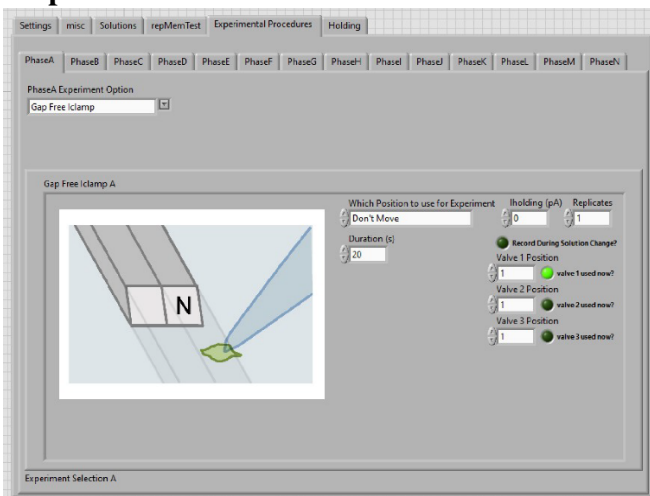


Membrane Test Settings

The set-

ting for the membrane test can be set here.

Experiment Procedures



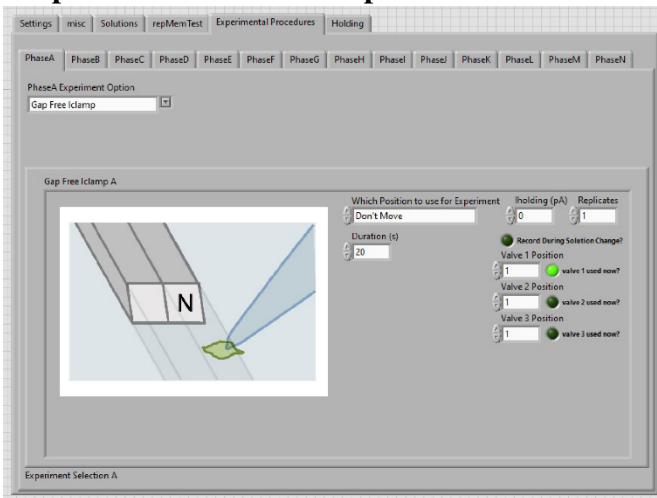
Experimental Procedures Tab

Ex-

perimental protocols are set here, there are 12 phases that can be programmed into a single experiment. The type of experiment for each phase is set by the dropdown box. The number of activated phases is set by the numerical field on the settings tab.

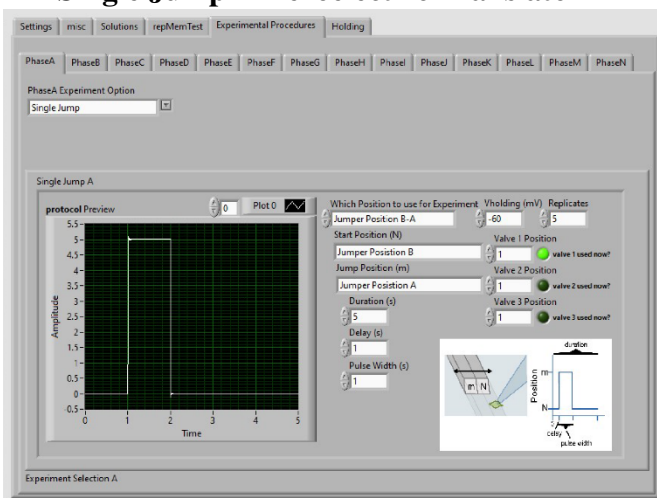
Experiment Paradigms The available experiment phase types are as follows, each has individual settings to set the parameters of the experiment. If the VI is running the preview will auto update so you can visually see the waveforms you are designing.

Gap Free – Current Clamp



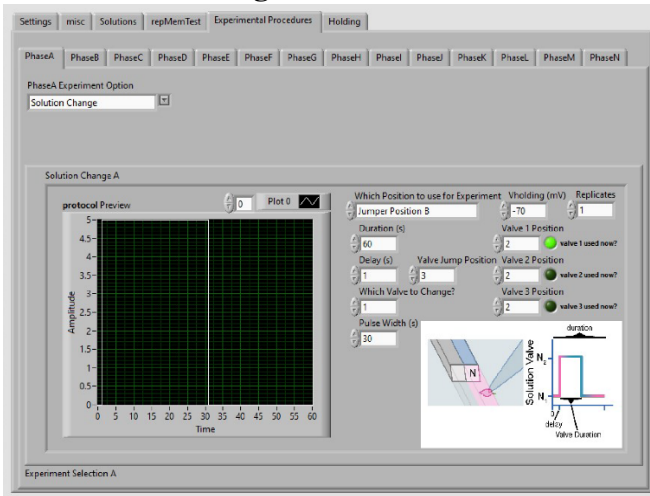
Gap Free (current clamp) Experiment

Single Jump – Piezoelectric Translator



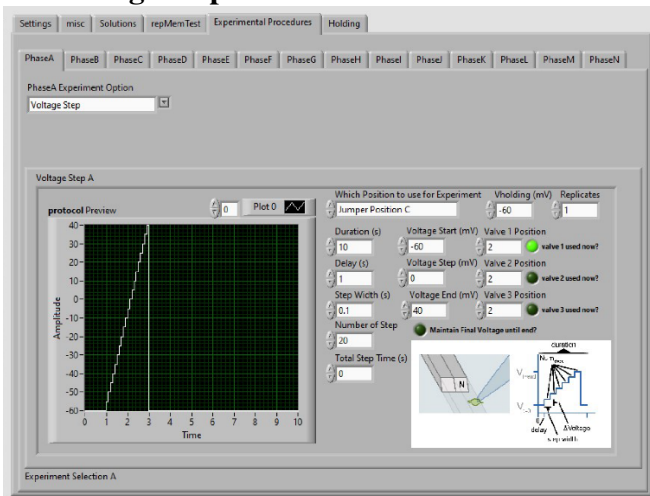
Single Jump (piezo) Experiment

Solution Change



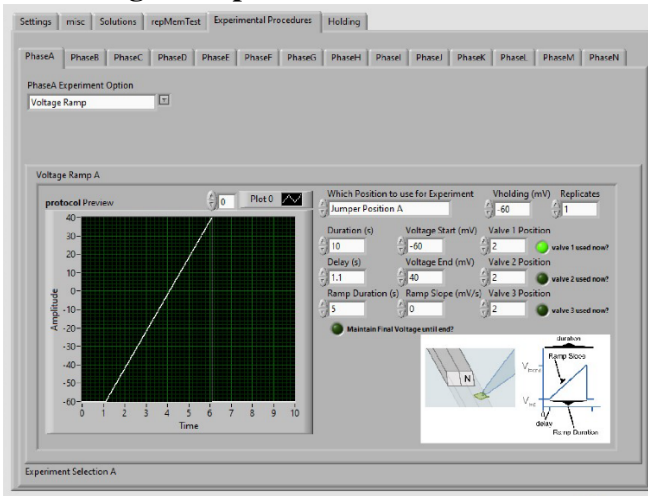
Solution Change Experiment

Voltage Step



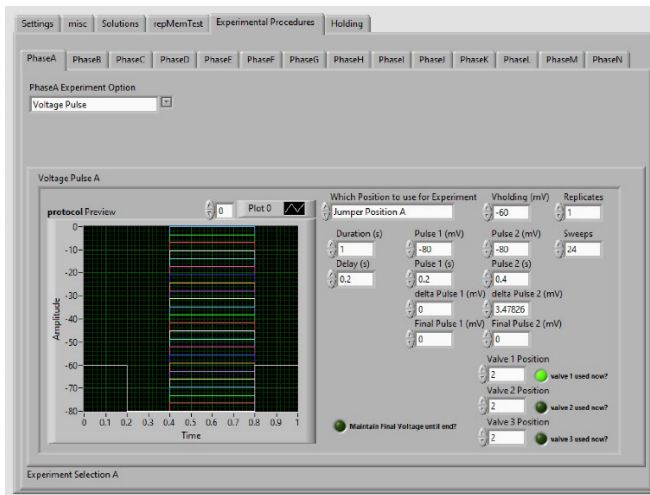
Voltage Step Experiment

Voltage Ramp



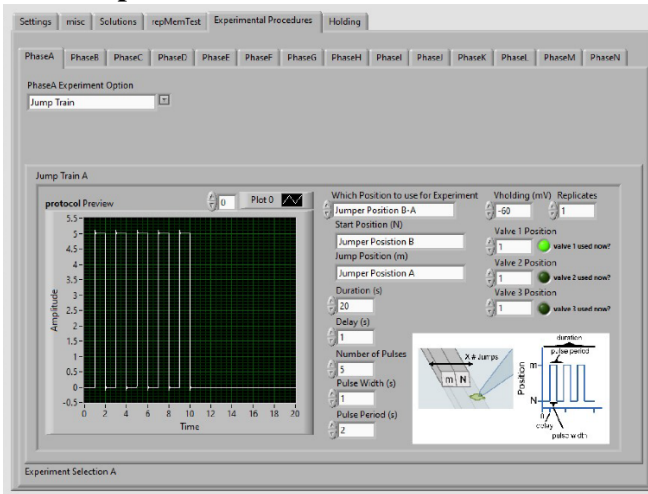
Voltage Ramp Experiment

Voltage Pulse



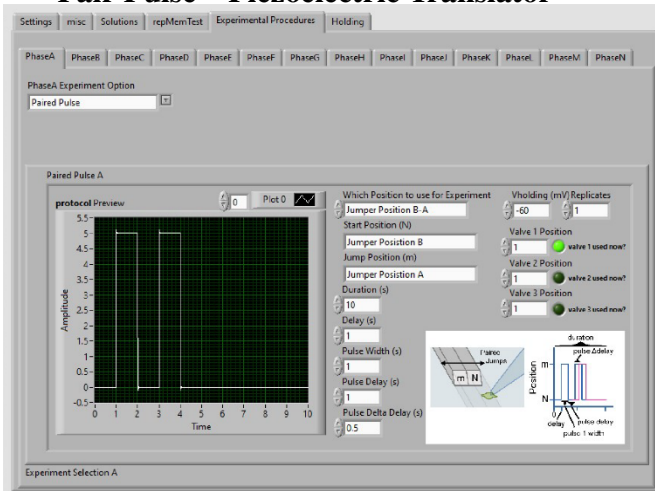
Voltage Pulse Experiment

Jump Train – Piezoelectric Translator



Jump Train (piezo) Experiment

Paired Pulse – Piezoelectric Translator



Paired Pulse (piezo) Experiment

Single Jump – Manipulator Jump

Settings misc Solutions rcpMenTest Experimental Procedures Holding

PhaseA PhaseB PhaseC PhaseD PhaseE PhaseF PhaseG PhaseH PhaseI PhaseJ PhaseK PhaseL PhaseM PhaseN

PhaseA Experiment Option
Single Manip Jump

Single Manip Jump A

protocol Preview Plot 0

Amp (uA) vs Time (s) graph showing a step function from 0 to 2 uA at t=0.

Start Position (N) Jumper Position B: -60 mV Replicates: 10
 Jumper Position A: 2 m Valve 1 Position: valve 1 used now?
 Duration (s): 8 Valve 2 Position: valve 2 used now?
 Delay (s): 0.5 Pulse Width (s): 1 Valve 3 Position: valve 3 used now?

Experiment Selection A

Single Jump (Manip) Experiment

Gap Free - Voltage Clamp

Settings misc Solutions rcpMenTest Experimental Procedures Holding

PhaseA PhaseB PhaseC PhaseD PhaseE PhaseF PhaseG PhaseH PhaseI PhaseJ PhaseK PhaseL PhaseM PhaseN

PhaseA Experiment Option
Gap Free

Gap Free A

Which Position to use for Experiment
Jumper Position A: 40 mV Replicates: 3

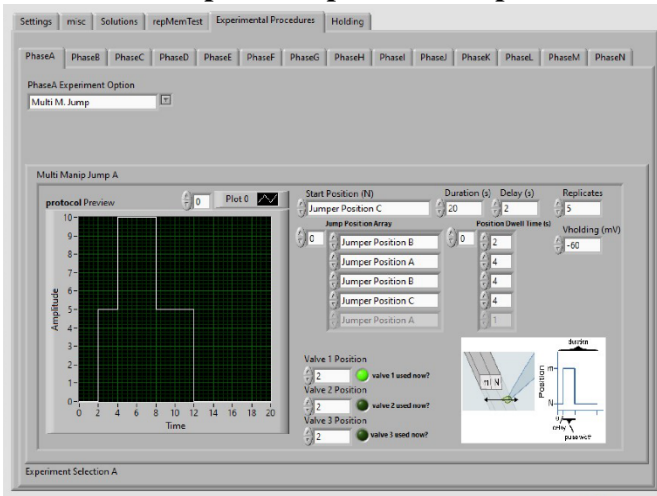
Duration (s): 60 Record During Transition Change

Valve 1 Position: valve 1 used now?
 Valve 2 Position: valve 2 used now?
 Valve 3 Position: valve 3 used now?

Experiment Selection A

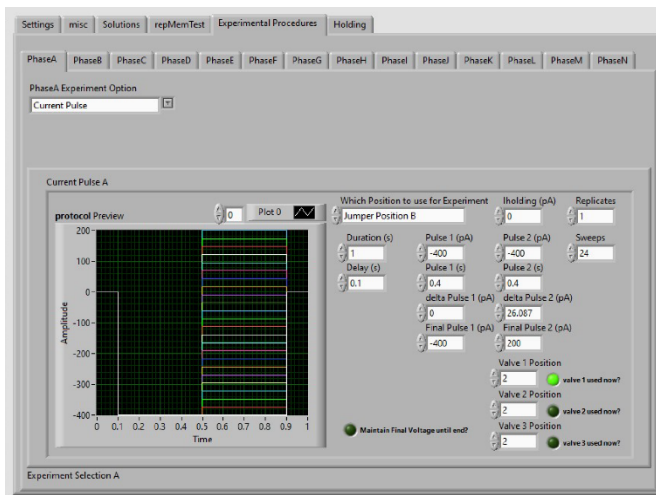
Gap Free (voltage clamp) Experiment

Multi-Jump – Manipulator Jump



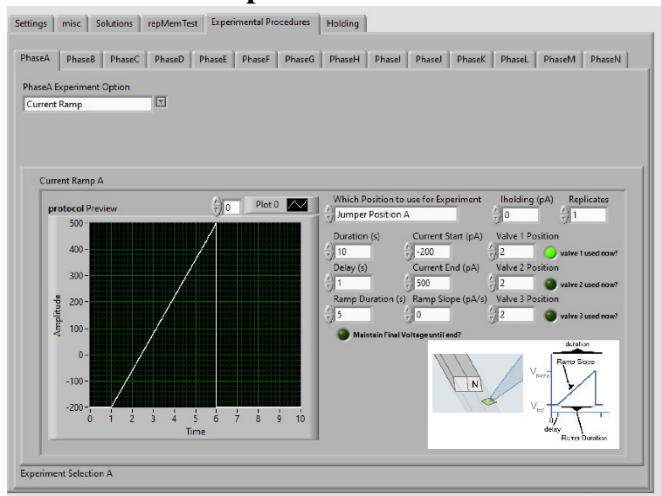
Multi-Manipulator Jump Experiment

Current Pulse



Current Pulse Experiment

Current Ramp



Current Ramp Experiment

A.1.2 Before each experiment:

Preparation of the patcherBot_{Pharma}

Prepare electrophysiology rig for patch clamp experiment. Prepare 2% w/v Tergazyme cleaning solution in room temperature distilled water.

Mix solution until all Tergazyme powder is dissolved.

Note: Because Tergazyme is an enzymatic detergent, the enzymatic component degrades over time. The manufacturer recommends making fresh solutions and using them within 8 hours for maximum efficacy.

Using a syringe with a 0.2 μm filter and 23G needle, fill the appropriate bath reservoir with freshly made 2% w/v Tergazyme (or extracellular solution for rinsing).

Be careful to not overfill the cleaning bath reservoir, as this can cause Tergazyme solution to flow into the experimental chamber, potentially damaging cells. The Tergazyme solution has very low surface tension so it will run even with the smallest amount of overfilling. Also account for the amount of displacement the submerged the pipette will cause.

Fill pipette electrode with intracellular solution and load into headstage of manipulator.

Prepare biological sample and place into sample dish of patcherBot_{Pharma}.

Load experiment settings for patcherBot_{Pharma}. After opening the main patcherBot VI, the experiment subVI can be opened. Run the main VI to initialize the ports, then stop the VI. Go to the experiment subVI, unclick “auto run” button and click the “auto WC run trigger” lamp button. Run the subVI, then load an experiment .ini or program your desired experimental protocols.

Starting a patch clamp experiment

Initialization Protocol

Calibrate the pipette electrode This details the initialization protocol in full, to be performed the first time. Following these detailed steps there will be a recap of a briefer initialization protocol that can be performed if you ensure the placement of the manipulators, bath, solution manifold, etc do not move between use.

Start initialization, press the calibrate button. Use Manipulator 1, then press the “done” button (not shown).

First, select a stage z-plane position 300 μm above the cells. Select and save this as the “home” position above a target cell. Press the “done” button.

Bring the pipette into the field of view under the microscope, and then lower the pipette to the “home” plane set in the previous step and bring it to the middle of the view. Press the “Pipette in focus” button. “Zero” the pipette tip at this location with the “zero pipette” button. Press the “done” button.

Move the pipette to a position outside of experimental bath without risk of collision with other hardware and push the save “safe” position button. Press the “done” button.

Move the pipette to a position above the bath where the pipette can translate side ways without crashing into the bath chamber and push the save “above bath” position button. Press the “done” button.

Move the pipette and submerge it in the cleaning bath (this is the lowest position that the patcherBot will search to find the pipette solution) and push the save “cleaning bath” position button. Press the “done” button. Upon pushing done, the patcherBot will move, according to the parameters field on this tab, and if appropriately programmed it should move straight up and then sideways to a position over the wash bath.

Move the pipette and submerge it in the wash bath (this is the lowest position that the patcherBot will search to find the pipette solution) and push the save “cleaning bath” position button. Press the “done” button. Upon pushing done, the patcherBot will move, straight up and then sideways to the safe location.

Bring the pipette back to the “home” position (“both to 0” button).

Save the pipette template, for pipette finding during the actual experiment, click the video feed to save an image, the mouse click designates the XYZ coordinates of the pipette tip.

The solution manifold positions can be programmed/confirmed now (see below).

The next step is to click the cells to queue for serially patching. Left mouse button selects the cell, an image is taken to compare/calibrate during fully automated use. The third (wheel) button translates the stage where the click occurs. It is best to click/select the each cell when the cells are near the center of the field of view.

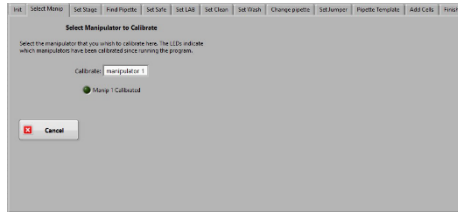
If the solution manifold positions have already been set the patcherBot recording process can be started with the “begin patch”.

Starting patcherBot_{Pharma} Initialization



Start

Select Manipulator



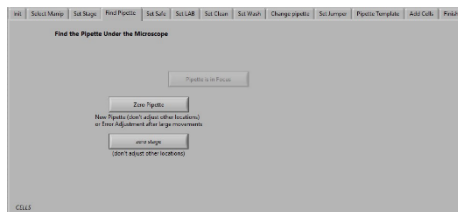
Step 1

Zero Stage



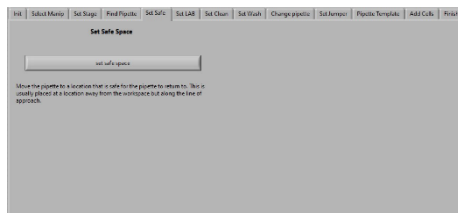
Step 2

Zero Manipulator



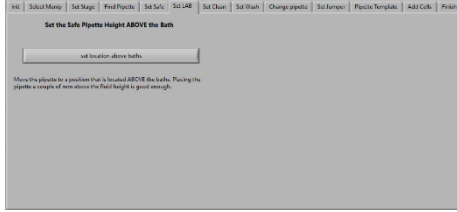
Step 3

Set Safe Plane



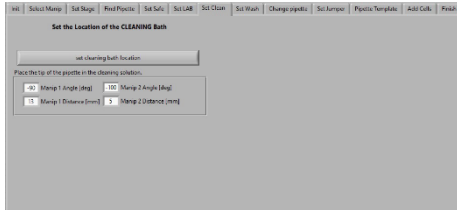
Step 4

Set Bath Clearance Plane



Step 5

Set Cleaning Bath Location



Step 6

Set Wash Bath Location



Step 7

Set Pipette Template Image



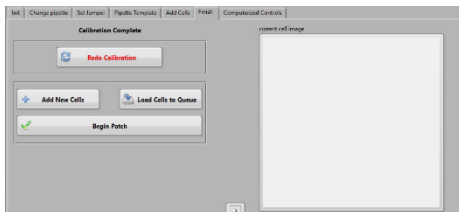
Step 8

Add Cells for Patching



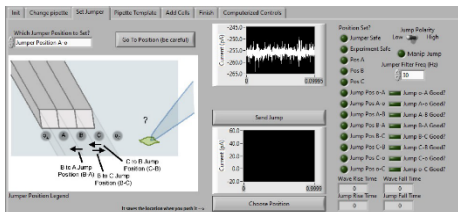
Step 9

Start patcherBot_{Pharma} Run



Step 10

Set Solution Manifold Locations



Solution Manifold Locations

There are several func-

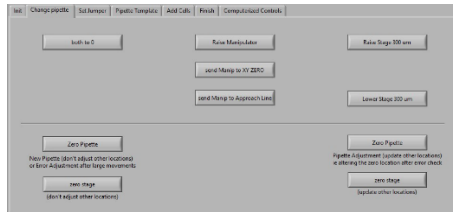
tions that this tab has. The buttons in the top left can be used to send the manipulator to previously saved positions. The dropdown box allows you to select a location and the “go” button sends the pipette to this location. The dropdown box also is used to save the current pipette location to the saved location array when the “choose position” button is pushed. The “send jump” button sends a square wave pulse (filtered based on the filter frequency field on the tab, and the direction is set by the jump polarity) to the piezoelectric translator. If the pipette is appropriately placed at a solution interface, the solutions flowing on either side of the interface have different salt concentration so that a junction potential differential results in a current step response then the jump rise and fall times will be measured (20-80 time).

Labview Panel Manipulator Controls



Labview Manipulator Controls

Change Pipette Control Panel



Change Pipette

During the experiment – fully automated

patcherBot_{Pharma} will now attempt to patch each cell in the queue and if whole-cell recording is achieved, then the patcherBot_{Pharma} protocol designated will be conducted. During each iteration the patcherBot moves to the XY location above the next cell, the pipette is translated to the same location. The patcherBot will attempt to verify the pipette tip location, using a cross-correlation protocol using the pipette template as a reference, the pipette will move up and down (15 μm), the best fit is found and the pipette location is updated. The patcherBot then focuses down to the next selected cell. A similar protocol (as with the pipette tip finding) is used with the cell to confirm its location. The pipette is then brought down to a position just over the cell, then the cell hunting process starts. The pipette steps down one increment, the resistance is checked, and this repeats (to a set maximum). If the resistance crosses the detection limit, then the cells will attempt to patch the cell, the cell sealing protocol then starts. Suction is applied at increasing amounts based on if the patch is stalling or waits if the patch is actively occurring. If a gigaseal is established, then the patcherBot will then move to break-in. High suction is applied in short bursts, the patcherBot monitors for the capacitance of the electrode to increase, signifying

that break-in was successful. If the resistance is still high, the patcherBot will move into the experimental execution protocols, otherwise the pipette will be removed (high positive pressure is applied and the pipette is retracted) and cleaned for the next iteration.

Follow along the various event states of patcherBot_{Pharma} or grab a cup of coffee.

During the experiment – semi-automated

patcherBot_{Pharma} will now attempt proceed to each cell in the queue and wait for the operator to perform some parts of the process then will proceed to whole-cell recording if successful, then the patcherBot_{Pharma} protocol designated will be conducted.

During each iteration the patcherBot moves to the XY location 100 m above the next cell, the pipette is translated to the same location. The patcherBot then focuses down to the next selected cell. The pipette is then brought down to a position just over the cell, then pauses for operator intervention. The user can do all of these steps, or just set of the initial steps; land the pipette on the cell, form a gigaseal, break in/enter whole cell conformation, and pull a patch/lift the cell. After the operator has performed the patching tasks that they wish, they can turn control back over to the patcherBot. The rest of the operations will be performed, as described above. Notification sounds occur throughout the patcherBot operation so that the operator can be away from the patcherBot but know when to check back in for the next operator intervention. Follow along the various event states of patcherBot_{Pharma} or grab a cup of coffee.

Notes to consider during experiment: Monitor patcherBot_{Pharma} operation for changes in fluid levels of the bath reservoirs, decreases in yield, pipette clogs or breaks, and other potential sources of failure. If pipette appears to be clogged (i.e., visible internal clog observed in pipette tip or increase in resistance) or broken (i.e., visible broken tip or decrease in resistance), then replace the pipette and repeat calibration.

Ensure there is no fluid exchange between the cleaning bath and the experimental bath. When the tip of the pipette is in the cleaning bath, monitor the square wave pulse in voltage clamp. If there is no electrical contact between the ungrounded cleaning bath and the grounded experimental bath, you will see capacitive transients, similar to when the tip of the pipette is in air. If there is electrical contact, you will see a square wave pulse, similar to when the tip is submerged in the experimental bath. To resolve this, use a kimwipe to remove small amount of fluid from the cleaning bath until electrical contact is eliminated.

Cleaning up

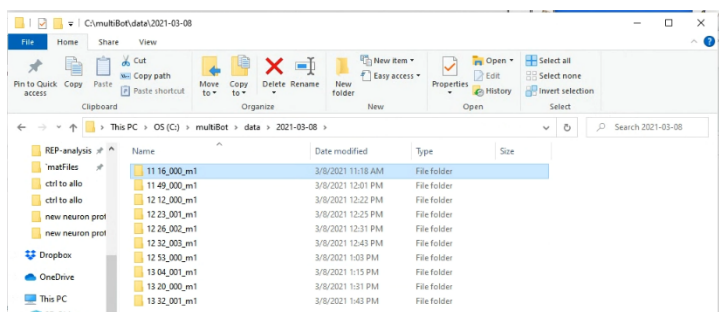
Stop the patcherBot_{Pharma} software.

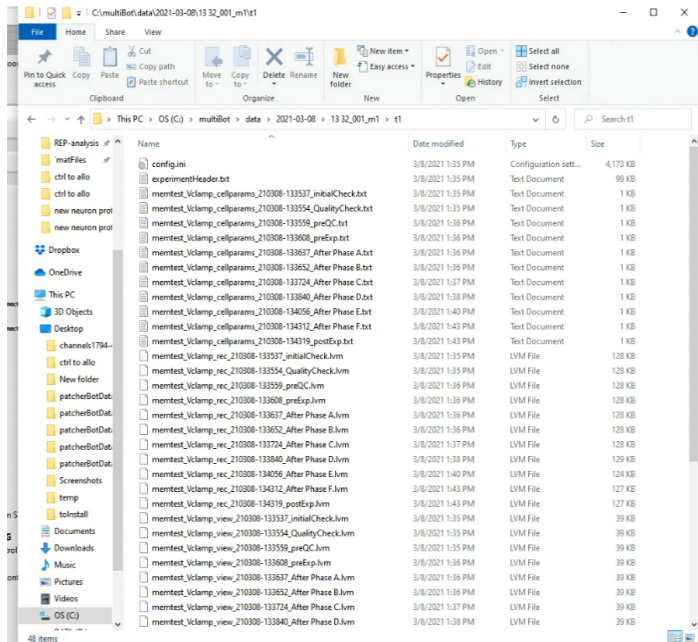
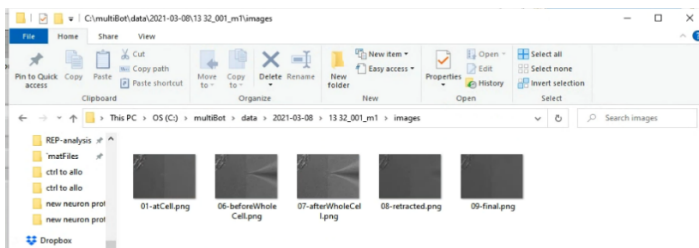
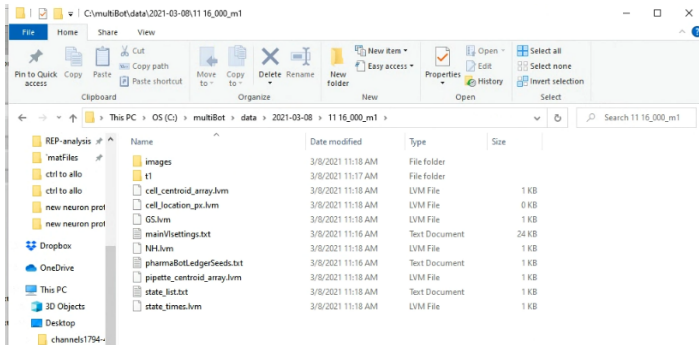
Turn off amplifiers and remove consumables like a conventional patch clamp rig.

Empty the clean and rinse baths.

Data Storage and Analysis

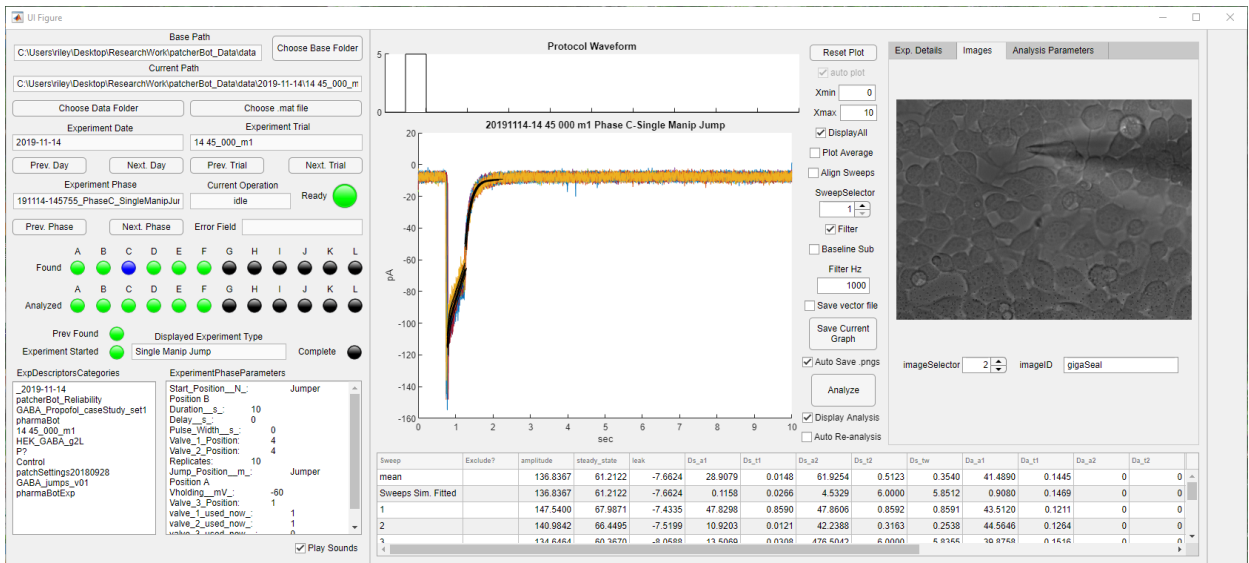
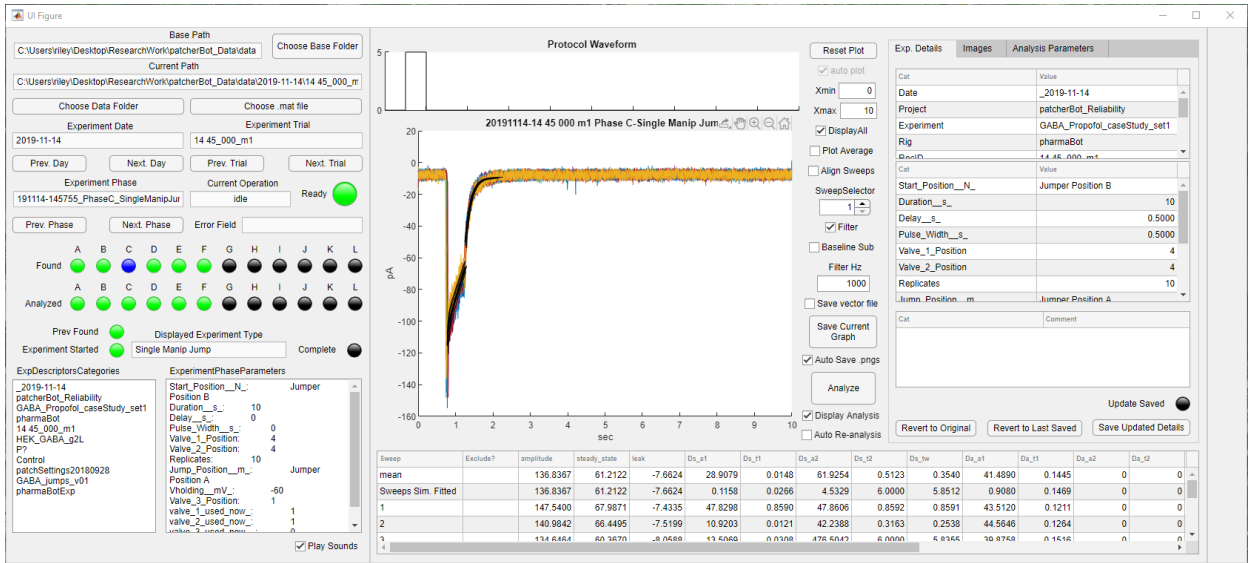
The patcherBot data is stored in a date-time based folder structure. Experiment settings and event status entries are saved. Images from various stages of the patcherBot process are saved. The data is stored in the t1 folder in .lvm files which are ascii-delimited files, the waveform files are also saved. Membrane tests before, between, and after phases are also recorded.

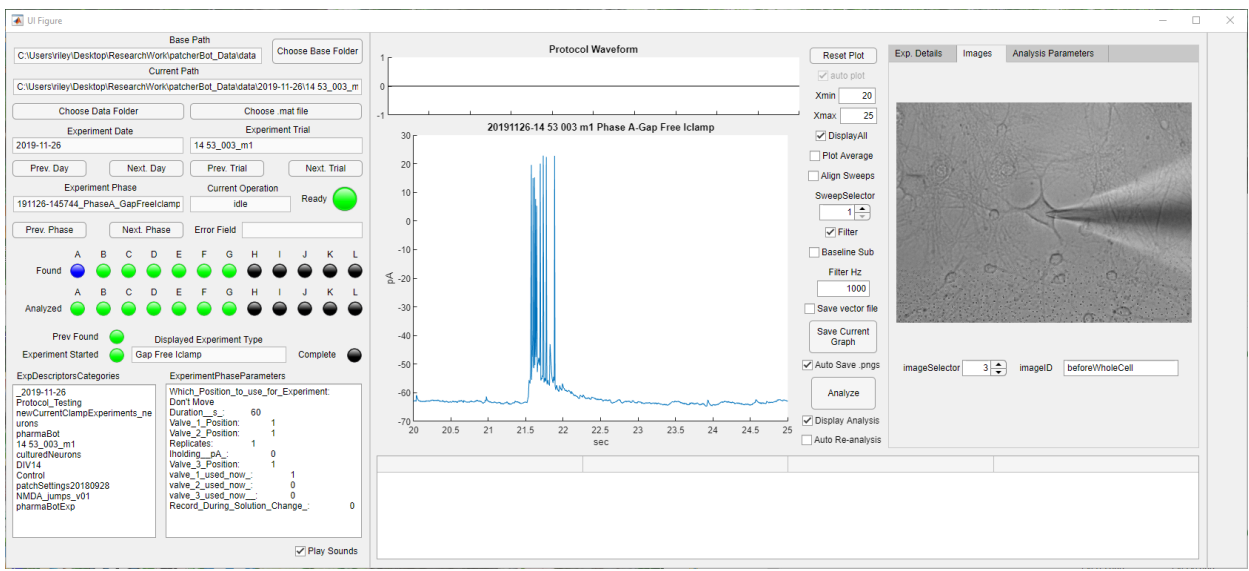
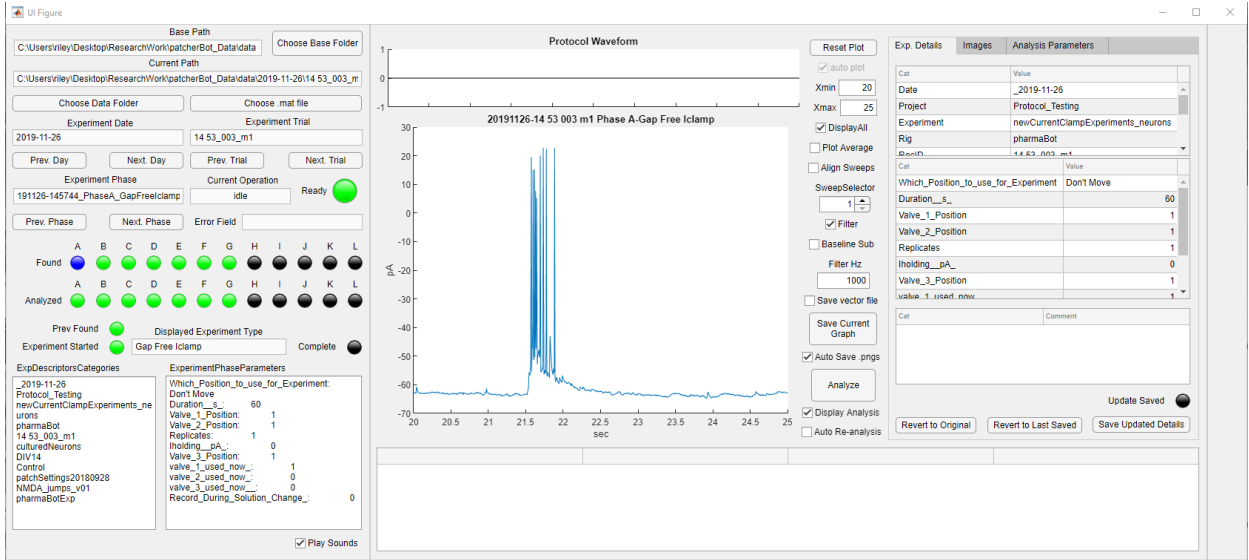




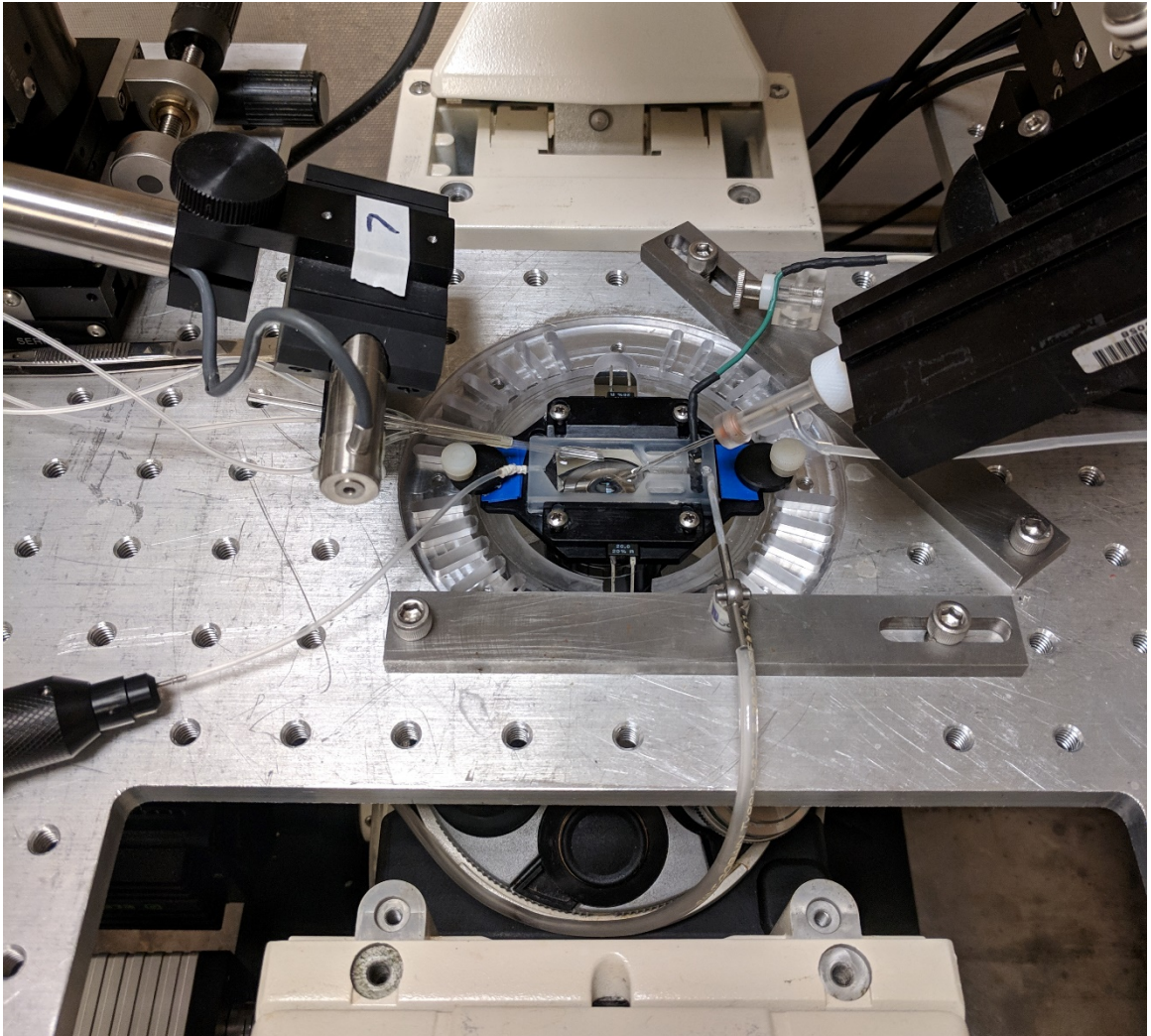
There is also a beta patcherBot data viewer/analyzer (current version is 04_01). It has the ability to analyze piezoelectric translator jumps as well as manipulator jumps.

After selecting a recording folder, it allows one to glance through the results of all experiment phases and step to other trials or experiment days.





Happy Patching:



APPENDIX B
PRELIMINARY "SUPER" PIPETTES

B.1 Quartz and Focused Ion Beam-milled pipettes

Previous literature has shown that focused ion beam-milling (FIB) of borosilicate pipettes showed considerable improvement in improving the resistance of gigaseals which is critical for single ion-channel recordings [122, 123, 124]. Single-channel recordings require extremely high-quality, high-resistance seals and would benefit from a completely flat and smoothed-out pipette tip [1]. Here, we began preliminary studies into the viability of using not only quartz pipettes but FIB-quartz pipettes. All images were taken with a scanning electron microscope (SEM). We see in Figure B.1 and Figure B.2 the difference in smoothness between a regular quartz and FIB-quartz pipette. As reference, we also see in Figure B.3 the outer diameter change pre- and post-FIB mill. We also see that the resistance of a pipette can be changed as a function of the pipette outer diameter (Figure B.4). This can be adjusted by the FIB-milling area. Lastly, we see that the gigaseal change is significant between a regular and FIB pipette highlighted in Table B.1.

Table B.1: Borosilicate vs FIB-milled Quartz Pipettes

Pipette Construction	Resistance (Mohm)	Gigaseal in grease (Mohm)
Borosilicate	2.7	11.8
Borosilicate	2.9	10.9
FIB/Quartz	5.9	100
FIB/Quartz	10.1	100
FIB/Quartz	6.9	100

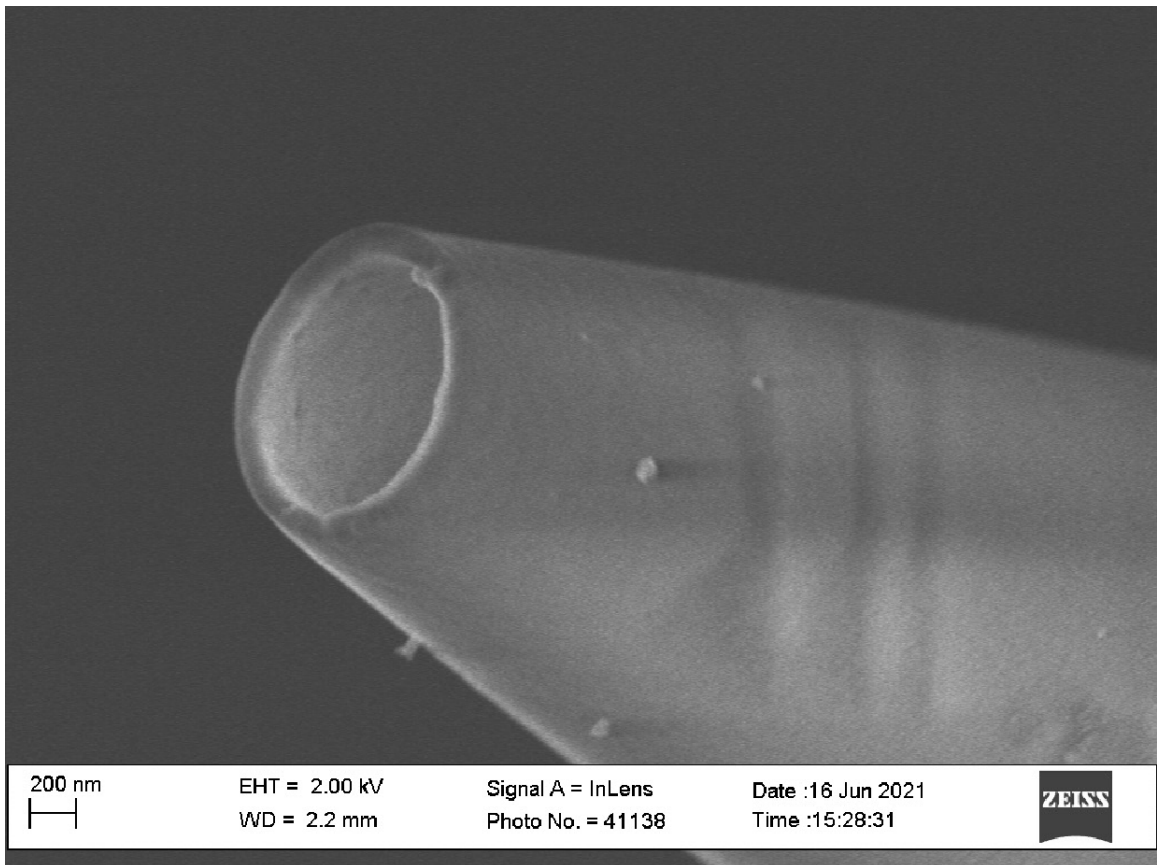


Figure B.1: SEM image of a quartz pipette. The tip of the pipette is rough and not smooth.

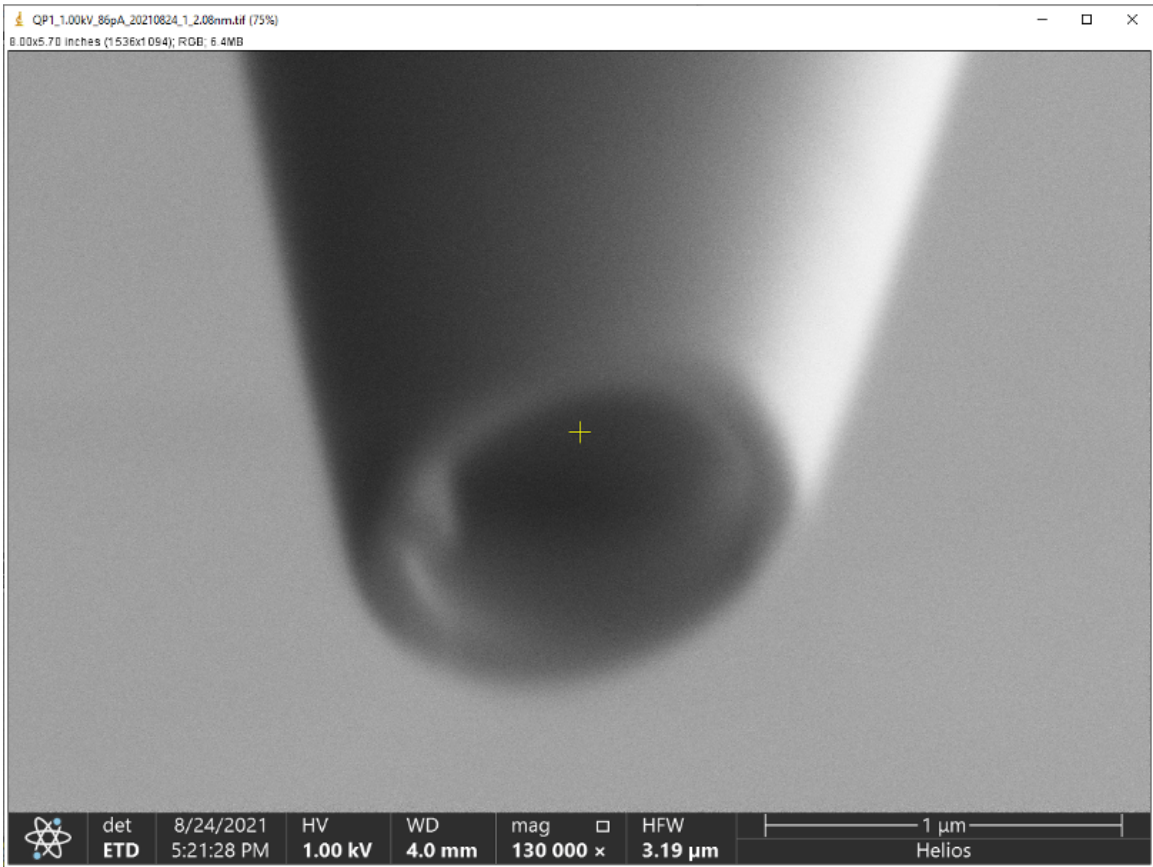


Figure B.2: SEM image of a FIB-quartz pipette. The tip of the pipette has been milled to a smooth surface.

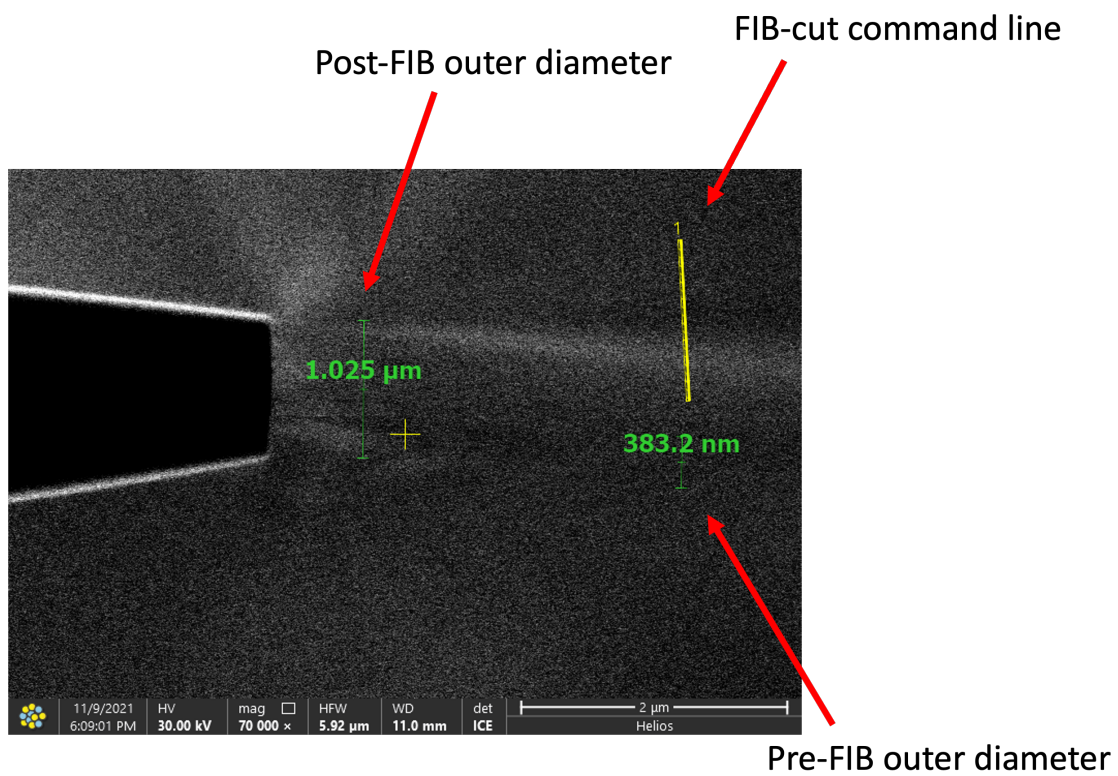


Figure B.3: SEM image of a FIB-quartz pipette showing the initially drawn diameter size of the pipette and the size after FIB-mill. The tip of the pipette has been milled to a smooth surface.

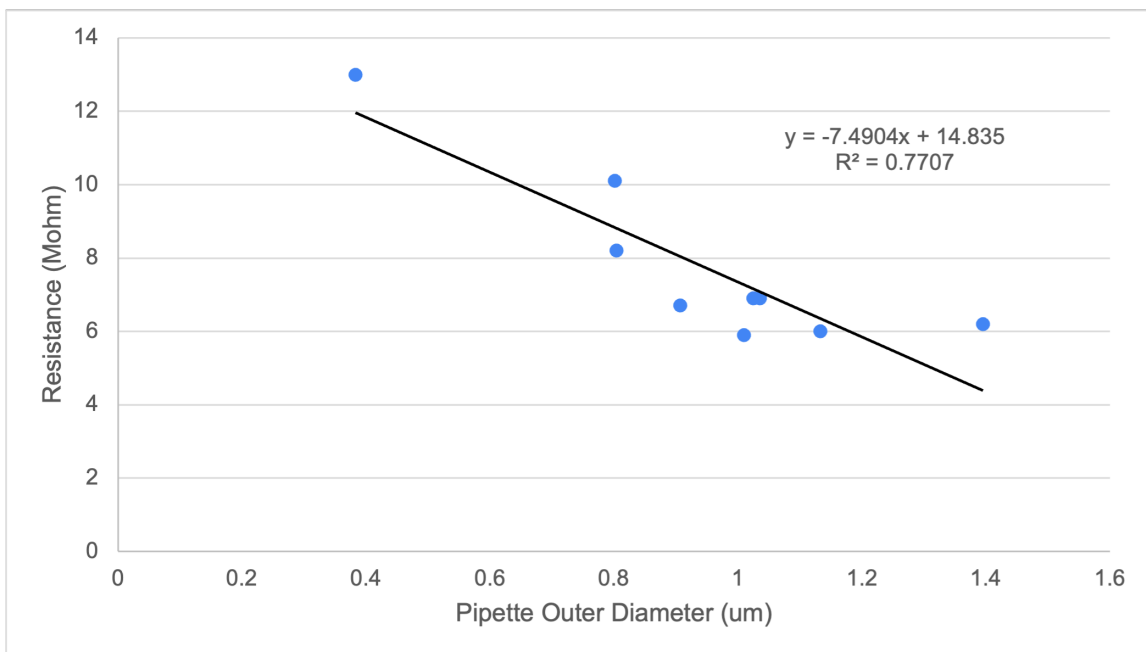


Figure B.4: Resistance of a quartz pipette as a function of outer diameter due to focused ion beam-milling. We can generate pipette resistances based on the milled size of the pipette's outer diameter.

REFERENCES

- [1] E. Neher and B. Sakmann, "Single-channel currents recorded from membrane of denervated frog muscle fibres," *Nature*, vol. 260, no. 5554, pp. 799–802, 1976.
- [2] O. P. Hamill, A. Marty, E. Neher, B. Sakmann, and F. J. Sigworth, "Improved Patch-Clamp Techniques for High-Resolution Current Recording from Cells and Cell-Free Membrane Patches," *Pflügers Archiv*, vol. 391, pp. 85–100, 1981.
- [3] T. Hoshi, W. N. Zagotta, and R. W. Aldrich, "Biophysical and Molecular Mechanisms of Shaker Potassium Channel Inactivation," *Science*, vol. 250, no. 4980, pp. 533–538, Oct. 1990.
- [4] D. H. Edwards, "Mechanisms of depolarizing inhibition at the crayfish giant motor synapse. I. Electrophysiology," <https://doi.org/10.1152/jn.1990.64.2.532>, vol. 64, no. 2, pp. 532–540, 1990.
- [5] D. B. Jaffe, D. Johnston, N. Lasser-Ross, J. E. Lisman, H. Miyakawa, and W. N. Ross, "The spread of Na⁺ spikes determines the pattern of dendritic Ca²⁺ entry into hippocampal neurons," *Nature* 1992 357:6375, vol. 357, no. 6375, pp. 244–246, May 1992.
- [6] M. E. Larkum and J. J. Zhu, "Signaling of layer 1 and whisker-evoked Ca²⁺ and Na⁺ action potentials in distal and terminal dendrites of rat neocortical pyramidal neurons in vitro and in vivo," *The Journal of neuroscience : the official journal of the Society for Neuroscience*, vol. 22, no. 16, pp. 6991–7005, Aug. 2002.
- [7] H. Markram, J. Lübke, M. Frotscher, and B. Sakmann, "Regulation of synaptic efficacy by coincidence of postsynaptic APs and EPSPs," *Science (New York, N.Y.)*, vol. 275, no. 5297, pp. 213–215, Jan. 1997.
- [8] G. J. Stuart, H. U. Dodt, and B. Sakmann, "Patch-clamp recordings from the soma and dendrites of neurons in brain slices using infrared video microscopy," *Pflügers Archiv* 1993 423:5, vol. 423, no. 5, pp. 511–518, Jun. 1993.
- [9] D. R. Castañeda-Castellanos, A. C. Flint, and A. R. Kriegstein, "Blind patch clamp recordings in embryonic and adult mammalian brain slices," *Nature protocols*, vol. 1, no. 2, pp. 532–542, Jul. 2006.
- [10] T. W. Margrie, M. Brecht, and B. Sakmann, "In vivo, low-resistance, whole-cell recordings from neurons in the anaesthetized and awake mammalian brain," *Pflügers Archiv : European journal of physiology*, vol. 444, no. 4, pp. 491–498, 2002.

- [11] G. Tamás, E. H. Buhl, and P. Somogyi, “Fast IPSPs elicited via multiple synaptic release sites by different types of GABAergic neurone in the cat visual cortex,” *The Journal of physiology*, vol. 500 (Pt 3, no. Pt 3, pp. 715–738, May 1997.
- [12] G. Maccaferri, J. David, B. Roberts, P. Szucs, C. A. Cottingham, and P. Somogyi, “Cell surface domain specific postsynaptic currents evoked by identified GABAergic neurones in rat hippocampus in vitro,” *The Journal of physiology*, vol. 524 Pt 1, no. Pt 1, pp. 91–116, Apr. 2000.
- [13] A. Frick, D. Feldmeyer, M. Helmstaedter, and B. Sakmann, “Monosynaptic connections between pairs of L5A pyramidal neurons in columns of juvenile rat somatosensory cortex,” *Cerebral cortex (New York, N.Y. : 1991)*, vol. 18, no. 2, pp. 397–406, Feb. 2008.
- [14] G. A. W. Y, and M. H, “Organizing principles for a diversity of GABAergic interneurons and synapses in the neocortex,” *Science (New York, N.Y.)*, vol. 287, no. 5451, pp. 273–278, 2000.
- [15] N. J. Minshew and D. L. Williams, “The new neurobiology of autism: cortex, connectivity, and neuronal organization,” *Archives of neurology*, vol. 64, no. 7, pp. 945–950, Jul. 2007.
- [16] A. M. Thomson and D. C. West, “Fluctuations in pyramid-pyramid excitatory postsynaptic potentials modified by presynaptic firing pattern and postsynaptic membrane potential using paired intracellular recordings in rat neocortex,” *Neuroscience*, vol. 54, no. 2, pp. 329–346, 1993.
- [17] G. Wang *et al.*, “An optogenetics- and imaging-assisted simultaneous multiple patch-clamp recording system for decoding complex neural circuits,” *Nature Protocols*, vol. 10, no. 3, pp. 397–412, 2015.
- [18] X. Jiang, G. Wang, A. J. Lee, R. L. Stornetta, and J. J. Zhu, “The organization of two new cortical interneuronal circuits,” *Nature Neuroscience*, vol. 16, no. 2, pp. 210–218, 2013.
- [19] S. Lefort, C. Tomm, J. C. Floyd Sarria, and C. C. Petersen, “The excitatory neuronal network of the C2 barrel column in mouse primary somatosensory cortex,” *Neuron*, vol. 61, no. 2, pp. 301–316, Jan. 2009.
- [20] R. Perin, T. K. Berger, and H. Markram, “A synaptic organizing principle for cortical neuronal groups,” *Proceedings of the National Academy of Sciences of the United States of America*, vol. 108, no. 13, pp. 5419–5424, 2011.

- [21] A. K. Lee, J. Epsztein, and M. Brecht, “Whole-cell patch-clamp recordings in freely moving animals,” *Methods in molecular biology (Clifton, N.J.)*, vol. 1183, pp. 263–276, 2014.
- [22] P. G. Aitken, T. Sauer, and S. J. Schiff, “Looking for chaos in brain slices,” *Journal of Neuroscience Methods*, vol. 59, no. 1, pp. 41–48, 1995.
- [23] N. Fertig, R. H. Blick, and J. C. Behrends, “Whole Cell Patch Clamp Recording Performed on a Planar Glass Chip,” *Biophysical Journal*, vol. 82, no. June, pp. 1–7, 2002.
- [24] C. Wood, C. Williams, and G. J. Waldron, “Patch clamping by numbers,” *Drug discovery today*, vol. 9, no. 10, pp. 434–441, May 2004.
- [25] J. Dunlop, M. Bowlby, R. Peri, D. Vasilyev, and R. Arias, “High-throughput electrophysiology: an emerging paradigm for ion-channel screening and physiology,” *Nature Reviews Drug Discovery 2008 7:4*, vol. 7, no. 4, pp. 358–368, 2008.
- [26] S. B. Kodandaramaiah, G. T. Franzesi, B. Y. Chow, E. S. Boyden, and C. R. Forest, “Automated whole-cell patch-clamp electrophysiology of neurons in vivo,” *Nature Methods*, vol. 9, no. 6, pp. 585–587, 2012.
- [27] A. D. Edelstein, M. A. Tsuchida, N. Amodaj, H. Pinkard, R. D. Vale, and N. Stuurman, “Advanced methods of microscope control using μ Manager software,” *Journal of Biological Methods*, vol. 1, no. 2, e10, Nov. 2014.
- [28] B. A. Suter *et al.*, “Ephus: Multipurpose Data Acquisition Software for Neuroscience Experiments,” *Frontiers in Neural Circuits*, vol. 4, no. AUG, Aug. 2010.
- [29] L. Campagnola, M. B. Kratz, and P. B. Manis, “ACQ4: an open-source software platform for data acquisition and analysis in neurophysiology research,” *Frontiers in neuroinformatics*, vol. 8, no. JAN, Jan. 2014.
- [30] R. Perin and H. Markram, “A Computer-assisted Multi-electrode Patch-clamp System,” *JoVE (Journal of Visualized Experiments)*, vol. 80, no. 80, e50630, Oct. 2013.
- [31] I. Kolb *et al.*, “PatcherBot: a single-cell electrophysiology robot for adherent cells and brain slices,” *Journal of Neural Engineering*, vol. 16, no. 4, p. 046 003, May 2019.
- [32] C. R. Landry, M. C. Yip, I. Kolb, W. A. Stoy, M. M. Gonzalez, and C. R. Forest, “Method for Rapid Enzymatic Cleaning for Reuse of Patch Clamp Pipettes: Increasing Throughput by Eliminating Manual Pipette Replacement between Patch Clamp Attempts,” *Bio-protocol*, vol. 11, no. 14, Jul. 2021.

- [33] H.-b. Yu, M. Li, W.-p. Wang, and X.-l. Wang, “High throughput screening technologies for ion channels,” *Acta Pharmacologica Sinica*, vol. 37, no. 1, pp. 34–43, 2016.
- [34] A. Obergrussberger *et al.*, “An update on the advancing high-throughput screening techniques for patch clamp-based ion channel screens: implications for drug discovery,” *Expert opinion on drug discovery*, vol. 13, no. 3, pp. 269–277, Jan. 2018.
- [35] C. Liu, T. Li, and J. Chen, “Role of High-Throughput Electrophysiology in Drug Discovery,” *Current Protocols in Pharmacology*, vol. 87, no. 1, e69, Dec. 2019.
- [36] I. Mollinedo-Gajate, C. Song, and T. Knöpfel, “Genetically encoded fluorescent calcium and voltage indicators,” *Handb Exp Pharmacol*, vol. 260, pp. 209–229, 2019.
- [37] L. A. Anecchino, A. R. Morris, C. S. Copeland, O. E. Agabi, P. Chadderton, and S. R. Schultz, “Robotic Automation of In Vivo Two-Photon Targeted Whole-Cell Patch-Clamp Electrophysiology,” *Neuron*, vol. 95, no. 5, pp. 1048–1055, 2017.
- [38] Q. Wu *et al.*, “Integration of autpatching with automated pipette and cell detection in vitro,” *Journal of Neurophysiology*, vol. 116, no. 4, pp. 1564–1578, Oct. 2016.
- [39] H. Wang *et al.*, “High-speed mapping of synaptic connectivity using photostimulation in Channelrhodopsin-2 transgenic mice,” *Proceedings of the National Academy of Sciences of the United States of America*, vol. 104, no. 19, pp. 8143–8148, 2007.
- [40] H. H. Yang and F. St-Pierre, “Genetically encoded voltage indicators: Opportunities and challenges,” *Journal of Neuroscience*, vol. 36, no. 39, pp. 9977–9989, 2016.
- [41] E. Ronzitti *et al.*, “Submillisecond optogenetic control of neuronal firing with two-photon holographic photoactivation of chronos,” *Journal of Neuroscience*, vol. 37, no. 44, pp. 10 679–10 689, 2017.
- [42] K. D. Piatkevich *et al.*, “A robotic multidimensional directed evolution approach applied to fluorescent voltage reporters,” *Nature Chemical Biology*, vol. 14, no. 4, pp. 352–360, 2018.
- [43] Y. Ku Cho *et al.*, “Multidimensional screening yields channelrhodopsin variants having improved photocurrent and order-of-magnitude reductions in calcium and proton currents,” *Journal of Biological Chemistry*, vol. 294, no. 11, pp. 3806–3821, 2019.
- [44] D. R. Hochbaum *et al.*, “All-optical electrophysiology in mammalian neurons using engineered microbial rhodopsins,” *Nature Methods*, vol. 11, no. 8, pp. 825–833, 2014.

- [45] K. Koos, “Automatic deep learning driven label-free image guided patch clamp system for human and rodent in vitro slice physiology,” *bioRxiv*, 2020.
- [46] L. Campagnola *et al.*, “Local connectivity and synaptic dynamics in mouse and human neocortex,” *Science*, vol. 375, no. 6585, eabj5861, Mar. 2023.
- [47] X. Jiang *et al.*, “Principles of connectivity among morphologically defined cell types in adult neocortex,” *Science*, vol. 350, no. 6264, pp. 1–51, 2015.
- [48] J. DeFelipe, “Types of neurons synaptic connections and chemical characteristics of cells,” *Journal of chemical neuroanatomy*, vol. 14, pp. 1–19, 1997.
- [49] L. Campagnola and P. B. Manis, “A map of functional synaptic connectivity in the mouse anteroventral cochlear nucleus,” *Journal of Neuroscience*, vol. 34, no. 6, pp. 2214–2230, 2014.
- [50] J. B. Ruden, L. L. Dugan, and C. Konradi, “Parvalbumin interneuron vulnerability and brain disorders,” *Neuropsychopharmacology*, vol. 46, no. 2, pp. 279–287, 2021.
- [51] H. F. Iaccarino *et al.*, “Gamma frequency entrainment attenuates amyloid load and modifies microglia,” *Nature 2016 540:7632*, vol. 540, no. 7632, pp. 230–235, Dec. 2016.
- [52] L. Verret *et al.*, “Inhibitory interneuron deficit links altered network activity and cognitive dysfunction in Alzheimer model,” *Cell*, vol. 149, no. 3, pp. 708–721, Apr. 2012.
- [53] H.-J. Suk, E. S. Boyden, and I. van Welie, “Advances in the automation of whole-cell patch clamp technology,” *Journal of Neuroscience Methods*, vol. 326, p. 108 357, 2019.
- [54] D. Colquhoun and F. J. Sigworth, “Fitting and Statistical Analysis of Single-Channel Records,” in *Single-Channel Recording*, B. Sakmann and E. Neher, Eds., Boston, MA: Springer US, 1995, pp. 483–587, ISBN: 978-1-4419-1229-9.
- [55] A. Auerbach and Y. Zhou, “Gating reaction mechanisms for NMDA receptor channels,” *J Neurosci*, vol. 25, no. 35, pp. 7914–7923, 2005.
- [56] S. Chakrapani *et al.*, “On The Structural Basis of Modal Gating Behavior in K(+) Channels,” *Nature structural & molecular biology*, vol. 18, no. 1, pp. 67–74, 2011.
- [57] H.-w. Ai, “Fluorescent-protein-based probes: general principles and practices,” *Analytical and Bioanalytical Chemistry*, vol. 407, no. 1, pp. 9–15, 2015.

- [58] C. Deo and L. D. Lavis, “Synthetic and genetically encoded fluorescent neural activity indicators,” *Current Opinion in Neurobiology*, vol. 50, pp. 101–108, 2018.
- [59] L. A. Anecchino and S. R. Schultz, “Progress in automating patch clamp cellular physiology,” *Brain and Neuroscience Advances*, vol. 2, p. 239 821 281 877 656, 2018.
- [60] I. Kolb, W. A. Stoy, E. B. Rousseau, O. A. Moody, A. Jenkins, and C. R. Forest, “Cleaning patch-clamp pipettes for immediate reuse,” *Scientific Reports*, vol. 6, Oct. 2016.
- [61] N. G. Glasgow and J. W. Johnson, “Whole-Cell Patch-Clamp Analysis of Recombinant NMDA Receptor Pharmacology Using Brief Glutamate Applications,” in *Patch-Clamp Methods and Protocols*, M. Martina and S. Taverna, Eds., New York, NY: Springer New York, 2014, pp. 23–41, ISBN: 978-1-4939-1096-0.
- [62] D. M. MacLean, “Constructing a Rapid Solution Exchange System,” in *Ionotropic Glutamate Receptor Technologies*, G. K. Popescu, Ed., New York, NY: Springer New York, 2016, pp. 165–183, ISBN: 978-1-4939-2812-5.
- [63] B. A. Orser, L. Y. Wang, P. S. Pennefather, and J. F. MacDonald, “Propofol modulates activation and desensitization of GABAA receptors in cultured murine hippocampal neurons,” vol. 14, no. 12, pp. 7747–7760, 1994.
- [64] S. Adodra and T. G. Hales, “Potentiation, activation and blockade of GABAA receptors of clonal murine hypothalamic GT1-7 neurones by propofol,” *British Journal of Pharmacology*, vol. 115, no. 6, pp. 953–960, 1995.
- [65] M. C. Yip, M. M. Gonzalez, C. R. Valenta, M. J. Rowan, and C. R. Forest, “Deep learning-based real-time detection of neurons in brain slices for in vitro physiology,” *Scientific Reports 2021 11:1*, vol. 11, no. 1, pp. 1–9, Mar. 2021.
- [66] K. S. Button *et al.*, “Power failure: why small sample size undermines the reliability of neuroscience,” *Nature Reviews Neuroscience*, vol. 14, no. 5, pp. 365–376, 2013.
- [67] M. R. Munafò *et al.*, “A manifesto for reproducible science,” *Nature Human Behaviour*, vol. 1, no. 1, p. 21, 2017.
- [68] T. J. Wardill *et al.*, “A Neuron-Based Screening Platform for Optimizing Genetically-Encoded Calcium Indicators,” *PLOS ONE*, vol. 8, no. 10, e77728–, Oct. 2013.
- [69] J. Akerboom *et al.*, “Optimization of a GCaMP Calcium Indicator for Neural Activity Imaging,” *The Journal of Neuroscience*, vol. 32, no. 40, p. 13 819, Oct. 2012.

- [70] Y. Xu, P. Zou, and A. E. Cohen, “Voltage imaging with genetically encoded indicators,” *Current Opinion in Chemical Biology*, vol. 39, pp. 1–10, 2017.
- [71] M. Z. Lin and M. J. Schnitzer, “Genetically encoded indicators of neuronal activity,” *Nature Neuroscience*, vol. 19, no. 9, pp. 1142–1153, 2016.
- [72] J. M. Kralj, A. D. Douglass, D. R. Hochbaum, D. Maclaurin, and A. E. Cohen, “Optical recording of action potentials in mammalian neurons using a microbial rhodopsin,” *Nature Methods*, vol. 9, no. 1, pp. 90–95, 2012.
- [73] M.-P. Chien *et al.*, “Photoactivated voltage imaging in tissue with an archaerhodopsin-derived reporter,” *Science Advances*, vol. 7, no. 19, eabe3216, Mar. 2023.
- [74] N. C. Flytzanis *et al.*, “Archaerhodopsin variants with enhanced voltage-sensitive fluorescence in mammalian and *Caenorhabditis elegans* neurons,” *Nature Communications*, vol. 5, no. 1, p. 4894, 2014.
- [75] R. S. McIsaac *et al.*, “Directed evolution of a far-red fluorescent rhodopsin,” *Proceedings of the National Academy of Sciences*, vol. 111, no. 36, pp. 13 034–13 039, Sep. 2014.
- [76] Y. Gong *et al.*, “High-speed recording of neural spikes in awake mice and flies with a fluorescent voltage sensor,” *Science*, vol. 350, no. 6266, pp. 1361–1366, Dec. 2015.
- [77] J. B. Grimm *et al.*, “A general method to improve fluorophores for live-cell and single-molecule microscopy,” *Nature Methods*, vol. 12, no. 3, pp. 244–250, 2015.
- [78] J. B. Grimm *et al.*, “A general method to fine-tune fluorophores for live-cell and in vivo imaging,” *Nature Methods*, vol. 14, no. 10, pp. 987–994, 2017.
- [79] A. S. Abdelfattah *et al.*, “Bright and photostable chemigenetic indicators for extended in vivo voltage imaging,” *Science*, vol. 365, no. 6454, pp. 699–704, Aug. 2019.
- [80] Y. Bando, M. Sakamoto, S. Kim, I. Ayzenshtat, and R. Yuste, “Comparative Evaluation of Genetically Encoded Voltage Indicators,” *Cell Reports*, vol. 26, no. 3, pp. 802–813, Jan. 2019.
- [81] F. St-Pierre, J. D. Marshall, Y. Yang, Y. Gong, M. J. Schnitzer, and M. Z. Lin, “High-fidelity optical reporting of neuronal electrical activity with an ultrafast fluorescent voltage sensor,” *Nature Neuroscience*, vol. 17, no. 6, pp. 884–889, 2014.
- [82] J. Park *et al.*, “Screening Fluorescent Voltage Indicators with Spontaneously Spiking HEK Cells,” vol. 8, no. 12, pp. 1–10, 2013.

- [83] A. Noguchi, Y. Ikegaya, and N. Matsumoto, “In Vivo Whole-Cell Patch-Clamp Methods: Recent Technical Progress and Future Perspectives,” *Sensors*, vol. 21, no. 4, 2021.
- [84] J. Lee, I. Kolb, C. R. Forest, and C. J. Rozell, “Cell membrane tracking in living brain tissue using differential interference contrast microscopy,” *IEEE Trans. Image Process.*, vol. 27, no. 4, pp. 1847–1861, Apr. 2018.
- [85] T. Vicar *et al.*, “Cell segmentation methods for label-free contrast microscopy: Review and comprehensive comparison,” *BMC Bioinform.*, vol. 20, no. 1, pp. 1564–1578, Jun. 2019.
- [86] Z. Zhou, S. Sorensen, H. Zeng, M. Hawrylycz, and H. Peng, “Adaptive image enhancement for tracing 3d morphologies of neurons and brain vasculatures,” *Neuroinformatics*, vol. 13, no. 2, pp. 153–166, Oct. 2015.
- [87] A. Dufour, V. Shinin, S. Tajbakhsh, N. Guillén-Aghion, J. C. Olivo-Marin, and C. Zimmer, “Segmenting and tracking fluorescent cells in dynamic 3-d microscopy with coupled active surfaces,” *IEEE Trans. Image Process.*, vol. 14, no. 9, pp. 1396–1410, Sep. 2005.
- [88] R. W. Oei *et al.*, “Convolutional neural network for cell classification using microscope images of intracellular actin networks,” *PLoS ONE*, vol. 14, no. 3, Mar. 2019.
- [89] Q. Wang, S. Bi, M. Sun, Y. Wang, D. Wang, and S. Yang, “Deep learning approach to peripheral leukocyte recognition,” *PLoS ONE*, vol. 14, no. 6, Aug. 2019.
- [90] Y. Al-Kofahi, A. Zaltsman, R. Graves, W. Marshall, and M. Rusu, “A deep learning-based algorithm for 2-d cell segmentation in microscopy image,” *BMC Bioinform.*, vol. 19, no. 1, Oct. 2018.
- [91] S. Berg *et al.*, “ilastik: Interactive machine learning for (bio)image analysis,” *Nat. Methods*, vol. 16, no. 12, pp. 1226–1232, Dec. 2019.
- [92] I. Suleymanova *et al.*, “A deep convolutional neural network approach for astrocyte detection,” *Scientific Reports*, vol. 8, no. 1, pp. 1–7, 2018.
- [93] W. A. Stoy *et al.*, “Robotic navigation to sub-cortical neural tissue for intracellular electrophysiology in vivo,” *J. Neurophysiol.*, vol. 118, no. 2, pp. 1141–1150, Aug. 2017.
- [94] J. Redmon and A. Farhadi, “YOLOv3: An Incremental Improvement,” *arXiv e-prints*, arXiv:1804.02767, arXiv:1804.02767, Apr. 2018. arXiv: 1804.02767 [cs.CV].

- [95] J. Redmon, S. K. Divvala, R. B. Girshick, and A. Farhadi, “You only look once: Unified, real-time object detection,” *CoRR*, vol. abs/1506.02640, 2015. arXiv: 1506.02640.
- [96] I. Kolb *et al.*, “Patcherbot: A single-cell electrophysiology robot for adherent cells and brain slices,” *Journal of Neural Engineering*, vol. 16, no. 4, pp. 1847–1861, 2019.
- [97] T. Lin, *Labelimg*, 2015.
- [98] J. Deng, W. Dong, R. Socher, L. Li, K. Li, and L. Fei-Fei, *Imagenet: A large-scale hierarchical image database*, 2009.
- [99] E. S. Olivas, J. D. M. Guerrero, M. M. Sober, J. R. M. Benedito, and A. J. S. Lopez, *Handbook of Research on Machine Learning Applications and Trends: Algorithms, Methods, and Techniques*. Information Science Reference - Imprint of: IGI Publishing, 2010, ISBN: 978-1-60566-766-9.
- [100] M. Everingham, L. Van Gool, C. K. Williams, J. Winn, and A. Zisserman, “The pascal visual object classes (voc) challenge,” *Int. J. Comput. Vis.*, vol. 88, no. 2, pp. 303–338, Jun. 2010.
- [101] J. Cartucho, R. Ventura, and M. Veloso, “Robust object recognition through symbiotic deep learning in mobile robots,” *2018 IEEE/RSJ International Conference on Intelligent Robots and Systems (IROS)*, pp. 2336–2341, 2018.
- [102] R. C. Gonzalez and R. E. Woods, *Digital image processing (3rd edition)*, USA, 2006.
- [103] O. P. Hamill, A. Marty, E. Neher, B. Sakmann, and F. J. Sigworth, “Improved patch-clamp techniques for high-resolution current recording from cells and cell-free membrane patches,” *Pflugers Archiv European Journal of Physiology*, vol. 391, no. 2, pp. 85–100, 1981.
- [104] Y. Peng, F. X. Mittermaier, H. Planert, U. C. Schneider, H. Alle, and J. R. Geiger, “High-throughput microcircuit analysis of individual human brains through next-generation multineuron patch-clamp,” *eLife*, vol. 8, Nov. 2019.
- [105] I. Jafar and H. Ying, “New algorithms for contrast enhancement in grayscale images based on the variational definition of histogram equalization,” *Integr. Comput.-Aided Eng.*, vol. 15, no. 2, pp. 131–147, 2008.
- [106] N. Kashiwagi, “On use of the kalman filter for spatial smoothing,” *Annals of the Institute of Statistical Mathematics volume*, vol. 45, pp. 21–34, 1993.

- [107] P. Molchanov, S. Tyree, T. Karras, T. Aila, and J. Kautz, “Pruning convolutional neural networks for resource efficient transfer learning,” *CoRR*, vol. abs/1611.06440, 2016. arXiv: 1611.06440.
- [108] R. Miles and J. C. Poncer, “Paired recording from neurones,” *Curr. Opin. Neurobiol.*, vol. 6, no. 3, pp. 387–394, 1996.
- [109] S. Song, P. J. Sjöström, M. Reigl, S. Nelson, and D. B. Chklovskii, “Highly non-random features of synaptic connectivity in local cortical circuits,” *PLoS Biology*, vol. 3, no. 3, pp. 0507–0519, 2005.
- [110] S. B. Kodandaramaiah *et al.*, “Multi-neuron intracellular recording in vivo via interacting autpatching robots,” *eLife*, vol. 7, A. J. King, Ed., e24656, 2018.
- [111] M. Świechowski, K. Godlewski, B. Sawicki, and J. Mańdziuk, “Monte Carlo Tree Search: a review of recent modifications and applications,” *Artificial Intelligence Review*, vol. 56, no. 3, pp. 2497–2562, 2023.
- [112] R. E. Perszyk *et al.*, “Automated Intracellular Pharmacological Electrophysiology for Ligand-Gated Ionotropic Receptor and Pharmacology Screening,” *Molecular Pharmacology*, vol. 100, no. 1, 73 LP –82, Jul. 2021.
- [113] G. I. Vera Gonzalez, P. O. Kgwarae, and S. R. Schultz, “Two-Photon Targeted, Quad Whole-Cell Patch-Clamping Robot,” *bioRxiv*, p. 2022.11.14.516499, Jan. 2023.
- [114] L. Campagnola *et al.*, “Local connectivity and synaptic dynamics in mouse and human neocortex,” *Science*, vol. 375, no. 6585, 2022.
- [115] L. Petreanu, D. Huber, A. Sobczyk, and K. Svoboda, “Channelrhodopsin-2-assisted circuit mapping of long-range callosal projections,” *Nature Neuroscience*, vol. 10, no. 5, pp. 663–668, 2007.
- [116] M. Bartos, I. Vida, M. Frotscher, J. R. P. Geiger, and P. Jonas, “Rapid Signaling at Inhibitory Synapses in a Dentate Gyrus Interneuron Network,” *The Journal of Neuroscience*, vol. 21, no. 8, 2687 LP –2698, Apr. 2001.
- [117] S. Grosser, F. J. Barreda, P. Beed, D. Schmitz, S. A. Booker, and I. Vida, “Parvalbumin Interneurons Are Differentially Connected to Principal Cells in Inhibitory Feedback Microcircuits along the Dorsoventral Axis of the Medial Entorhinal Cortex,” *eneuro*, vol. 8, no. 1, pp. 0354–20, Jan. 2021.
- [118] L. E. Linders *et al.*, *Studying Synaptic Connectivity and Strength with Optogenetics and Patch-Clamp Electrophysiology*, 2022.

- [119] G. Qi, G. Radnikow, and D. Feldmeyer, “Electrophysiological and morphological characterization of neuronal microcircuits in acute brain slices using paired patch-clamp recordings.,” *Journal of visualized experiments : JoVE*, no. 95, p. 52358, Jan. 2015.
- [120] H. Zeng and J. R. Sanes, “Neuronal cell-type classification: Challenges, opportunities and the path forward,” *Nature Reviews Neuroscience*, vol. 18, no. 9, pp. 530–546, 2017.
- [121] B. R. Lee *et al.*, “Scaled, high fidelity electrophysiological, morphological, and transcriptomic cell characterization,” *eLife*, vol. 10, 2021.
- [122] M. Malboubi, H. Ostadi, S. Wang, Y. Gu, and K. Jiang, “The Effect of Pipette Tip Roughness on Giga-seal Formation,” in *Proceedings of the World Congress on Engineering*, vol. II, 2009, pp. 29–47, ISBN: 9789881821010.
- [123] M. Malboubi, Y. Gu, and K. Jiang, “Surface properties of glass micropipettes and their effect on biological studies,” Tech. Rep., 2011.
- [124] M. Malboubi, Y. Gu, and K. Jiang, “Experimental and simulation study of the effect of pipette roughness on giga-seal formation in patch clamping,” *Microelectronic Engineering*, vol. 87, no. 5-8, pp. 778–781, May 2010.